FABRICATION, CHARACTERIZATION AND APPLICATION OF PHTHALOCYANINE-MAGNETITE HYBRID NANOFIBERS

A thesis submitted in fulfilment of the requirements

for the degree of

MASTER OF SCIENCE

Of

RHODES UNIVERSITY

By

PHILLIMON MOKANNE MODISHA

October 2013

Dedication

To

My Mother

WILHEMINAH MMEMME BOKABA

(*Pheladi*)

Acknowledgements

First and foremost, I would like to thank God for his grace. ***''Except the LORD build the house, the labour in vain that build it: except the LORD keep the city, the watchman waketh but in vain''. Psalm 127***

I want to offer my sincere gratitude to my supervisor, Prof. Tebello Nyokong, who supported me throughout the course of my thesis and giving me a room to work in my own way. I attribute the level of my Masters degree to her encouragement, patience and effort. Her motto "**Just do it**" was my driving force to always work harder. I also appreciate the fact that you unlock the great potential within the students to succeed. Thank you for opening new avenues and frontiers by sending me to Belgium (Ghent University) for a month, this is truly remarkable. Making it possible for me to attend conferences made my academic life enjoyable.

The good advice, support and friendship from my co-supervisor, Dr. Edith Antunes, has been valuable on both academic and personal levels, for which I am extremely grateful.

I was fortunate to pursue my Masters degree within the Nanotechnology Innovation Center/ Sensors cohosted by Rhodes University Department of Chemistry. Special thanks to Dr. Nkosiphile Masilela and Edward Sekhosana, you made me understand that there are still kind people in this world. I appreciate all your help and patience. I personally view lab S22 as a Research and Development (R&D) industry, where team work is important. Thanks to Mpho, Jessica, Sarah, Thandeka, Papa Dayo, Audacity, Stephens, Phindile, Muthumuni and lab S22 research group as a whole for support and working together. Keep that spirit of family friendship. My associate in struggle, Cassious Sekgota, you opened my mind socially. Thanks to my brothers

and sisters in faith Dr. Lucas Mmonwa, David Maahlamela, Nomthandazo Zondani, Prudent Mokgokong, Bongiwe Miga, Kgoroane Makgopo, Hlaulani Hlungwane and ZCCSF Rhodes University as a whole. ***"Ke lwanne ntwa e molemo se sentshaletseng ke moqhaka wa hlooho''***

Financial support by Enerst and Ethel Eriksen Trust, the Department of Science and Technology (DST) and National Research Foundation (NRF), South Africa through DST/NRF Chairs Initiative for Professor of Medicinal Chemistry and Nanotechnology, ProcoTex, Rhodes University as well as DST/Mintek Nanotechnology Innovation Centre is gratefully acknowledged.

My understanding of technical things was nourished by my grandfather (Mokanne) who taught me more about automobiles both diesel and petrol engines, *ke a leboga Mokone*. Special thanks to my late grandmother (Ntsae) who raised me but I am sorry, you were so unfortunate not to see my success. My late younger sister (Tlaishego), thanks for predicting my academic life.

At last my parents more especially my mother (Mmemme) who is actually my advisor an "intellectual thinker" for being proud of me. My siblings, Kgothatso, Matshidiso and Kgaugelo for their best wishes, you really missed me.

Abstract

Magnetic nanoparticles comprising magnetite (Fe_3O_4) were functionalized with 3-aminopropyl-triethoxysilane forming amino functionalized magnetite nanoparticles (AMNPs). The amino group allows for conjugation with zinc octacarboxyphthalocyanine (ZnOCPc) or zinc tetracarboxyphthalocyanine (ZnTCPc) via the carboxyl group to form an amide bond. A reduced aggregation of ZnTCPc is observed after conjugation with AMNPs. The thermal stability, conjugation, morphology and the sizes of the nanoparticles and their conjugates were confirmed using thermogravimetric analysis (TGA), Fourier transform infrared spectroscopy (FTIR), transmission electron microscopy (TEM) and Powder X-ray diffractometry (PXRD), respectively. The covalent linkage of AMNPs to ZnOCPc or ZnTCPc resulted in improvement in the photophysical behavior of the phthalocyanines. Improvement in the triplet quantum yield (Φ_T), singlet oxygen quantum yield (Φ_Δ), triplet lifetime (τ_T) and singlet oxygen lifetime (τ_Δ) of the ZnOCPc or ZnTCPc were observed, hence improving the photosensitizers efficiency. The conjugates comprising of zinc octacarboxyphthalocyanine (ZnOCPc) and AMNPs were electrospun into fibers using polyamide-6 (PA-6). This was used for the photodegradation of Orange-G and compared with ZnOCPc-AMNPs in suspension. For ZnOCPc-AMNPs in suspension, it is noteworthy that the catalyst can be easily recovered using an external magnetic field. The singlet oxygen generation increases as we increase the fiber diameter by increasing the ZnOCPc concentration. The singlet oxygen quantum yield is higher for PA-6/ZnOCPc-AMNPs nanofibers when compared to PA-6/ZnOCPc. The rate of degradation of Orange-G increased with an increase in the singlet oxygen quantum yield. Moreover, the kinetic analysis showed that the photodecomposition of Orange-G is a first-order reaction according to the Langmuir-Hinshelwood model.

Table of Contents

List of Symbols

ΔA	=	**Change in absorbance following laser pulse**
AA	=	**Acetic acid**
I	=	**Intensity of light**
I_{abs}	=	**Intensity of light absorbed**
F	=	**Fluorescence intensity**
FA	=	**Formic acid**
α	=	**Non-peripheral position**
β	=	**Peripheral position**
ε	=	**Molar extinction coefficient**
ε_S	=	**Singlet state extinction coefficient**
ε_T	=	**Triplet state extinction coefficient**
λ_{em}	=	**Wavelength of emission spectrum maximum**
λ_{exc}	=	**Wavelength of excitation spectrum maximum**
hv	=	**Light Energy**
n	=	**Refractive index**
Φ_Δ	=	**Singlet oxygen quantum yield**
Φ_F	=	**Fluorescence quantum yield**
Φ_T	=	**Triplet state quantum yield**
τ_Δ	=	**Singlet oxygen lifetime**
τ_F	=	**Fluorescence lifetime**
τ_T	=	**Triplet state lifetime**
χ^2	=	**Reduced Chi-squared statistic**
$^1O_2$	=	**Singlet molecular oxygen**
$^3O_2$	=	**Triplet molecular oxygen**
O_2	=	**Ground state molecular oxygen**
S_0	=	**Ground singlet state**

S_1	**=**	**Excited singlet state**
T_1	**=**	**First excited triplet state**
T_2	**=**	**Second excited triplet state**
k	**=**	**Apparent rate constant**
K_{obs}	**=**	**Observed rate constant**
K_A	**=**	**Adsorption coefficient**

List of Abbreviations

A	**=**	**Absorbance**
ADMA	**=**	**Anthracene-9, 10-bis-methylmalonate**
AlPcSmix	**=**	**Mixed-sulfonated aluminium phthalocyanine**
APTES	**=**	**3-aminopropyltriethoxysilane**
CT	**=**	**Charge-transfer transitions**
DBU	**=**	**1, 8-diazabicyclo[5.4.0]undec-7-ene**
DMF	**=**	**Dimethylformamide**
DMSO	**=**	**Dimethylsulphoxide**
EDC	**=**	**1-ethyl-3-(3-dimethylaminopropyl) carbodiimide hydrochloride**
EDS	**=**	**Energy dispersive x-ray spectroscopy**
ET	**=**	**Energy transfer**
EtOH	**=**	**Ethanol**
F	**=**	**Fluorescence**
H_2Pc	**=**	**Metal-free phthalocyanine**
HOMO	**=**	**Highest occupied molecular orbital**
IC	**=**	**Internal conversion**
IR	**=**	**Infrared**
ISC	**=**	**Intersystem crossing**
L-H	**=**	**Langmuir-Hinshelwood**
LMCT	**=**	**Ligand-to-metal charge transfer**
LUMO	**=**	**Lowest unoccupied molecular orbital**
MLCT	**=**	**Metal-to-ligand charge transfer**
MOCPc	**=**	**Metallo-octacarboxy phthalocyanine**
MPc	**=**	**Metallophthalocyanine**
MTCPc	**=**	**Metallotetracarboxy phthalocyanine**
NaOH	**=**	**Sodium hydroxide**
NHS	**=**	**N-hydroxysuccinimide**

OG	**=**	**Orange-G**
PA-6	**=**	**Polyamide-6**
Pc	**=**	**Phthalocyanine**
PDT	**=**	**Photodynamic therapy**
RH	**=**	**Relative humidity**
ROS	**=**	**Reactive Oxygen Species**
SEM	**=**	**Scanning Electron Microscopy**
SOC	**=**	**Spin-orbit coupling**
TCSPC	**=**	**Time-correlated single photon counting**
TEM	**=**	**Transmission electron microscope**
TGA	**=**	**Thermogravimetric analysis**
TEOS	**=**	**Tetraethoxysilane**
UV/Vis	**=**	**Ultraviolet/visible**
PXRD	**=**	**Powder X-ray diffractometry**

List of Tables

List of Schemes

List of Figures

PUBLICATIONS

The following publications have arisen from this thesis

P. Modisha, E. Antunes, J. Mack and T. Nyokong, Improvement of the photophysical parameters of zinc octacarboxy phthalocyanine upon conjugation to magnetic nanoparticles. International Journal of Nanoscience, 12 (2) (2013) 1350010 (10 pages).

P. Modisha, E. Antunes and T. Nyokong, Photodegradation of Orange-G using zinc-octacarboxyphthalocyanine supported on Fe_3O_4 nanoparticles. Journal of Molecular Catalysis A: Chemical. In press.

P. Modisha and T. Nyokong, Fabrication of phthalocyanine-magnetite hybrid nanofibers for degradation of Orange-G. Journal of Molecular Catalysis A: Chemical. In press.

P. Modisha, E. Antunes and T. Nyokong, Photophysical properties of zinc tetracarboxy phthalocyanines conjugated to magnetic nanoparticles. Journal of Nanoscience and Nanotechnology, in press.

CHAPTER ONE

INTRODUCTION

Introduction

The incorporation of nanocomponents into novel hybrid systems opens wide possibilities for design of new nanomaterials with unique properties. In this work, conjugates of magnetite nanoparticles (MNPs) with phthalocyanines (Pcs) are developed for applications in the degradation of an azo dye as a test pollutant. The degradation experiments are done when the conjugates are in solution and also when embedded in electrospun nanofibers. The use of MNPs is motivated by their easiness of recovering and reusing of Pcs bound on their surfaces using a magnet. Moreover Pcs bound to MNPs are less aggregated, thus increasing their photophysical effectivity.

1.1 Magnetite nanoparticles (MNPs)

A nanoparticle is a zero dimensional (0D) particle with all linear dimensions having the same order of magnitude of less than 100 nm. Magnetite nanoparticles have drawn considerable attention in science and engineering because of their non-toxicity, excellent magnetic properties, suspendability in water and their affordability **[1, 2]**. These properties endow them to be used in terabit data storage devices, sensors, catalysis, magnetic resonance imaging (MRI) and therapeutics **[3-7]**. Moreover, magnetite nanoparticles with sizes ranging from 2-20 nm exhibit superparamagnetic properties **[8]**. At this nanoscale, the magnetic moments are in a random motion and they respond quickly to the magnetic field to reach a magnetic saturation and move back to zero when the magnetic field is removed **[9]**.

1.1.1 Applications of magnetite nanoparticle in catalysis

By definition, a catalyst is a substance that speeds up the rate of the reaction without itself being consumed, while a support is a solid material with high surface area, to which a catalyst is affixed. Magnetite nanoparticles have been used both as catalysts and supports. Fischer-Tropsch synthesis (FTS) is well-known in the production of hydrocarbons from a syngas ($CO + H_2$). For this reaction, MNPs supported on activated silicon wafers have been employed as catalysts **[10]**. Moreover, MNPs have been used as supports for *Aspergillus niger* (catalyse), diatomite, magnesiumtetrapyridylporphyrin (MnTPP) and palladium catalysts. These catalysts were designated for hydrogen peroxide decomposition, epoxidation of alkenes, and removal of hexavalent Cr (VI) in water and for the hydrodehalogenation of organic pollutants **[11-17]**. The aim of this work is to combine phthalocyanines with MNPs for use in photocatalysis when in solution or supported on fibers. More importantly, the magnetic properties of MNPs as supports allow facile recovery of the catalyst using a magnet for the catalyst recycling.

1.1.2 Application of MNPs in magnetic resonance imaging (MRI) and hyperthermia (HPT)

Magnetite nanoparticles can be specific to cancerous tissues [Figure 1.1 (I)] depending on the type of the targeting probe attached or by enhanced permeability and retention (EPR) **[18]**. Cancerous tissues retain molecules by EPR due to poor lymphatic drainage. The retention and accumulation of such molecules is much greater in cancer cells when compared to healthy normal cells **[19, 20]**. Magnetic resonance imaging (MRI) **[21]** can be used to view the affected area in the presence of a contrast agent, as depicted in Figure 1.1 (II). In addition MNPs produce heat which damages tumor tissues; this is called hyperthermia (HPT), Figure 1.1 (III). This method takes the advantage of the fact that, tumor cells are more susceptible to elevated

temperatures in the range of 42-45°C than the normal cells **[22]**. HPT is based on the theory that, when exposed to an external alternating magnetic field (AMF), the magnetic moments oscillates, during which process the electromagnetic energy is converted into heat **[23].**

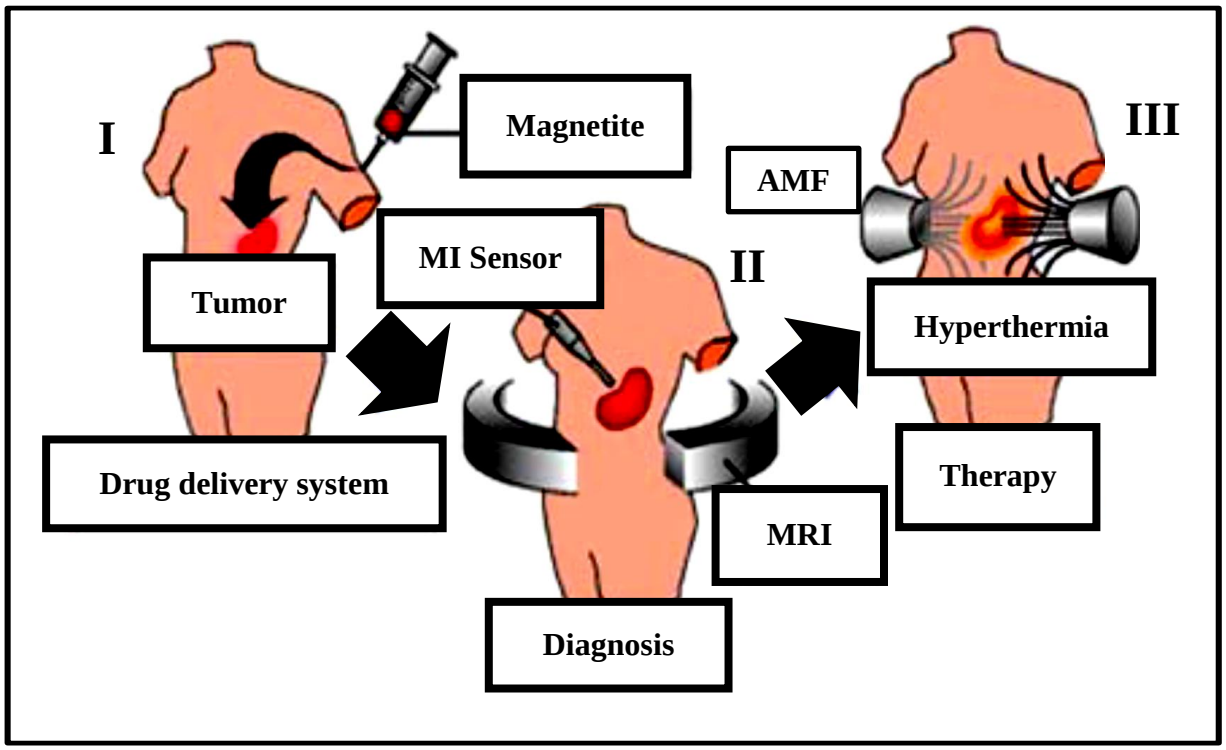

Figure 1.1: Scheme of representation showing drug delivery system (I), diagnosis (II) and therapy (III), using magnetite nanoparticles (MNPs) [21]. MRI=magnetic resonance imaging; MI=magneto impedance; AMF=alternating magnetic field.

1.1.3 Synthesis, stabilization and surface functionalization of MNPs

Various chemical methods such as: thermal decomposition, microemulsion **[24]**, sol-gel **[25]**, hydrothermal reactions **[26]**, flow injection **[27]** and electrospray **[28]** can be used to synthesize magnetite nanoparticles. However, co-precipitation is a conventional method used for small scale and in commercial production **[29]**. This method entails mixing Fe^{2+} and Fe^{3+} (molar ratio of 1:2)

salt solutions followed by the addition of a base for the precipitation of the nanoparticles Eq. 1.1 **[30]**.

$$Fe^{2+} + 2Fe^{3+} + 8OH^- \rightarrow Fe_3O_4 + 4H_2O \ldots\ldots\ldots\ldots (1.1)$$

It is important to stabilize or functionalize nanoparticles to prevent agglomeration, corrosion and intermolecular attraction between them **[31]**. Therefore, functional groups such as: amines, carboxylates, sulfates, phosphates or inorganic materials (Figure 1.2) like silica, gold and gadolinium are known to bind to the surface of MNPs through their surface hydroxyl groups **[32-34]**. These functional groups allows for the dispersion in aqueous or organic media and also for the nanoparticles to be conjugated with biological molecules such as proteins, folic acid and fluorophores (e.g. quantum dots and phthalocyanines). In this work, the water dispersed magnetite nanoparticles were coated with silica and functionalized with 3-aminopropyltriethoxy silane (APTES).

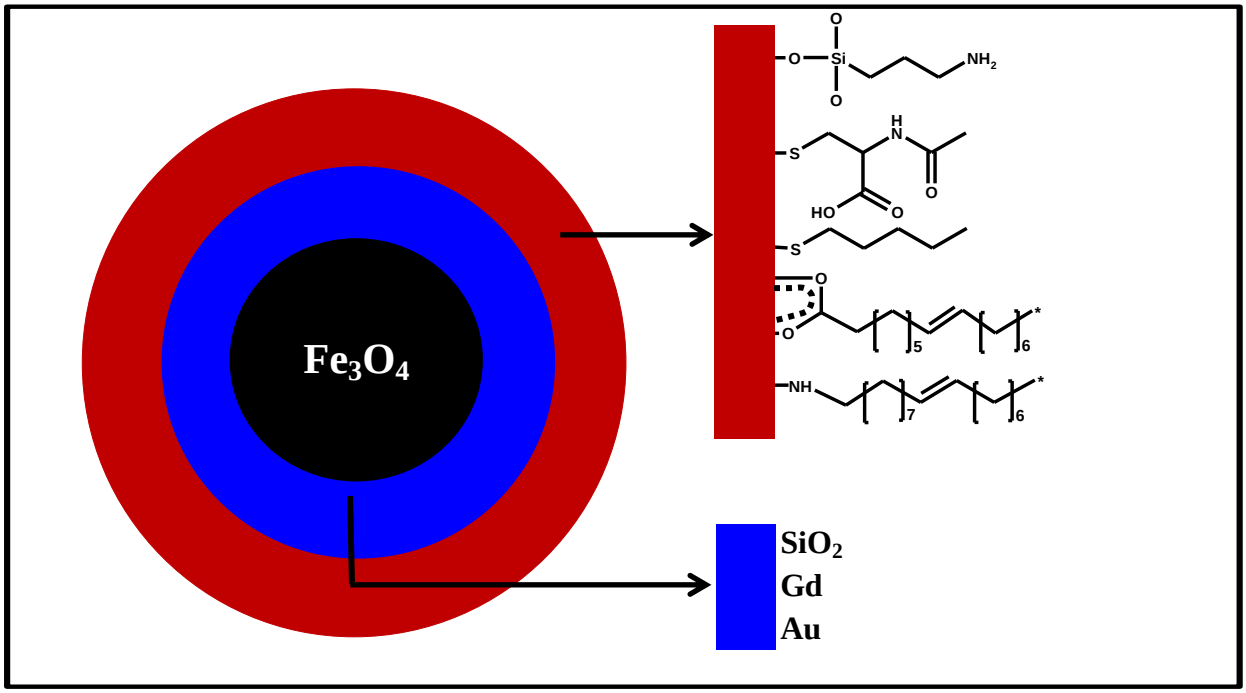

Figure 1.2: Surface modification of MNPs (black), first by materials such as SiO_2, Gd or Au and then by suitable functionalized ligands (red).

1.1.4 Characterization of magnetite nanoparticles

The crystal structure and the size of MNPs can be determined using a powder X-ray diffractometry (PXRD). The MNPs are characterized by their face centered cubic (FCC) lattice crystal structure with hkl Miller indices at (220), (311), (400), (422), (511) and (440) corresponding to their 2θ values at 30 º, 36 º, 43 º, 54 º, 57 º and 63 º, respectively **[35]**. The crystal size is calculated from PXRD pattern (Figure 1.3) using Debye-Scherrer equation (Eq. 1.2) focusing on the (311) peak.

$$D = \frac{0.9\,\lambda}{B\cos\theta} \qquad (1.2)$$

where D is the crystal size, λ is the wavelength of the X-ray using Cu-Kα radiation (λ= 1.541 Å, nickel filter), B is the full width at half maximum (FWHM) and θ is the diffraction angle **[36]**.

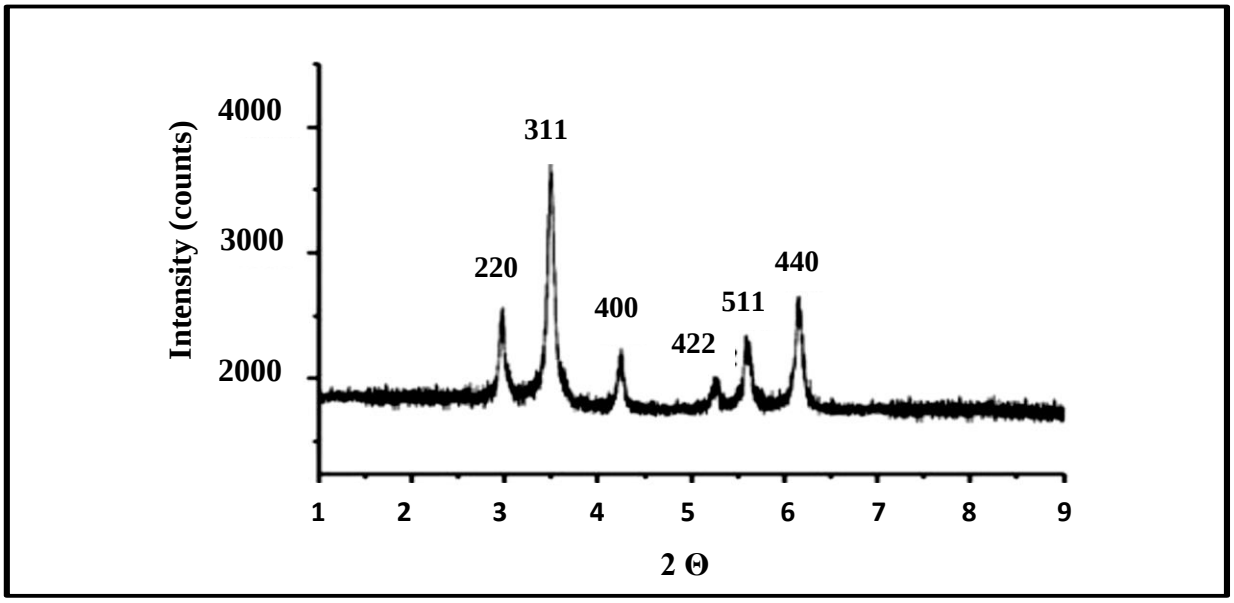

Figure 1.3: PXRD pattern of MNPs prepared by the co-precipitation method [35]

Further confirmation of the nanoparticles size can be done using transmission electron microscopy (TEM) **[37]**. This technique helps to visualize the shape of the nanoparticles, size distribution and their dispersion **[38]**, as shown in Figure 1.4.

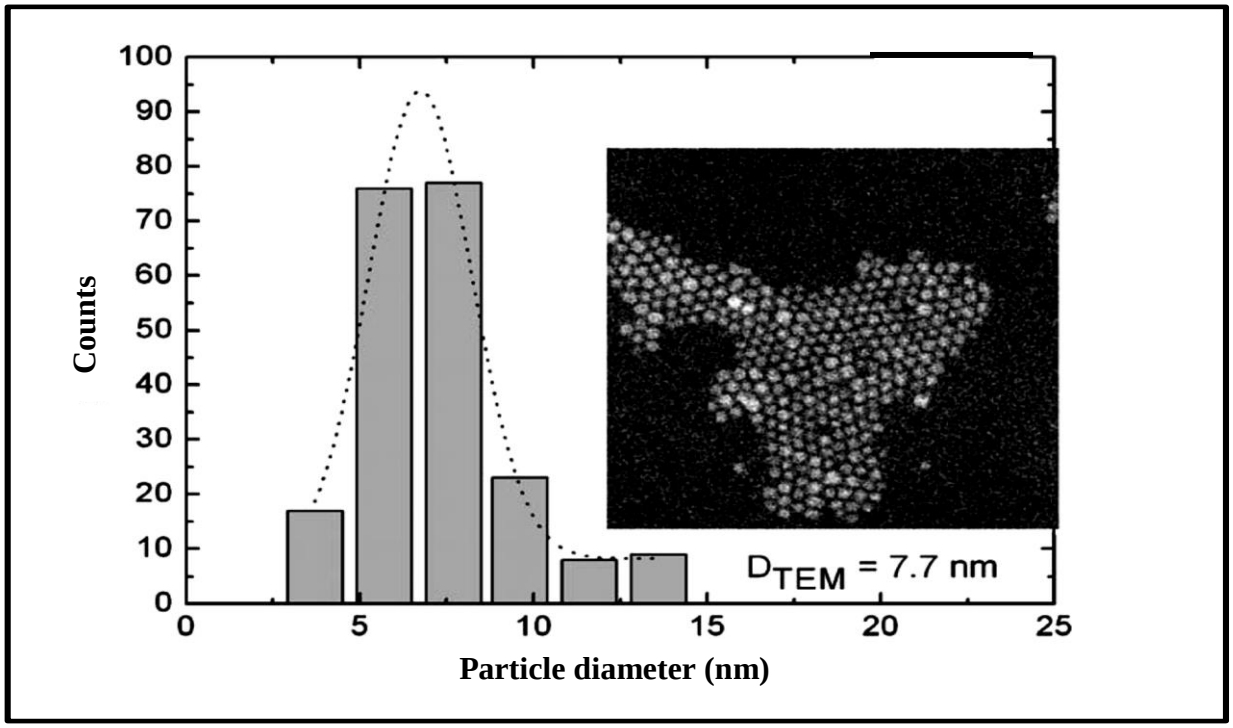

Figure 1.4: The size distribution histogram of MNPs. Inset: TEM image of MNPs [38].

Other techniques including, thermogravimetric analysis (TGA), Fourier transform infrared spectroscopy (FTIR), energy dispersive x-ray spectroscopy (EDS) and Breunner-Ermmet-Teller (BET) can be used to determine the thermal stability, functional groups on the surface, elemental composition and the surface area of the nanoparticles, respectively **[39]**.

1.2 Phthalocyanines (Pcs)

Phthalocyanines are well-known as blue-green dyes which absorb light strongly in the visible region of the spectrum **[40]**. The history of Pcs dates back to 1907 when they were accidentally discovered but unrecognized, as an insoluble bluish by-product during the synthesis of *o*-cyanobenzamide from phthalamide **[41]**. In 1928, iron Pc was also accidentally discovered at the Scottish Dyes Ltd and its structural identification was done by Linstead **[42]**. Seven years later, the structure was confirmed by X-ray crystallography, with the chemical formula $C_{32}H_{18}N_8$ for the metal-free derivative **[43, 44]**. The name 'phthalocyanine' was invented from its precursor phthalic acid derivative 'phthalo' and 'cyanine' from the Greek word for blue. Phthalocyanines have a wide variety of applications because of their diverse chemical, structural, electronic and optical properties. Hence, they have been found useful in many technological applications such as photovoltaic cells **[45]**, optical data storage **[46, 47]**, fuel cells **[48]**, chemical sensors **[49],** catalysis **[50]**, non-linear optics **[51]** and recently in medical applications as photosensitizers for photodynamic therapy (PDT) **[52]** and photodynamic antimicrobial activity (PACT) **[53]**.

1.2.1 Structure of phthalocyanines

Phthalocyanines (Pcs) are aromatic macrocyclic compounds with conjugated system of 18π electrons. Their four isoindole groups are linked together by four nitrogen atoms resulting in a closed ring, Figure 1.5. The structure of the Pc ring **(1)** is comparable to that of naturally occurring porphyrins (Por) **(2)**. The substitution of four meso carbon bridges by nitrogen atoms and the fusion of benzene rings on the pyrrole β−positions of **(2)** results in a phthalocyanine **(1)**

[54], Figure 1.5. It has been reported that over 70 metals or metalloids **[55]** can be coordinated in the central cavity of the metal free Pc (H_2Pc) to form metallophthalocyanines (MPcs).

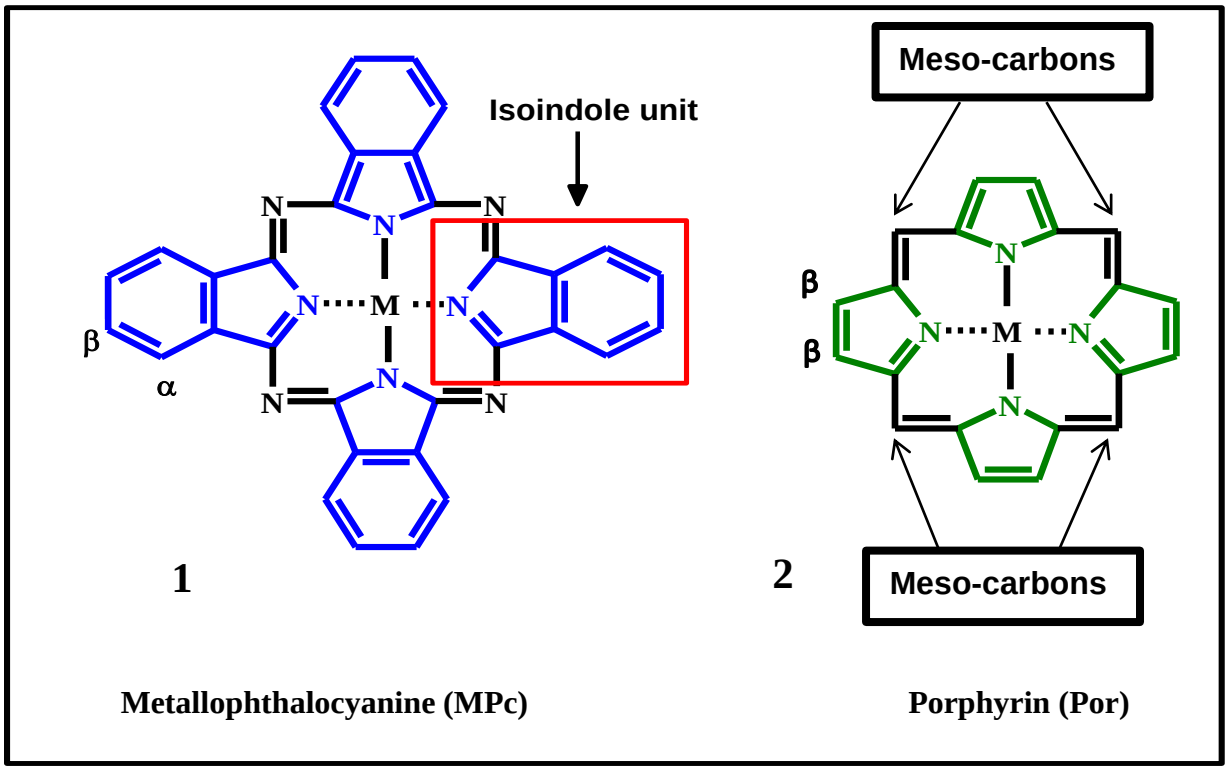

Figure 1.5: The structure of a metallophthalocyanine (MPc) and a porphyrin (Por)

1.2.2 Synthesis of water soluble symmetric phthalocyanines

This work will only compare the well-known metal tetracarboxyphthalocyanine (MTCPc) and octacarboxyphthalocyanine (MOCPc); as such their general syntheses protocols are discussed. MTCPc **(5)**, Scheme 1.1, is obtained from tetracarboxy amido-substituted metallophthalocyanine (MTCAPc) **(4)** which is an intermediate formed from reacting trimellitic anhydride **(3)**, urea, ammonium molybdate and a metal salt, followed by treatment with potassium hydroxide at elevated temperature **[54-60]**. The octacarboxylic acid-substituted metallophthalocyanines (MOCPc) **(8)** are obtained by reacting pyromellitic dianhydride **(6)**, urea (as a solvent and a

source of nitrogen), 1, 8-diazabicyclo[5.4.0]undec-7-ene (DBU) (as a catalyst) and a suitable metal salt, Scheme 1.2 **[54, 55]**.

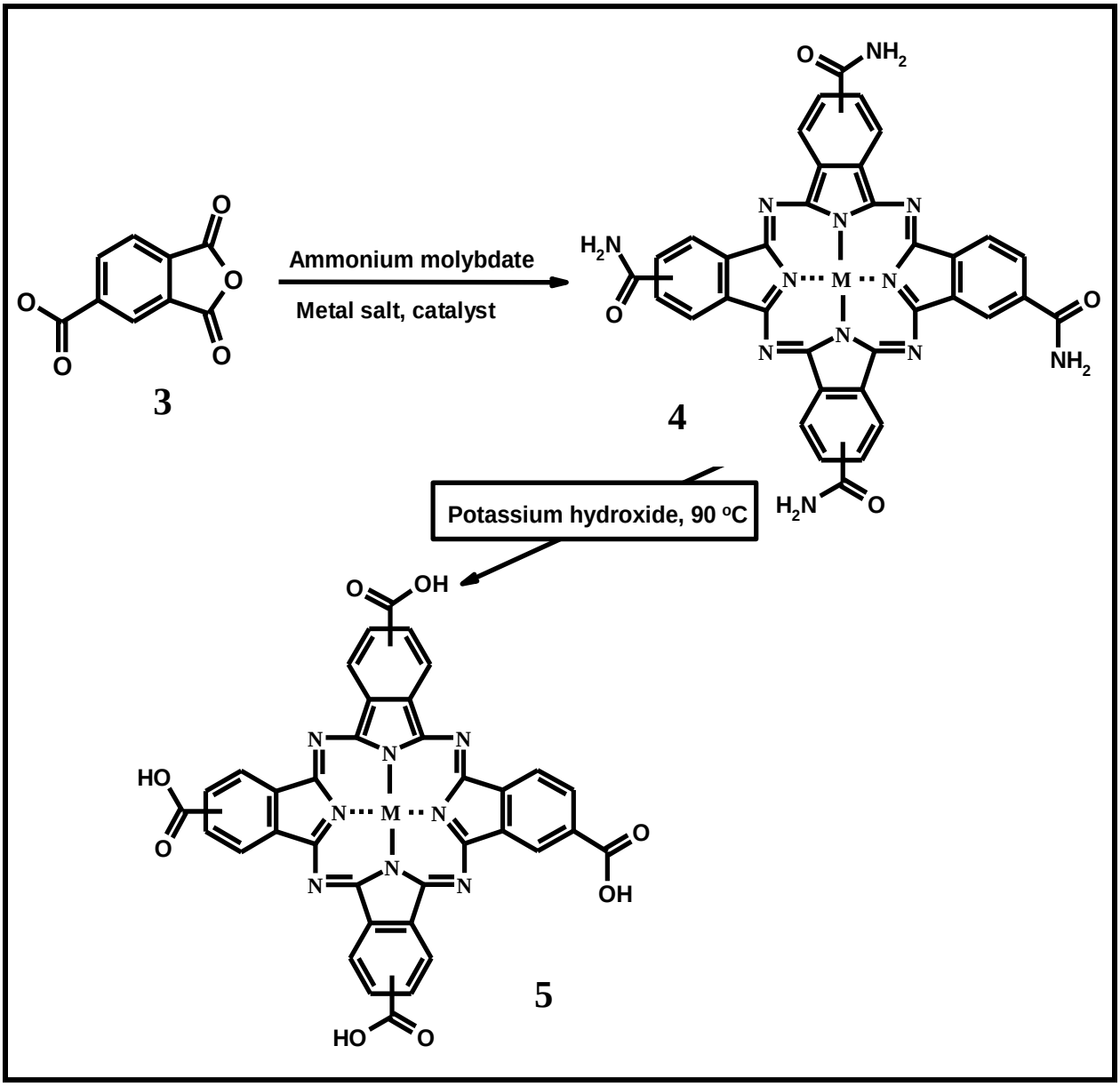

Scheme 1.1: Synthesis of metal-tetracarboxy metallophthalocyanine (MTCPc) [54].

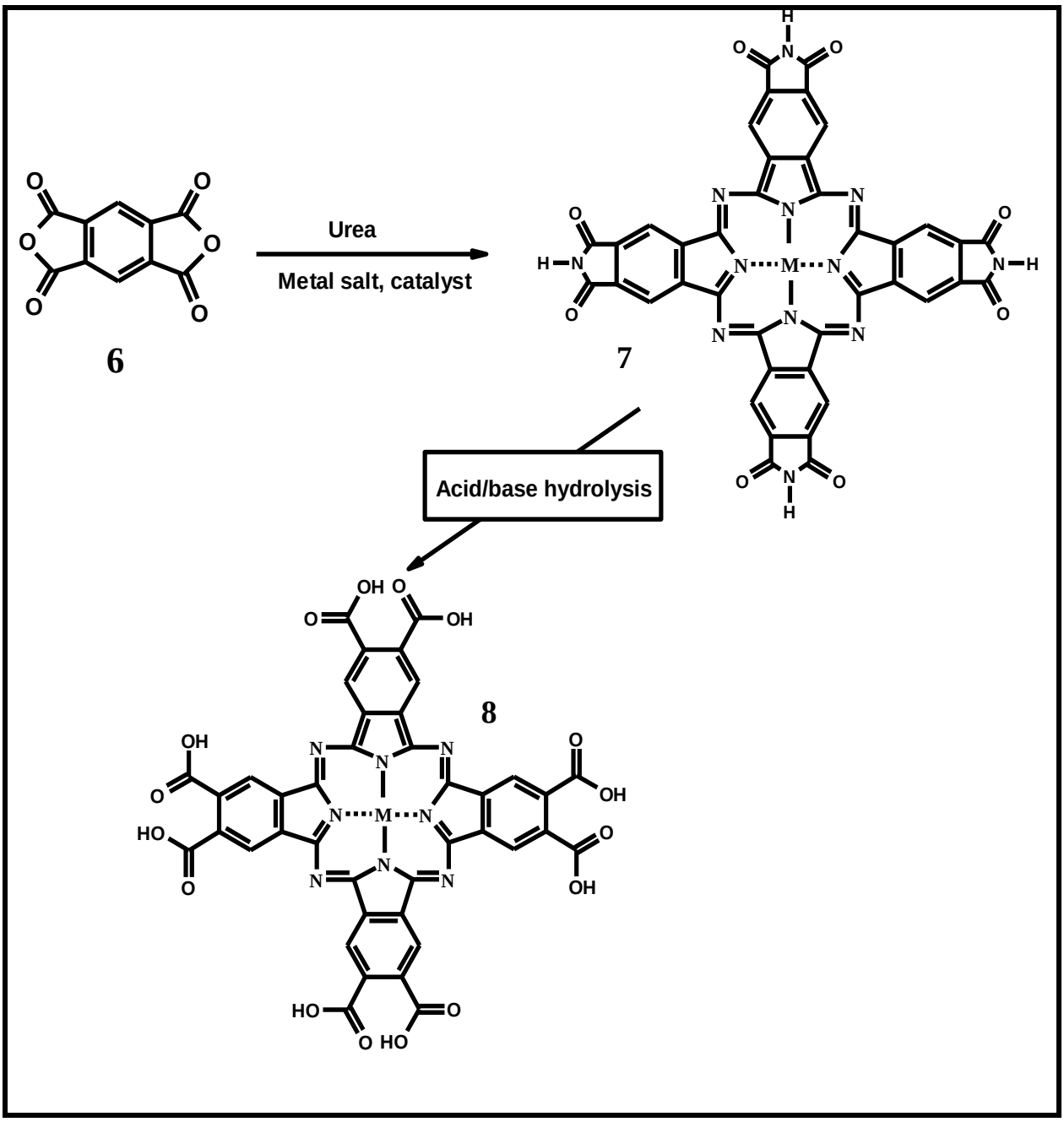

Scheme 1.2: Synthesis of metal-octacarboxy phthalocyanine (MOCPc) [54].

1.2.3 Electronic absorption spectra of Pcs

A phthalocyanine is characterized by an intense and isolated absorption band in the red region of the electromagnetic spectrum **[61]** called the Q-band, with its vibrational bands ($Q_{vib.}$), Figure 1.6. The B-band appears between 300 - 400 nm and is a less intense band when compared to the Q-Band. The B-band is broad due to the overlapping of the B_1 and B_2 bands. Other absorption bands such as N, L, and C are also present and they appear at a lower energy **[62, 63]**, only in transparent solvents such as chloroform.

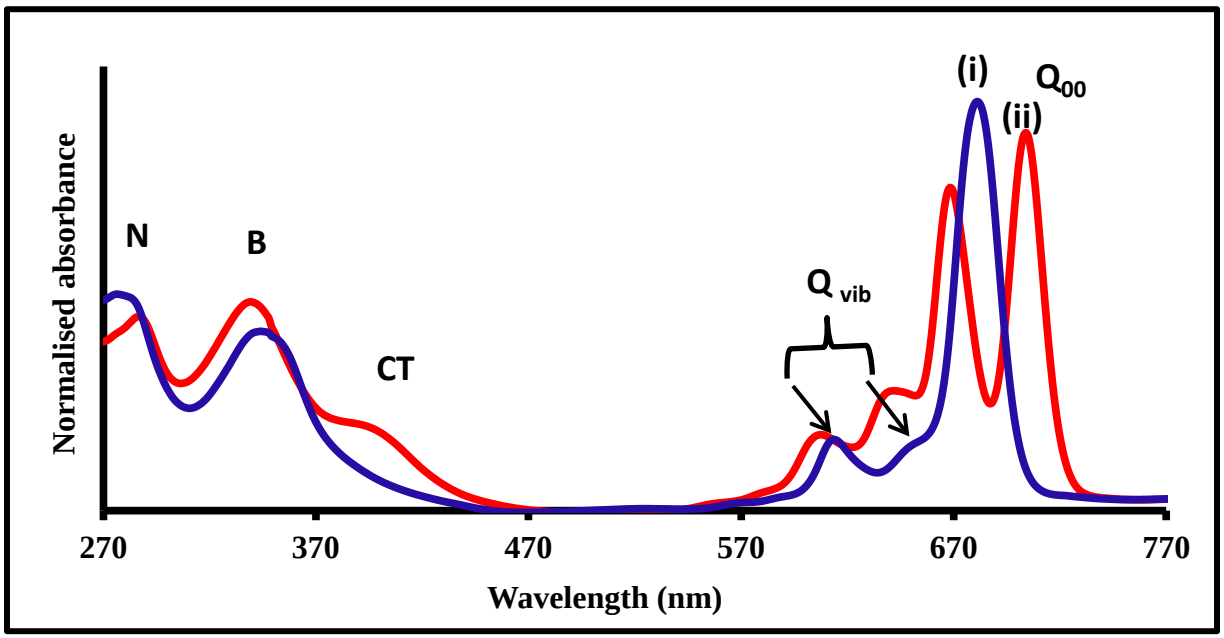

Figure 1.6: Ground state absorption spectra of metallated (i blue) and metal free (ii red) Pcs

The bands in the absorption spectrum are due to π-π* electronic transitions in the Pc ligand and the assignment of the Q and B bands is based on Gouterman's four-orbital model **[64-67]**. In this model, the top two highest occupied molecular orbitals (HOMO) and the degenerate lowest unoccupied molecular orbital (LUMO) are taken into account **[68]**, Figure 1.7. The Q-band

absorption is due to a transition from the a_{1u} of the HOMO to a doubly degenerate transition e_g of the LUMO, while a transition from a_{2u} or b_{2u} to the e_g of the LUMO results in the B-band absorption.

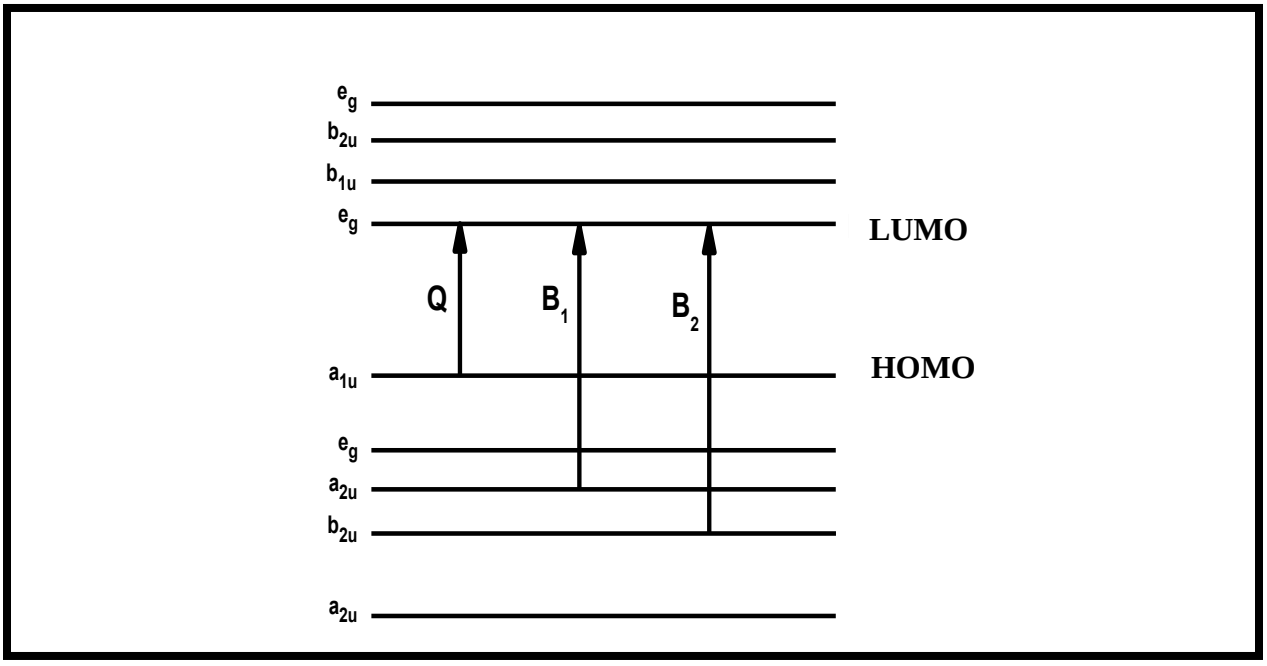

Figure 1.7: Electronic transitions in MPcs showing the origin of Q and B absorption bands

For the metal-free phthalocyanine (H_2Pc), the Q band splits into a doublet (Figure 1.6). This splitting of the Q band is due to the low symmetry (D_{2h}) of H_2Pc in comparison with metallophthalocyanine (D_{4h}). The LUMO orbital loses degeneracy due to the presence of the two core protons giving rise to a split Q- band. Other absorption bands present between the Q and B bands occur when the metal d-orbitals lie within the HOMO-LUMO gap (Figure 1.6) of the Pc ring, and these are assigned as charge-transfer transitions (CT) **[68]**. A charge transfer from an electron rich ligand to an electron poor metal is known as a ligand to metal charge transfer (LMCT) while a transfer from metal to ligand is a metal to ligand charge transfer (MLCT).

1.2.4 Aggregation of phthalocyanines

Aggregation is described as a coplanar association of rings progressing from a monomer to a dimer and higher order complexes **[69, 70]**. Aggregation of MPcs depends on concentration, nature of the solvents and substituents, metal ions and temperature **[71]**. Water soluble octacarboxylated Pc derivatives show no aggregation, however tetracarboxylated derivatives are 'aggregated. According to Kasha's molecular exciton theory **[72]**, the absorption bands of aggregates will be blue shifted with respect to the monomer band when the polarization axes of the monomer and the line of the molecular center of the aggregate is larger than 54.7 ^{o}. The so called H-aggregation occurs when the angle is 90 ^{o} whereby the molecules are face to face, Figure 1.8. When the angle is smaller than 54.7 ^{o} the aggregated peak is red shifted and this is called J-type aggregation. The aggregation due to cofacial arrangement of Pc rings (H-type) is more common whereas the J-type is very rare **[73, 74]**. The nanoparticles moments could either be parallel or perpendicular to the Pc's moments resulting in blue or red shifting.

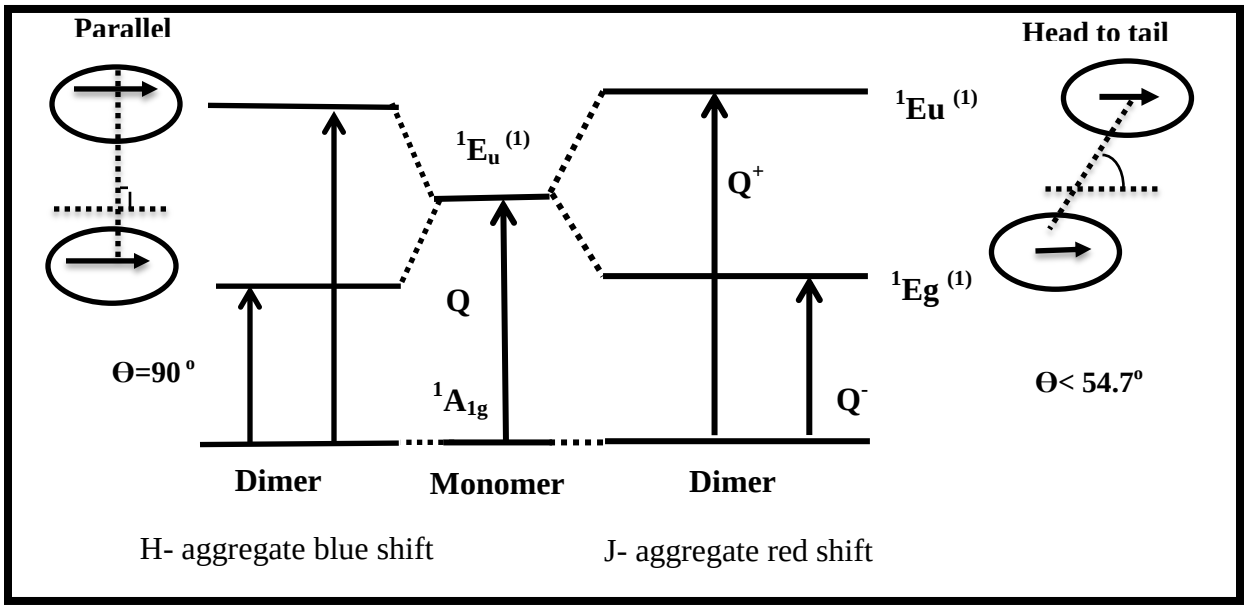

Figure 1.8: Energy levels showing the transition in aggregated MPc complexes [73].

1.2.5 Photophysicochemical properties of phthalocyanines

The photophysical processes that take place when an MPc molecule absorbs light are best illustrated by the Jablonski diagram **[75]**, Figure 1.9. After absorption and population of the S_1 state, the molecule can relax back to its ground state by releasing a photon resulting in fluorescence (F) emission or it can undergo radiationless, vibrational relaxation (VR) and internal conversion (IC) back to the ground state, or inter-system crossing (ISC) to the first triplet state, T_1. The latter may be followed by IC and phosphorescence (P) back to the S_1 state. ISC is a spin-forbidden transition, but occurs through spin-orbit coupling, which relaxes the spin selection rule **[76-78]**. For this reason, the intensity of the spin-forbidden transitions increases with an increase in the atomic number of the metal atom in the complex, a phenomenon known as the 'heavy-atom' effect **[76, 78]**, due to enhanced spin-orbit coupling. Heavy atoms or paramagnetic compounds such as MNPs (magnetite nanoparticles) increase ISC, improving triplet quantum yields and consequently the singlet oxygen yields. This falls under the main important aspects of this thesis, because singlet oxygen (the chief cytotoxic species) is needed for photocatalysis. Thus the aim of this thesis is to conjugate MNPs to Pcs in order to increase the singlet oxygen quantum yield due to the heavy atom effect.

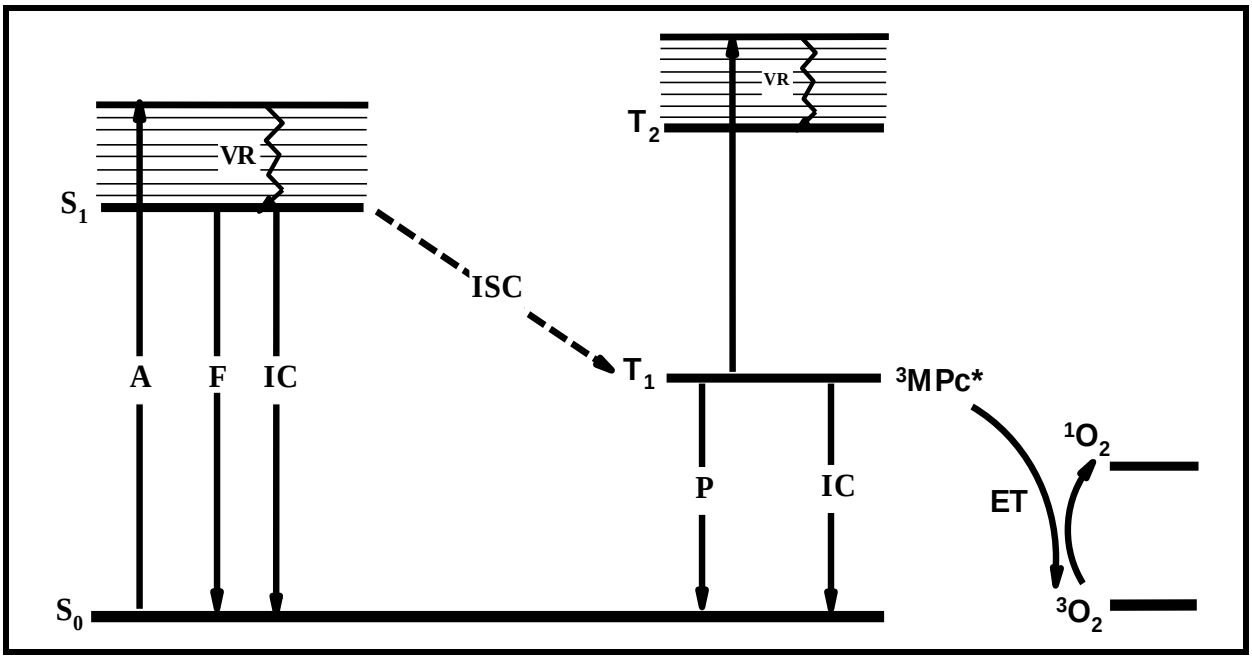

Figure 1.9: Simplified Jablonski diagram for MPcs, showing the origin of the transitions. A = absorption, IC = internal conversion, F = fluorescence, VR = vibrational relaxation, ISC = inter-system crossing, P = phosphorescence, T-T absorption = triplet to triplet absorption. S_0 = singlet ground state, S_1 = first singlet excited state, T_1 = first triplet excited state, T_2 = second triplet excited state, ET= Electron Transfer [75].

1.2.5.1 Fluorescence quantum yield (Φ_F) and fluorescence lifetime (τ_F)

The fluorescence properties of MPcs for example: spectral shifts, fluorescence quantum yield and lifetime can be affected by aggregation, nature of solvent, pH, halogenation, electronic energy transfer and the nature of the central metal **[71]**. Fluorescence quantum yield (Φ_F) is defined as the number of emitted photons relative to the number of absorbed photons. Fluorescence lifetime (τ_F) is the average time an excited fluorophore spends in the excited state before it decays back to its ground state **[79]**. Fluorescence quantum yield (Φ_F) may be determined by comparison with a standard using Eq. 1.3 **[80]:**

$$\Phi_F = \Phi_{F_{std}} \frac{F.A_{std}n^2}{F_{std}.A.n_{std}^2} \quad (1.3)$$

where F and F_{Std} are the areas under the fluorescence curves for sample and standard (e.g. ZnPc), respectively. A and A_{Std} are the absorbances of the sample and reference at the excitation wavelength respectively, while n and n_{Std} are the refractive indices of solvents in which the sample and reference were dissolved, respectively.

1.2.5.2 Triplet quantum yield (Φ_T) and lifetime (τ_T)

A comparative method **[81]** using a standard may be employed for the calculations of the triplet quantum yield (Φ_T), Eq. 1.4.

$$\Phi_T = \Phi_T^{Std} \frac{\Delta A_T.\varepsilon_T^{Std}}{\Delta A_T^{Std}.\varepsilon_T} \quad (1.4)$$

where ΔA_T and ΔA_T^{Std} are the changes in the triplet state absorbances of the Pc derivative and the standard respectively; ε_T and ε_T^{Std}, the triplet state molar extinction coefficients for the Pc derivative and the standard respectively; Φ_T^{Std}, the triplet quantum yield for the standard e.g. ZnPc. ε_T and ε_T^{Std} are determined from the molar extinction coefficients of their respective ground singlet state (ε_S and ε_S^{Std}), the changes in absorbances of the ground singlet states (ΔA_S and ΔA_S^{Std}) and changes in the triplet state absorptions, (ΔA_T and ΔA_T^{Std}) according to Eqs. 1.5a and 1.5b:

$$\varepsilon_T = \varepsilon_s \frac{\Delta A_T}{\Delta A_S} \qquad (1.5a)$$

$$\varepsilon_T^{Std} = \varepsilon_S^{Std} \frac{\Delta A_T^{Std}}{\Delta A_S^{Std}} \qquad (1.5b)$$

1.2.5.3 Singlet oxygen quantum yield (Φ_Δ) and lifetime (τ_Δ)

MPc complexes are well known as photocatalysts (goal of this work) for many reactions such as: epoxidation of alkenes, transformation of alkanes and degradation of water pollutants **[82-84]**. Singlet state oxygen produced by triplet state molecules is the chief cytotoxic species in photocatalytic reactions through Type II mechanisms, Scheme 1.3.

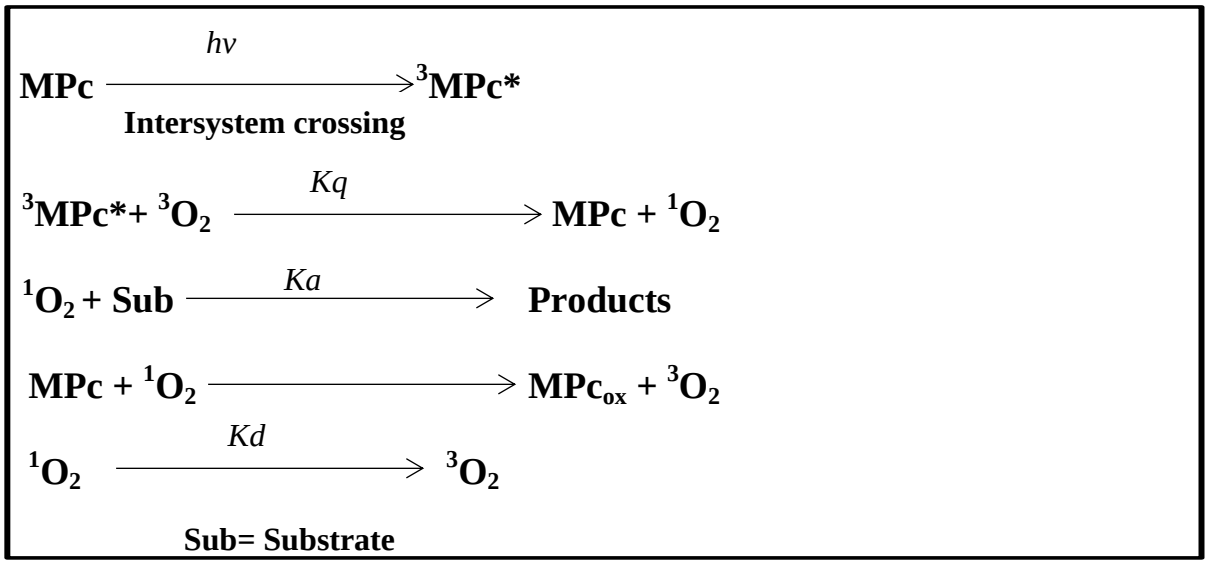

Scheme 1.3: Type II reaction mechanism for singlet oxygen ($^1O_2$) generation by irradiation of MPc.

The excited triplet state of the MPc can also interact with the ground state molecular oxygen or the substrate molecules to generate superoxide and hydroperoxyl radicals, which subsequently oxidizes the substrate, Type I mechanism (Scheme 1.4).

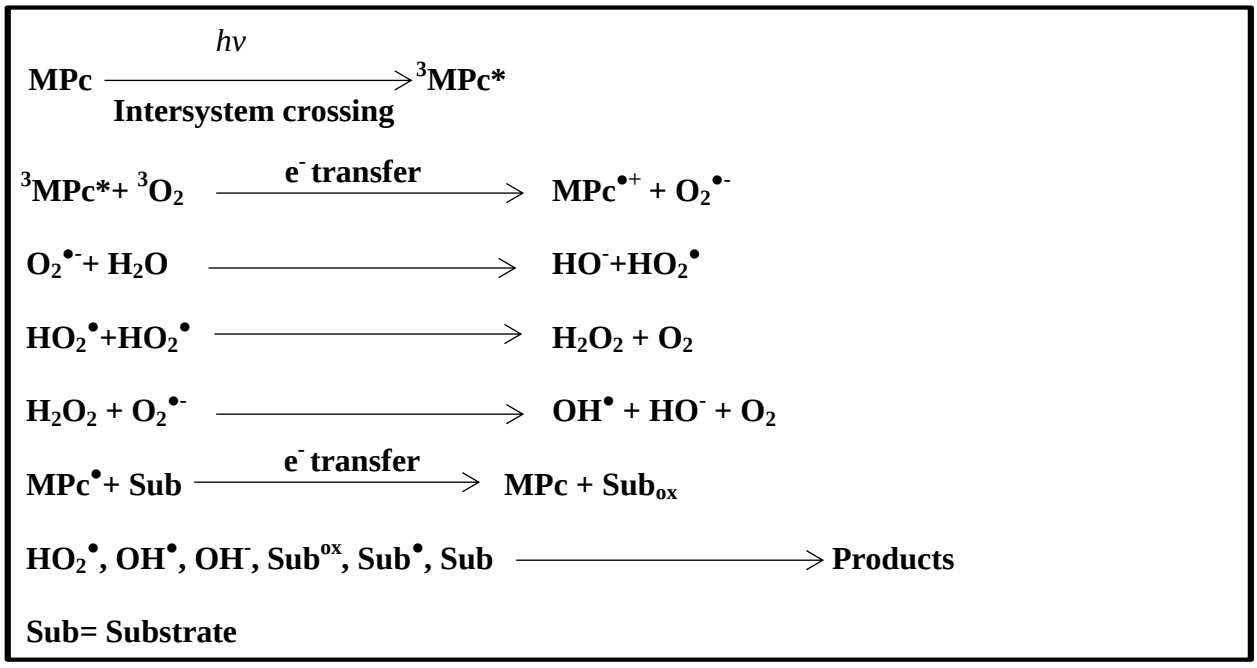

Scheme 1.4: Type I reaction mechanism by free radical production.

It is well known that Type II is more common in photoinitiated oxidation reactions; therefore the magnitude of singlet oxygen quantum yield (Φ_Δ) is determined. The singlet oxygen quantum yield can be determined by a chemical method using anthracene-9, 10-bis-methylmalonate (ADMA) as a quencher in aqueous solvents. By employing the comparative method, the singlet oxygen quantum yield of the phthalocyanine can be determined according to Eq. 1.6 **[85, 86]:**

$$\Phi_\Delta = \Phi_\Delta^{Std} \frac{W I_{Abs}^{Std}}{W^{Std} I_{Abs}} \qquad (1.6)$$

where Φ_Δ^{std} is the singlet oxygen quantum yield for the standard, W and W^{Std} are the ADMA photobleaching rates in the presence of MPc and the standard (e.g. AlPcSmix a mixture of sulphonated aluminium phthalocyanines), respectively. I_{Abs}^{Std} and I_{Abs} are the rates of light absorption by the MPc derivative and standard, respectively.

Alternatively, singlet oxygen luminescene method (SOLM) can also be employed to determine the singlet oxygen quantum yield. In this method sodium azide is used as a singlet oxygen quencher. The time resolved phosphorescence decay curve of singlet oxygen at 1270 nm determines the singlet oxygen quantum yield **[87]**. The dynamic course of $^1O_2$ concentration can be clearly recorded, following Eq. 1.7 as described theoretically in the literature **[88]**:

$$I(t) = B\frac{\tau_D}{\tau_T - \tau_D}[e^{-t/\tau_T} - e^{-t/\tau_D}] \qquad (1.7)$$

where I(t) is the phosphorescence intensity of singlet oxygen ($O_2(^1\Delta_g)$) at time t, τ_D is the lifetime of $O_2(^1\Delta_g)$ phosphorescence decay, τ_T is the triplet state lifetime and B is a coefficient involved in sensitizer concentration and singlet oxygen quantum yield. The singlet oxygen quantum yield, Φ_Δ, of the phthalocyanine is then determined using Eq. 1.8 **[88]**:

$$\Phi_\Delta = \Phi_\Delta^{Std} \cdot \frac{B}{B^{Std}} \qquad (1.8)$$

where Φ_Δ^{Std} is the singlet oxygen quantum yield for the standard, for example AlPcSmix in water, B and B^{Std} are the coefficients of the sample and standard, respectively. The singlet oxygen lifetime (τ_Δ) is determined by fitting the decay curves using Origin Pro 8 software. Only the SOLM method was used to determine the singlet oxygen quantum yield for Pc or Pc-AMNPs in solution.

To determine the singlet oxygen quantum yield in a fiber, a direct method can also be used, where the quantum yields (Φ_{ADMA}) are calculated using Eq. (1.9) **[89]**.

$$(\Phi_{ADMA}) = \frac{(C_o - C_t)V_R}{I_{Abs}\ .t} \qquad (1.9)$$

where C_0 and C_t are the quencher concentrations prior to and after irradiation, respectively; V_R is the solution volume; t is the irradiation time per cycle and I_{abs} is defined by Eq. (1.10).

$$I_{Abs} = \frac{\alpha.A.I}{N_A} \qquad (1.10)$$

where $\alpha = 1 - 10^{-A(\lambda)}$), A ($\lambda$) is the absorbance of the sensitizer at the irradiation wavelength, A is the irradiated area in cm^2, I is the intensity of light and N_A is the Avogadro's constant. The absorbance used for Eq. 1.10 is that of the phthalocyanines in the fibers. The singlet oxygen quantum yields (Φ_Δ) were calculated using Eq. (1.11) **[89].**

$$\frac{1}{\Phi_{ADMA}} = \frac{1}{\Phi_\Delta} + \frac{1}{\Phi_\Delta}.\frac{k_d}{k_a}.\frac{1}{[ADMA]} \qquad (1.11)$$

where k_d is the decay constant of singlet oxygen and k_a is the rate constant for the reaction quencher with $^1O_2$ ($^1\Delta_g$). The intercept of the plot of 1/ Φ_{ADMA} versus 1/ [ADMA] gives $1/\Phi_\Delta$.

1.2.6 Photocatalytic behavior of Pcs

Phthalocyanines have been used as photocatalysts for many pollutants including phenols, thiols etc. **[71]**, but their use as photocatalyts for degradation of azo dyes is still limited, Table 1.1 **[90-94].** The conjugates of Pcs with MNPs are few (as shown in Table 1. 2) **[95-100]**, hence they are explored in this work. The advantage of using MNPs as supports for Pc is that they allow for the facile recovery of the catalyst using a magnet. Tables 1.1 and 1.2 also show that ZnOCPc, ZnTCPc, ZnOCPc-MNPs and ZnTCPc-MNPs conjugates have never been used as a photocatalysts for degradation of an azo-dye. For this reason, we aim to explore these

compounds for the first time. The mechanism for degradation of an azo dye is shown by Scheme 1.5 **[101]**. The singlet oxygen abstracts a hydrogen atom from the NH group of the hydrazine tautomer (II). The formed hydroperoxide radical combines with the resulting hydrazyl radical (III) to give (IV), which decomposes to yield product (V), a 1, 2-naphthaquinone and the diazonium ion (VI). The latter (VI) then breaks down to benzene and nitrogen.

Table 1.1: Phthalocyanines as photocatalysts for azo dyes in solution and in supports

Photocatalyst	**Fiber** **Support**	**Analyte**	**Φ_{Δ}**	**Ref.**
Copper(II) phthalocyanine tetrasulfonate/ TiO_2 **Iron (II) phthalocyanine tetrasulfonic acid**	**Polymetha-crylate**	**Orange (II)**	**–**	**[90]** **[91]**
Iron(II)-tetranitrophthalocyanine/ TiO_2 **Zinc(II)tetrakis[4(methylpyridyloxy)]phthalocya-nine**	**Polyvinyl-pyrrolidone** **Polysulfone**	**Methyl-orange**	**0.21**	**[92]** **[93]**
Zinc-tetrakis-(β-benzylmercapto)-phthalocyanine	**Polystyrene**	**Orange-G**	**0.13**	**[94]**

Table 1.2: Phthalocyanines conjugated to magnetite nanoparticles and their applications

Conjugate	Applications	Φ_Δ	Ref.
Zinc-phthalocyanine-MNPs	**Potential use in PDT & HPT**	**0.67**	**[95]**
Silicon-phthalocyanine-MNPs		**0.24**	**[96]**
Aluminium-phthalocyanine-MNPs Aluminum-phthalocyaninetetrasulfonate-MNPs		**0.28**	**[97]**
Iron-tetracarboxyphthalocyanine-MNPs	**Oxidation of hydrocarbons and sulfides**		**[98]**
Aluminium-tetracarboxyphthalocyanine-folate-MNPs	**Imaging/ cell targeting/ drug delivery & PDT**		**[99]**
Copper-phthalocyaninetetrasulfonate-MNPs	**Photodegradation of Rhodamine B and methyl orange**		**[100]**

Sub Aim:

The aim is to synthesize the MNPs, then link them to ZnOCPc or ZnTCPc through an amide bond taking the advantage of carboxyl groups in the peripheral positions of the Pc and also the amino functionalized MNPs. The conjugates are used for degradation of an azo dye. The use of MNPs allows for easy separation of the catalyst using a magnet so that the catalyst can be reused.

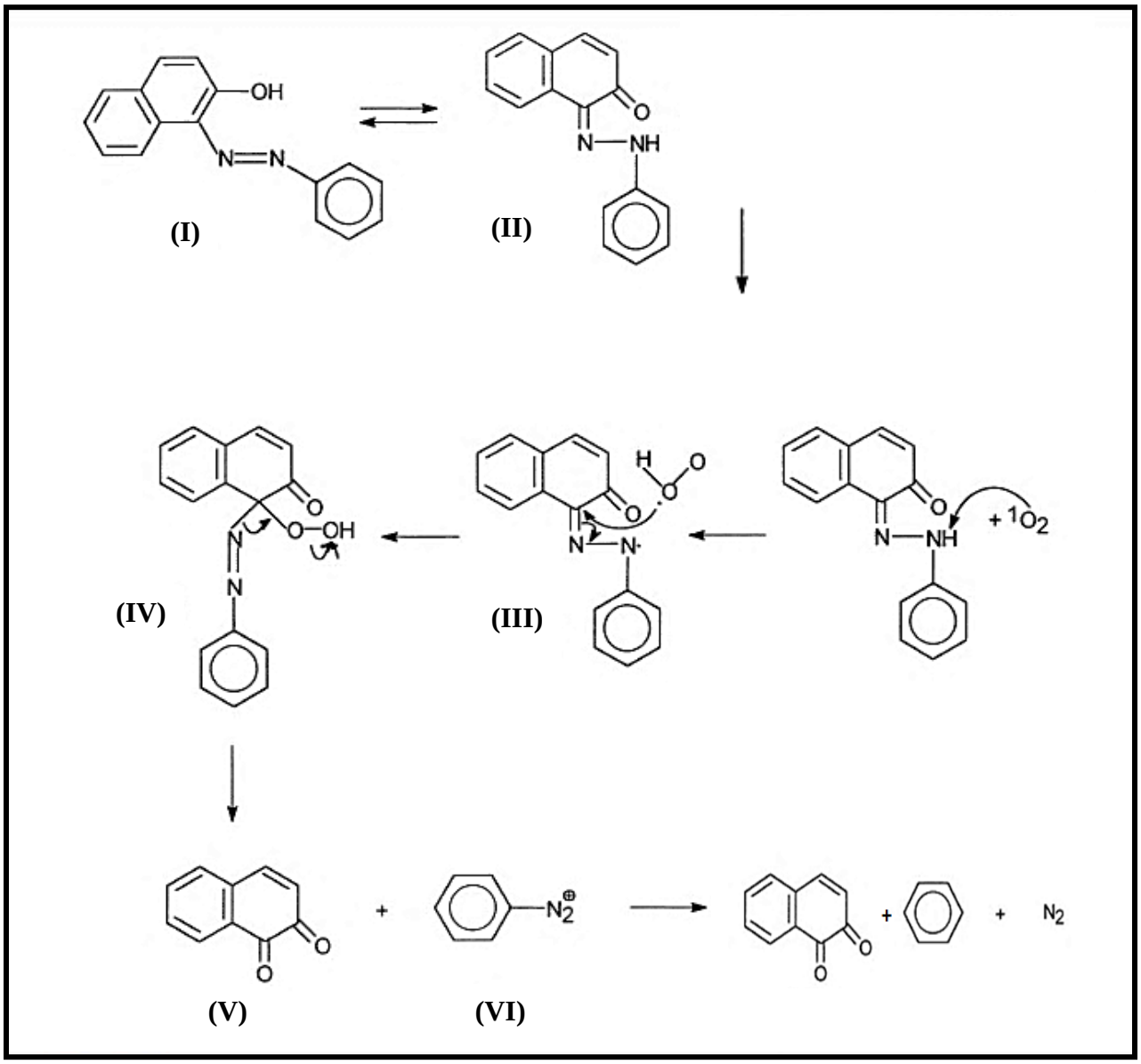

Scheme 1.5: Representative mechanism for photo-oxidation of 1-arylazo-2-naphthol (azo dye) via a singlet oxygen Type II mechanism [101].

1.3 Background on azo dyes: water pollution and degradation

Azo dyes are diazotized amines coupled to an amine or phenol, with one or more azo bonds (–N=N–). Almost all dyestuffs used by textile industries are azo dyes, and they are also used in printing, food, paper making and cosmetic industries. An estimate was made in the 1980's, that 280,000 tons of textile dyes were annually discharged into industrial effluents worldwide **[102]**. Azo dyes are toxic, carcinogenic and mutagenic **[103]**. They can also affect the aquatic ecosystem, decreasing the light penetration and gas dissolution in lakes, rivers and other bodies of water **[104]**. In recent years, advanced oxidation processes (AOPs) are a matter of growing interest for the destruction of these dyes **[105]**. AOPs are based on *in situ* generation of very powerful oxidizing agents such as hydroxyl radicals, which are highly effective for removing organic dyes from water. AOPs such as Fenton reaction **[106]**, wet air oxidation **[107]**, ozonation **[108]**, electrolysis **[109]**, photolysis **[110]**, radiolysis **[111]** and their combinations **[112, 113]** are widely studied for the decomposition of various kinds of hazardous organic compounds. Among these processes photolysis is mostly used successfully, as it is comparatively cheap and uses easy to handle reagents, hence it is employed in this work.

1.4 Electrospinning

Electrospinning was first proposed in the 20 th century. Zeleny **[114]** described the principles of electrospinning in 1914. Then, in 1969 Taylor brought the fundamental concepts of the Taylor cone, and the voltage values at which Taylor cones are formed **[115]**. Electrospinning is regarded as a simple and inexpensive method for making ultrafine fibers of a diameter ranging from 100 nm to 1μm. These ultrafine fibers have various characteristics such as small pore size,

large surface area and the possibility for surface functionalization **[115]**. Thus, the process has generated much interest among scientists and engineers. Electrospun fibers are finding widespread applications in the emerging areas of nanotechnology and biomedical research **[116, 117]**, drug encapsulation and delivery **[118–120]**, tissue engineering **[121–123]** etc.

1.4.1 Basics of electrospining

In an ordinary electrospinning process, a high electrostatic potential from a high-voltage power supply is applied to the polymer solution across a finite distance between a conductive nozzle and a grounded collector **[124]**. The Coulombic repulsion forces existing in a polymer solution between the charges of similar polarity destabilizes a spherical droplet located at the tip of the nozzle to form a helical coil (i.e. Taylor cone) **[124]**, Figure 1.10. When the voltage exceeds the critical value, a charged droplet overcomes its own surface tension to form a jet that undergoes a whipping instability to split into ultrafine fluids **[124, 125**]. For large scale production of fibers, multinozzle electrospinning setup maybe used; this method differs from the mononozzle setup by the number of nozzles, with the general methodology remaining the same. Another basic principle for a successful electrospinning is to obtain steady state conditions. Electrospinning is regarded to be in steady state if the amount of polymer that is transported through the needle per unit of time equals the amount of polymer that is deposited as nanofibres on the collector per unit of time **[119]**. This definition is two-fold. The first condition is that relative to time, the entire polymer that is spun from the needle capillary and then collected, is converted into fibers, without beads or drops in the structure; the second condition is a stable and time invariant Taylor cone **[119, 120]**. Steady state electrospinning allows for the long-term stability needed for reproducibly of samples of any desired size.

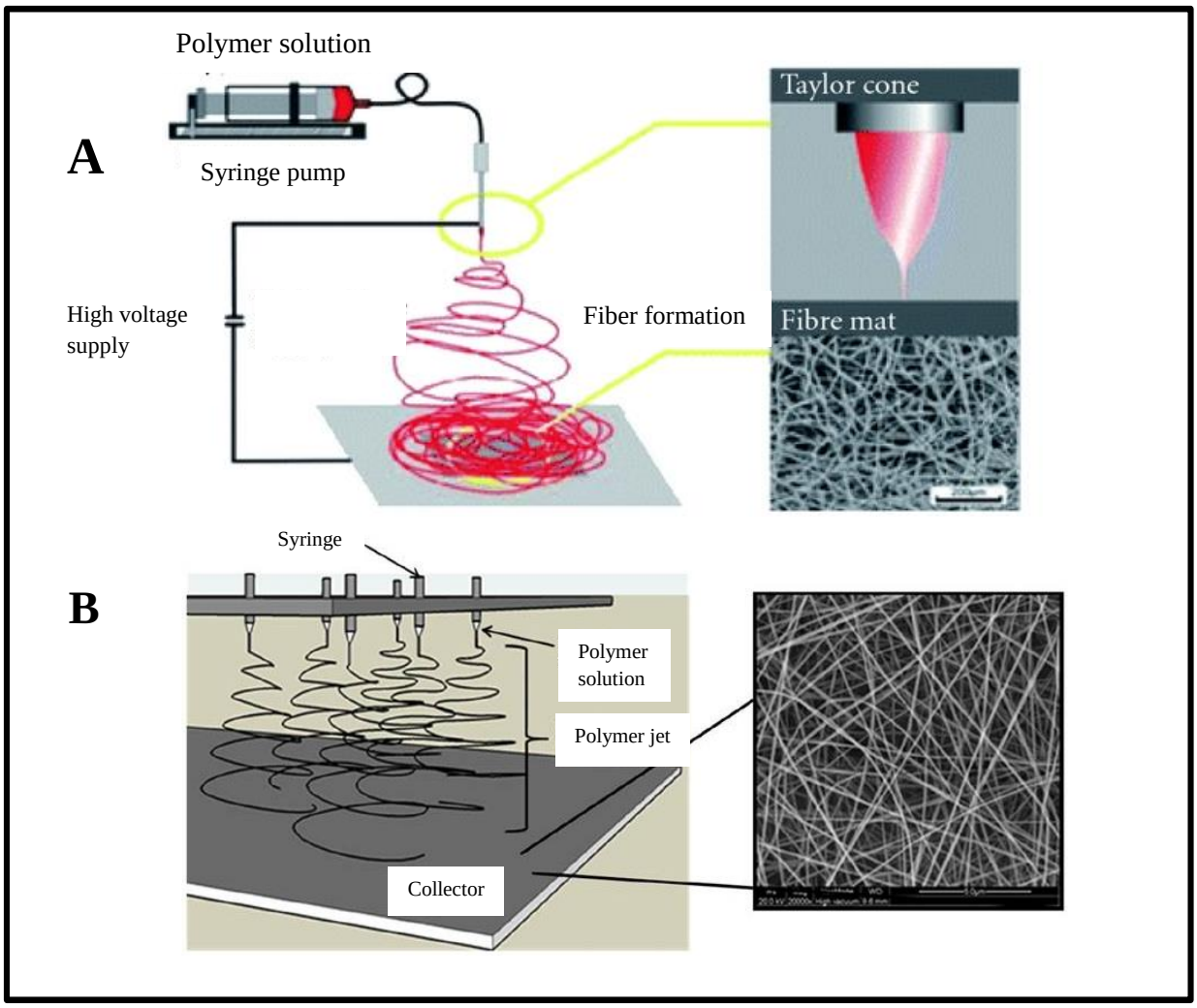

Figure 1.10: Schematic diagram showing (A) mononozzle and (B) multinozzle electrospinning setups [126].

1.4.2 Factors affecting electrospinning

Many factors can impact the electrospinning process, including the nature of the polymer itself (polymer length and its distribution), the properties of the polymer solutions (concentration, viscosity, conductivity and surface tension). The nature of the solvent or mixtures of solvents are also important in addition to the nature of the polymer **[117]**. The process parameters (applied

voltage, flow rate, distance between capillary tip and collection screen, temperature and humidity of the environment) also affect the electrospinning process **[118]**.

1.4.3 Phthalocyanines on electrospun nanofibers

Many phthalocyanines have been electrospun into fibers with their photoactivity still maintained within the polymer fiber, and without separation of the phthalocyanine from the fiber during electrospinning **[126]**. Thus reproducible behavior in any application is expected. Numerous polymers have been used in fabricating phthalocyanine/ fibers (as shown in Table 1.3) **[127-132]**. In our case we chose polyamide-6 (PA-6) because of its relative flexibility, significant stiffness and resistance to chemical degradation and heat. These properties allow us to use the fibers in any media or pH without the fiber being degraded. Phthalocyanines were also covalently linked to polymer fibers, but with a low singlet oxygen yield **[123]**. Phthalocyanine-gold nanoparticles conjugates were electrospun using polystyrene **[94]**, but no phthalocyanine-magnetite nanoparticles conjugates have been electrospun so far, therefore this is done for the first time in this work. As stated above, the use of magnetite nanoparticles allows for ease of separation when using a magnet. In the following chapter the synthesis methods and materials used for the synthesis of AMNPs, ZnOCPc-AMNPs or ZnTCPc-AMNPs conjugates and fibers are outlined in more details. The specifications of the equipments used and the experimental conditions are also discussed.

Table 1.3: Electrospun fibers functionalized with phthalocyanines and their applications

Phthalocyanine	Polymer	Application	Ref.
LuTPPc	Polystyrene	Photodegradation of 4-nitrophenol	[127]
LuTAPc ZnTAPc	Polyacrylic acid	Optical detection of NO_2 gas	[128]
CuTAPc	Poly(ethylene oxide)	for optoelectronic devices	[129]
ZnPc	Polyurethane	Antibacterial activity	[130]
CoTAPc	Cellulose fiber	Photoconversion of Reactive Red X-3B	[131]
$HOAlPc(SO_3H)_4$ $ZnPc(OC_2H_4N^+CH_3)_4$	Polyurethane	Gram-positive bacteria	[132]

TPPc= tetraphenoxy phthalocyanine, TAPc= tetraamino phthalocyanine

1.5 Summary of aims

- The aims of this thesis are summarized as follows:
- Syntheses of magnetite nanoparticles (AMNPs), zinc octacarboxy phthalocyanine (ZnOCPc) and zinc tetracarboxy phthalocyanine (ZnTCPc).
- Conjugation of AMNPs to ZnOCPc and ZnTCPc separately.
- Characterization of the ZnOCPc-AMNPs and ZnTCPc-AMNPs conjugates using ultraviolet-visible spectroscopy (UV/Vis), Fourier transform infrared spectroscopy (FTIR), powder X-ray diffractometry (PXRD), energy dispersive x-ray spectroscopy (EDS), transmission electron microscopy (TEM) and thermogravimetric analysis (TGA).
- Study the fluorescence, photophysical and photochemical properties of the conjugates.
- Optimization of elecrospinning parameters of polyamide-6 (PA-6).
- The development of polyamide-6 (PA-6) electrospun fibers containing a phthalocyanine (ZnOCPc) and phthalocyanine-magnetite nanoparticles (ZnOCPc-AMNPs).
- Characterization of the electrospun fibers using TGA, EDS and SEM.
- Investigation of the photocatalytic degradation of Orange-G by phthalocyanine and phthalocyanine-magnetite nanoparticles in solution and in fibers .

CHAPTER TWO

EXPERIMENTAL

Experimental

2.1 Materials

Anhydrous iron (III) chloride, anhydrous iron (II) sulphate, ethanol (EtOH) and toluene were purchased from SAARCHEM. Anthracene-9, 10-bis-methylmalonate (ADMA), ammonia (25%), dimethyl sulfoxide (DMSO), dimethylformamide (DMF), hydrochloric acid (32 %), sodium hydroxide pellets, sulphuric acid (98 %) and trisodium-citrate were purchased from Merck. Acetic acid (98 %), 3-aminopropyl-triethoxysilane (APTES), 1-ethyl-3-(3-dimethylaminopropyl) carbodiimide hydrochloride (EDC), formic acid (99.8 %), lipophilic Sephadex LH-20 microbeads, N-hydroxysuccinimide (NHS), Orange-G and tetraethoxysilane (TEOS) were purchased from Sigma Aldrich. Polyamide-6 Ultramid® B grades, B24, B27 and B32, with average molecular weights in grams per mole: 70,000, 80,000 and 90,000 respectively, were supplied by BASF. Phosphate-buffered solutions of pH 7.4 and 9 were prepared using appropriate amounts of Na_2HPO_4, KH_2PO_4 and chloride salts, dissolved in ultra-pure water. $AlPcS_{mix}$ (containing a mixture of sulfonated derivatives) was synthesized according to the literature **[133]** and used as a standard for triplet and singlet oxygen quantum yields.

2.2 Instrumentation

Infrared spectra were recorded on a Perkin Elmer 100 ATR FT-IR spectrometer.

Ground state electronic absorption spectra were performed on a Shimadzu UV-2550 spectrophotometer. Quartz cells with 1 cm path-length were used.

Powder X-ray analysis was performed on a Bruker D8 Discover diffractometer, equipped with a Lynx Eye detector, under Cu-Kα radiation (λ= 1.541 Å). Data were collected in the range from

2θ = 5 to 75 ^{o}, scanning at 0.010 ^{o} min^{-1} and 192 s per step. The samples were placed on a zero background silicon wafer slide. The x-ray diffraction data were processed using the Eva (evaluation curve fitting) software. Baseline correction was performed on each diffraction pattern by subtracting a spline fitted to the curved background.

Transmission electron microscopy (TEM) images were obtained using a ZEISS LIBRA® 120 transmission electron microscope.

The morphology of the electrospun nanofibers was examined using a scanning electron microscope (Jeol Quanta 200 F FE-SEM) at an accelerating voltage of 20 kV. Before SEM analysis, the sample was coated with gold using a sputter coater (Balzers Union SKD 030). The average fiber diameter and their standard deviations were based on 50 measurements, using Cell ^{D} software from Olympus.

Energy dispersive spectroscopy (EDS) was done on an INCA PENTA FET coupled to the VAGA TESCAM using 20 kV accelerating voltage.

A Perkin Elmer TGA 7 Thermogravimetric analyser was used to study the thermal properties of the compounds under an inert N_2 atmosphere (at 20 mL min^{-1}) and heating at a rate of 10 ^{o} C min^{-1}.

Fluorescence excitation and emission spectra were recorded on a Varian Eclipse fluorescence spectrofluorometer.

Fluorescence lifetimes were measured using time correlated single photon counting setup (TCSPC) (PicoQuant FluoTime 200), as shown in Figure 2.1. The excitation source was a diode LDH-P-670 with PDL 800-B, 670 nm, 20 MHz repetition rate Picoquant GmbH. Fluorescence was detected under the magic angle with a peltier cooled photomultiplier tube (PMT) (PMA-C 192-N-M, Picoquant) and integrated electronics (PicoHarp 300E, Picoquant GmbH). A

monochromator with a spectral width 4 nm was used to select the required emission wavelength. The response function of the system, which was measured with a scattering Ludox solution (DuPont), had a full width at half-maximum (FWHM) of 300 ps. The fluorescence lifetimes were obtained by deconvolution of the decay curves using the FluoFit Software program (PicoQuant GmbH, Germany).

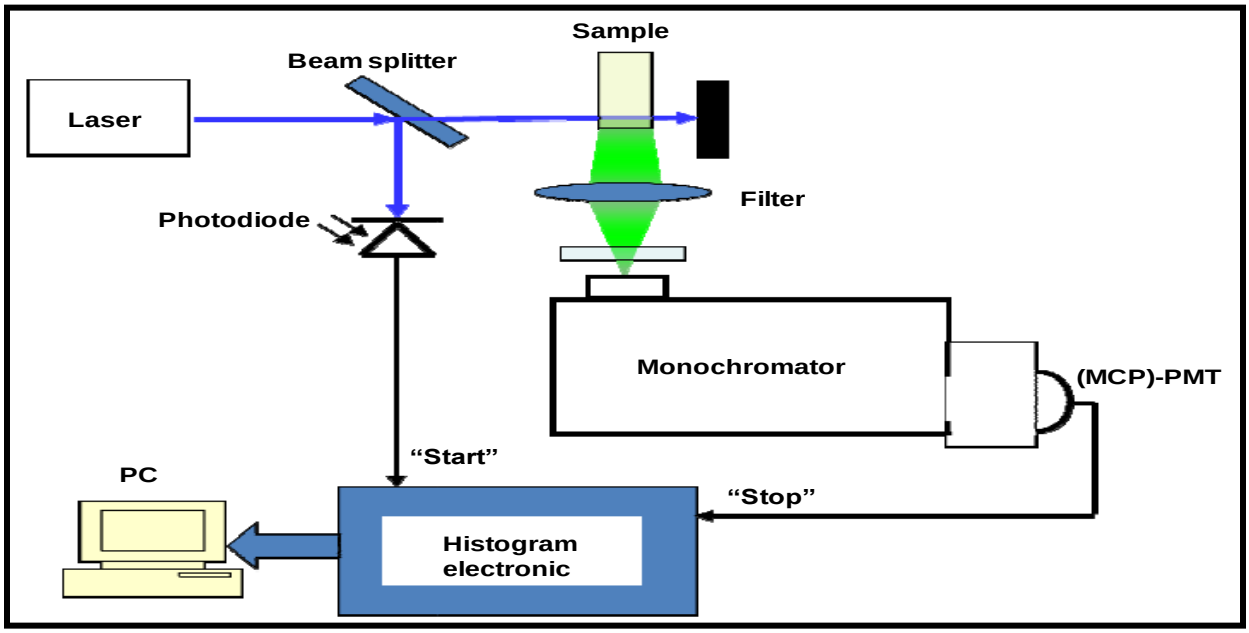

Figure 2.1: Schematic diagram of time-correlated single photon counting (TCSPC) setup. (MCP)-PMT = Monochromator photomultiplier tube, PC = Personal computer.

Laser flash photolysis system (Figure 2.2) was used for the determination of triplet decay kinetics. The excitation pulses were produced by a tunable laser system consisting of an Nd: YAG laser (355 nm, 135 mJ/4-6 ns) pumping an optical parametric oscillator (OPO, 30 mJ/3-5 ns) with a wavelength range of 420 - 2300 nm (NT-342B, Ekspla). The analyzing beam source was from a Thermo Oriel 66902 xenon arc lamp, and a Kratos Lis Projekte MLIS-X3 photomultiplier tube was used as the detector. Signals were recorded with a dual channel, 300

MHz digital real time oscilloscope (Tektronix TDS 3032C). The triplet lifetimes were determined by the exponential fitting of the kinetic curves using OriginPro 8 software.

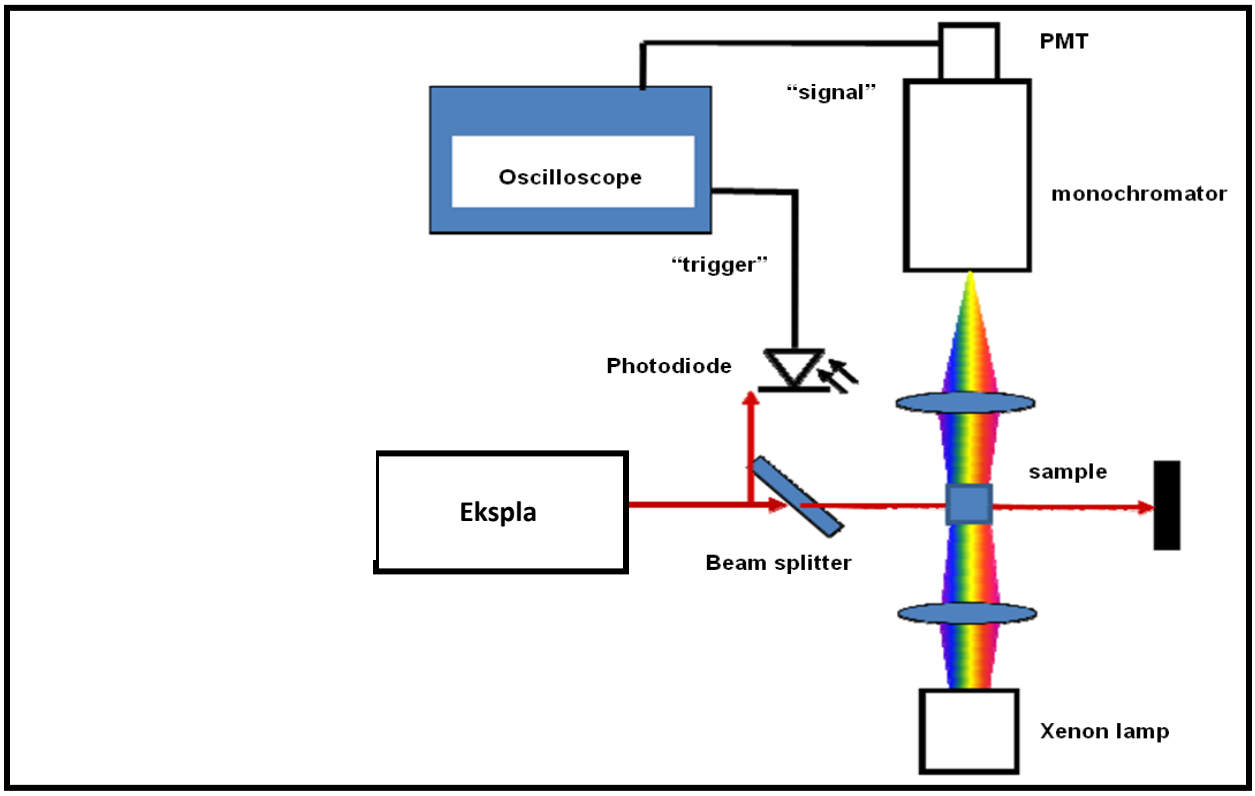

Figure 2.2: Schematic diagram for a laser flash photolysis setup. PMT= Photo Multiplier Tube

The time resolved singlet oxygen phosphorescence at 1270 nm (Figure 2.3) was used to determine the singlet oxygen quantum yields in aqueous solution. The dynamic phosphorescence decay of singlet oxygen ($^1O_2$) species was demonstrated using its phosphorescence at 1270 nm. For these studies, an ultra-sensitive germanium detector (Edinburgh Instruments, EI-P) combined with a 1000 nm long pass filter (Omega, RD 1000 CP) and a 1270 nm band-pass filter (Omega, C1275, BP50) was used to detect $^1O_2$ phosphorescence under excitation using a Quanta-Ray Nd:YAG laser which provided a 400 mJ, 9 ns pulses of laser light at 10 Hz pumping a Lambda-Physik FL3002 dye laser (Pyridin 1 dye in methanol), with a pulse period of 7 ns and repetition

rate of 10 Hz. The near-infrared phosphorescence of the samples were focused onto the germanium detector using a lens (Edmund, NT 48-157) with the detection direction perpendicular to the excitation laser beam. The detected signals were averaged with a digital oscilloscope (Tektronics, TDS 360) to show the dynamic decay of $^1O_2$. The data obtained was analysed using ORIGIN Pro 8 software.

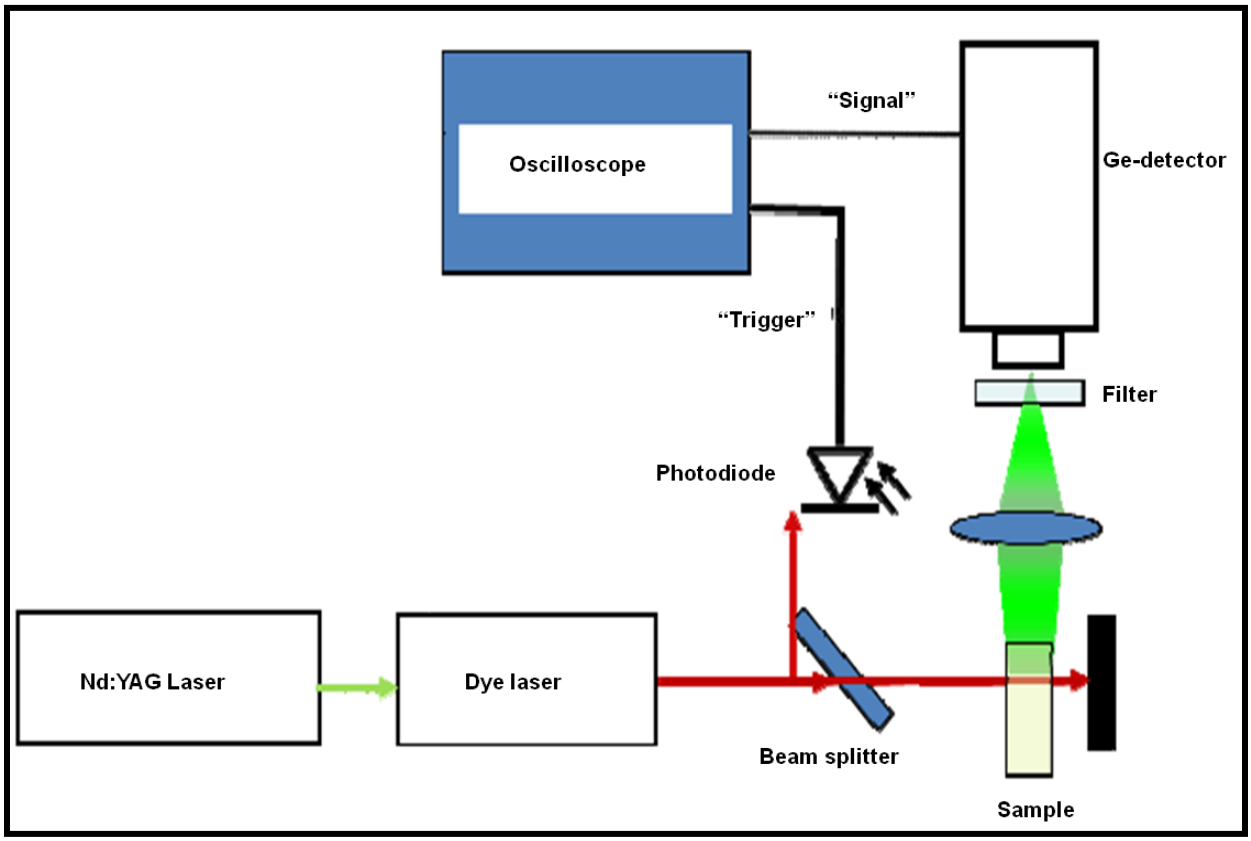

Figure 2.3: Schematic diagram for the singlet oxygen detection setup using its phosphorescence.

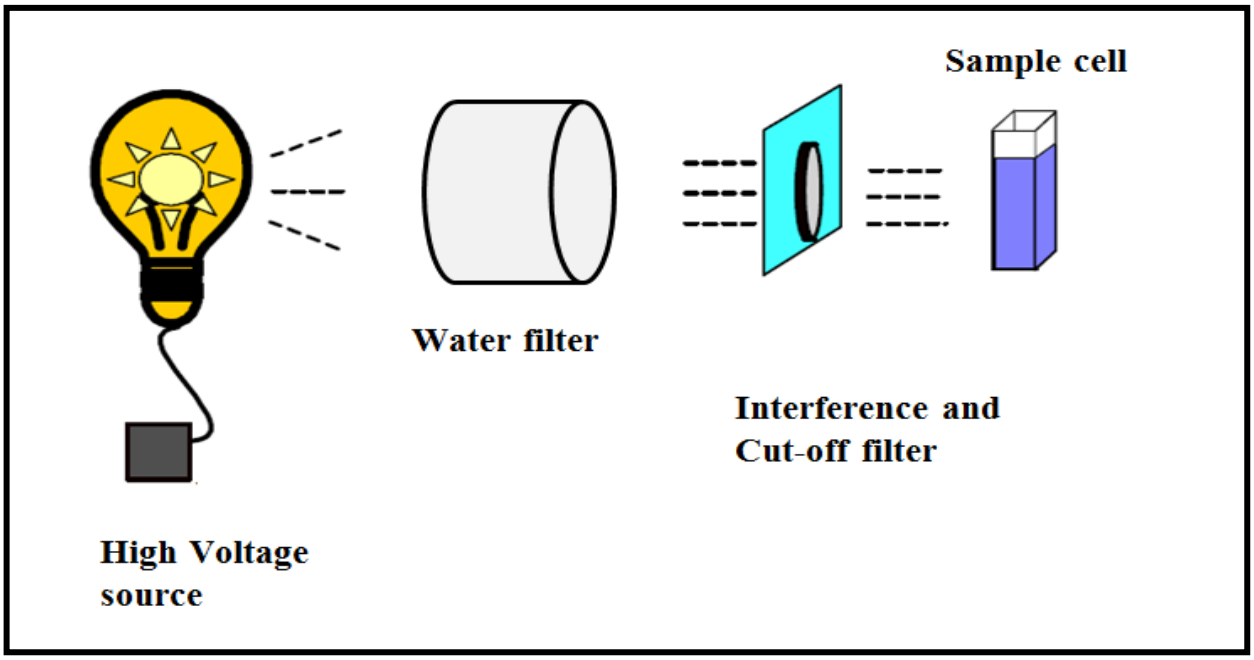

Figure 2.4: Schematic diagram of a photochemical setup.

Determination of the singlet oxygen quantum yield and the photodegradation of Orange-G (OG) were carried out using a Halogen lamp (300W), 600 nm glass (Schott) and water filters, to filter off ultra-violet and far infrared radiation respectively as shown in Figure 2.4. An interference filter (Intor, 670 nm with bandwidth of 40 nm) was placed in the light path just before the reaction vessel (which was a glass vial). The intensity of the light reaching the reaction vessel was measured with a power meter (POWER MAX 5100 Molelectron Detector Inc).

For elecrospinning, polymer solution viscosity and conductivity were measured using a rotating Brookfield Viscometer LVDV-II and a CDM-210 conductivity meter (Radiometer Analytical). The electrospinning set-up consisted of an infusion pump KD Scientific Syringe Pump Series 100 used to pump out a solution held in a 20 ml plastic syringe fitted with a needle (dimensions: 1.024 mm × 15.24 cm). A high-voltage source (Glassman High Voltage Series EH) was used to generate an electric field between the needle tip and a grounded collector.

2.3 Syntheses

The syntheses of ZnOCPc **[134]** and ZnTCPc **[135]** have been reported before.

2.3.1 Synthesis of AMNPs

2.3.1.1 Citrate stabilized magnetite (Fe_3O_4) nanoparticles (CMNPs), Scheme 3.1, Step 1 (p 45)

The magnetite nanoparticles were obtained by the co-precipitation of Fe^{3+} and Fe^{2+} as in literature **[136]** with slight modification as follows: $FeCl_3$ (0.65 g, 4.0 mmol) and $FeSO_4$ (0.32 g, 2.0 mmol) were introduced into a three necked flask fitted with a thermometer and an inert gas inlet. Millipore water (42.5 ml) was added under a N_2 atmosphere, while the third neck of the flask was closed with a rubber septum. Ammonia solution (5 ml, 25 %) was added to the reaction mixture using a syringe with continuous stirring, also under nitrogen. After the addition of the NH_3 solution, the mixture turned black, with stirring continued for a further 1 hr. Trisodium citrate (100 ml, 0.3 M) was then added and the mixture was stirred for a further 30 min at 90 ^{0}C. The synthesized particles were collected using a magnet and washed with Millipore water. The CMNPs were again dispersed in Millipore water for further functionalization with silica in the next section. Yield: 0.61g, 63 % `

Silica coated magnetite nanoparticles (SMNPs), Scheme 3.1, Step 2 (p 45)

To the CMNPs dispersed in Millipore water, CH_3OH (160 ml) and 40 ml of H_2O were added. To this reaction mixture, 3 ml of NH_3 solution and 2 ml of tetraethylorthosilicate (TEOS) were added sequentially and the mixture allowed to stir for 24 hr followed by washing with two parts of 30 ml Millipore water as reported in literature **[137]**. Yield: 0.38 g, 62 %

2.3.1.3 Amino functionalized magnetite nanoparticles (AMNPs), Scheme 3.1, Step 3 (p 45)

A sample of SMNPs (10 mg) was washed with anhydrous ethanol followed by toluene (3x) **[137]**. The SMNPs were then added to 12 ml of DMF and 8 ml of toluene and the mixture stirred. APTES (1000 µL) was then added drop-wise using a syringe needle. The mixture was stirred for 24 hr at room temperature under Ar gas flow. The as-prepared amino functionalized MNPs (AMNPs) were washed four times with toluene and collected with the aid of a magnet upon decantation of the supernatant. Yield: 6.6 mg, 66 %

2.3.1.4 ZnOCPc-AMNPs conjugate, Scheme 3.2 (p 47)

The literature method used for linking silica functionalized quantum dots to a metallated phthalocyanine (MPc) was employed **[138]**. The carboxyl groups of ZnOCPc or ZnTCPc were activated by dissolving ZnOCPc (15 mg, 0.75 mmol) or ZnTCPc (15 mg, 0.61 mmol), in 5 ml of PBS, pH 7.4. EDC (0.23 g, 1.2 mmol) and NHS (0.12 g, 1.0 mmol) were added and the solution stirred for 3 hr. The amino functionalized MNPs (5 mg) were suspended in 5 ml PBS at pH 7.4, sonicated, and subsequently added to the activated ZnOCPc or ZnTCPc. The mixture was stirred for 12 hr at room temperature with a N_2 gas flow. The product was precipitated by addition of ethanol, and washed with ethanol. Size exclusion chromatography (using an aqueous solution at pH 9 as the eluting solvent) was used to separate unreacted Pcs from the conjugate. A magnet was also used to separate the conjugate from unreacted Pcs. The linked conjugate is represented as ZnOCPc-AMNPs (linked) or ZnTCPc-AMNPs (linked). Similar experiments were also performed where ZnOCPc or ZnTCPc was simply mixed with AMNPs without coupling agents (EDC and NHS). Yield: 12 mg, 60 %

2.4 Photophysichemical methods

2.4.1 Fluorescence quantum yields (Φ_F).

Fluorescence quantum yields (Φ_F) of the MPcs and MPc-AMNPs conjugates were determined using a comparative method (Eq. 1.3) in pH 9 buffer or EtOH: NaOH (1:1). Unsubstituted ZnPc (Φ_F = 0.20) **[139]** in DMSO was employed as a standard. Both the samples and the standard were excited at the same wavelength. The absorbances of the solutions at the excitation wavelength were about 0.05 to avoid any inner filter effects.

2.4.2 Triplet quantum yields (Φ_T) and lifetimes (τ_T)

The decay kinetics of the triplet absorption of the MPcs and MPc-AMNPs conjugates were recorded using laser flash photolysis setup, Figure. 2.2. The absorbance of sample solutions and that of the standard were adjusted to be nearly 1.5 at their Q-band maximum. All samples were introduced into a 1 cm quartz cell and then bubbled with argon for 10 min to remove dissolved oxygen before taking readings. The triplet quantum yields of the phthalocyanines alone or in the presence of magnetite nanoparticles were determined using Eq. 1.4. Mixed-sulfonated aluminium phthalocyanine (AlPcSmix) was employed as a standard {AlPcSmix in aqueous medium (Φ_T^{std} = 0.44 **[71]**)}. Triplet lifetimes were determined from the kinetic data obtained, using ORIGIN Pro 8 software to fit the kinetics decay curves.

2.4.3 Singlet oxygen quantum yield (Φ_Δ)

The determination of Φ_Δ was achieved by employing an optical and chemical method. The optical method involves the observation of the fluorescence kinetic decay of the singlet oxygen generated at 1270 nm in air using equipment shown in Figure 2.3. The singlet oxygen quantum yield (Φ_Δ) determinations for the MPcs and MPc-AMNPs in aqueous solution and in fibers were

carried out in unbuffered aqueous media. For MPc or MPc-AMNPs in aqueous solution, sodium azide (NaN_3) was used as singlet oxygen quencher. The dynamic course of the singlet oxygen concentrations were clearly recorded following Eq.1.7. The Φ_Δ values were then determined using Eq. 1.8, and employing AlPcSmix in aqueous solution ($\Phi_\Delta^{Std} = 0.42$) **[71]**) as a standard.

For singlet oxygen quantum yield (Φ_Δ) determination in fibers, ADMA was used a singlet oxygen quencher and its degradation was monitored at 380 nm, Figure. 2.4. In each case 15 mg of the modified fibers was suspended in an aqueous solution of ADMA and irradiated using the photolysis set-up described above. The quantum yields (Φ_{ADMA}) were calculated using Eq. 1.11 also using the molar extinction coefficient of ADMA in water, log (ε) = 4.1 **[140]**. The intensity of the light reaching the reaction vessel was measured with a power meter (POWER MAX 5100 Molelectron Detector Inc) and found to be 1.3×10^{19} photons cm^{-2} s^{-1}.

2.4.4 Photodegradation of Orange-G

Photocatalytic reactions were carried out in a batch reactor (glass vial). The irradiation experiments were carried out using the photolysis setup described above for singlet oxygen determination, Figure 2.4. The intensity of the light reaching the reaction vessel was measured with a power meter (POWER MAX 5100 Molelectron Detector Inc) and found to be 3.2×10^{19} photons cm^{-2} s^{-1}.

2.5. Electrospinning methods

Electrospinning of polyamide-6 (PA-6) was carried out in air at room temperature with the relative humidity (RH) between 48-52 % at 25 ^{o}C. PA-6 (i.e., B24, B27 and B32) pellets were dissolved in formic acid/acetic acid (50/50 and 75/25 vol. %) solvent mixtures to produce a uniform polymer solution with concentrations in the range 10 to 16 wt. %, Table 2.1. The solutions were magnetically stirred at room temperature for 3 hr, followed by the measurement of their conductivity and viscosity. A high voltage in the range 9-30 kV was applied to the polymer solution, which is held in a plastic syringe equipped with a needle. The flow rate ranged between 0.2 and 1ml/h. The distance between the needle tip and the grounded collector was 6 cm. Polymers containing different concentrations of Pcs were prepared as follows: ZnOCPc (2 mg, 0.1 mmol), (10 mg, 0.5 mmol) or (20 mg, 1.0 mmol) were dissolved in PA-6 (B32 14 wt. %) polymer solution of formic acid/ acetic acid (50/50 and 75/25 vol. %) followed by electrospinning. The fabrication of ZnOCPc-AMNPs hybrid nanofibers was carried out by adding 30 mg of ZnOCPc-AMNPs conjugate into PA-6 solution, followed by electrospinning. The spectral characterization, morphology and the thermal stability of the as synthesized AMNPs, ZnOCPc-AMNPs and ZnTCPc-AMNPs are discussed in the following chapter. The photophysical and photochemical parameters of these two complexes i.e. ZnOCPc-AMNPs and ZnTCPc-AMNPs are also compared.

Table 2.1: Operating parameters used for electrospinning of PA-6 nanofibers

Parameter	
Polymer molecular weight	70 000, 80 000, 90 000
Polymer concentration	10-16 wt.%
Applied voltage	9-30 kV
Flow rate	0.2- 1ml/h
Humidity	48-52 % RH
Solvent system	FA/AA
TCD (tip-to-collector distance)	6 cm

CHAPTER THREE

Characterization of the conjugates

3.1 Synthesis of AMNPs and Pc-AMNPs conjugates

The co-precipitation of Fe^{2+}/ Fe^{3+} was carried out in aqueous medium under inert conditions since MNPs are subject to oxidation in air. To allow monodispersity and stability, the magnetite nanoparticles (MNPs) were stabilized with trisodium citrate to yield CMNPs, Scheme 3.1, step 1. The nanoparticles obtained were black and exhibited strong magnetic response. The CMNPs were coated with silica to prevent corrosion of MNPs and to allow further functional group attachment, Scheme 3.1, step 2. The silica coated MNPs (SMNPs) were functionalized with 3-aminopropyltriethoxy silane (APTES) to yield amino functionalized MNPs (AMNPs) (Scheme 3.1, step 3). This facilitates linking to carboxylic phthalocyanines through an amide bond.

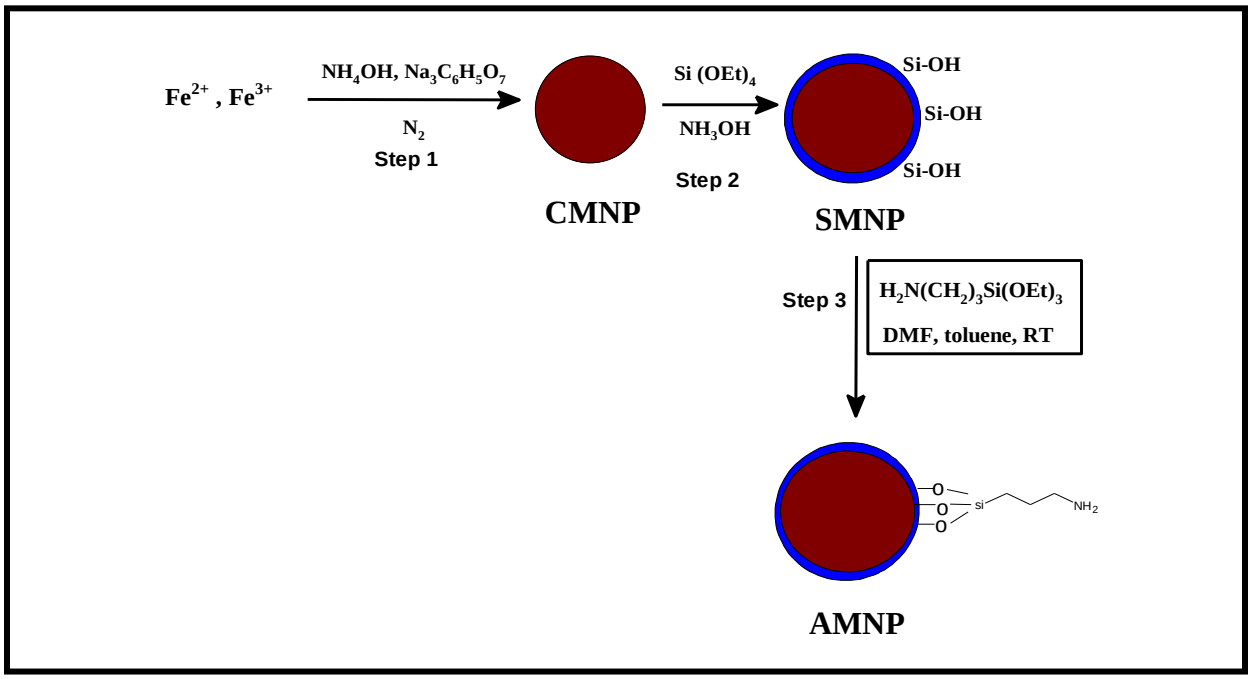

Scheme 3.1: Synthesis of amino functionalized magnetite nanoparticles (AMNPs). CMNP= citrate stabilized magnetite nanoparticles; SMNP= silica coated magnetite nanoparticles

The ZnOCPc and ZnTCPc were synthesized according to the method reported in literature **[134, 135].** The carboxylic acid groups on these molecules allow covalent linkage to the amino functionalized MNPs through an amide bond. The nanocomposites of ZnOCPc-AMNPs and ZnTCPc-AMNPs were formed by a covalent linkage of ZnOCPc or ZnTCPc with the amino functionalized magnetite nanoparticles (AMNPs). 1-Ethyl-3-(3-methylaminopropyl) carbodiimide (EDC) and N-hydroxy succinimide (NHS) were used to activate the carboxylic acid groups on the ZnOCPc or ZnTCPc before linking to the amino groups of the AMNPs, as shown for ZnOCPc in Scheme 3.2**.** Studies have shown that with a mixture of EDC and NHS, about 60% of the carboxylic acid groups are NHS-activated, 30% are EDC activated, leaving only 10% not activated **[141]**. Therefore it is possible that more than one ZnOCPc or ZnTCPc can be linked to the MNPs.

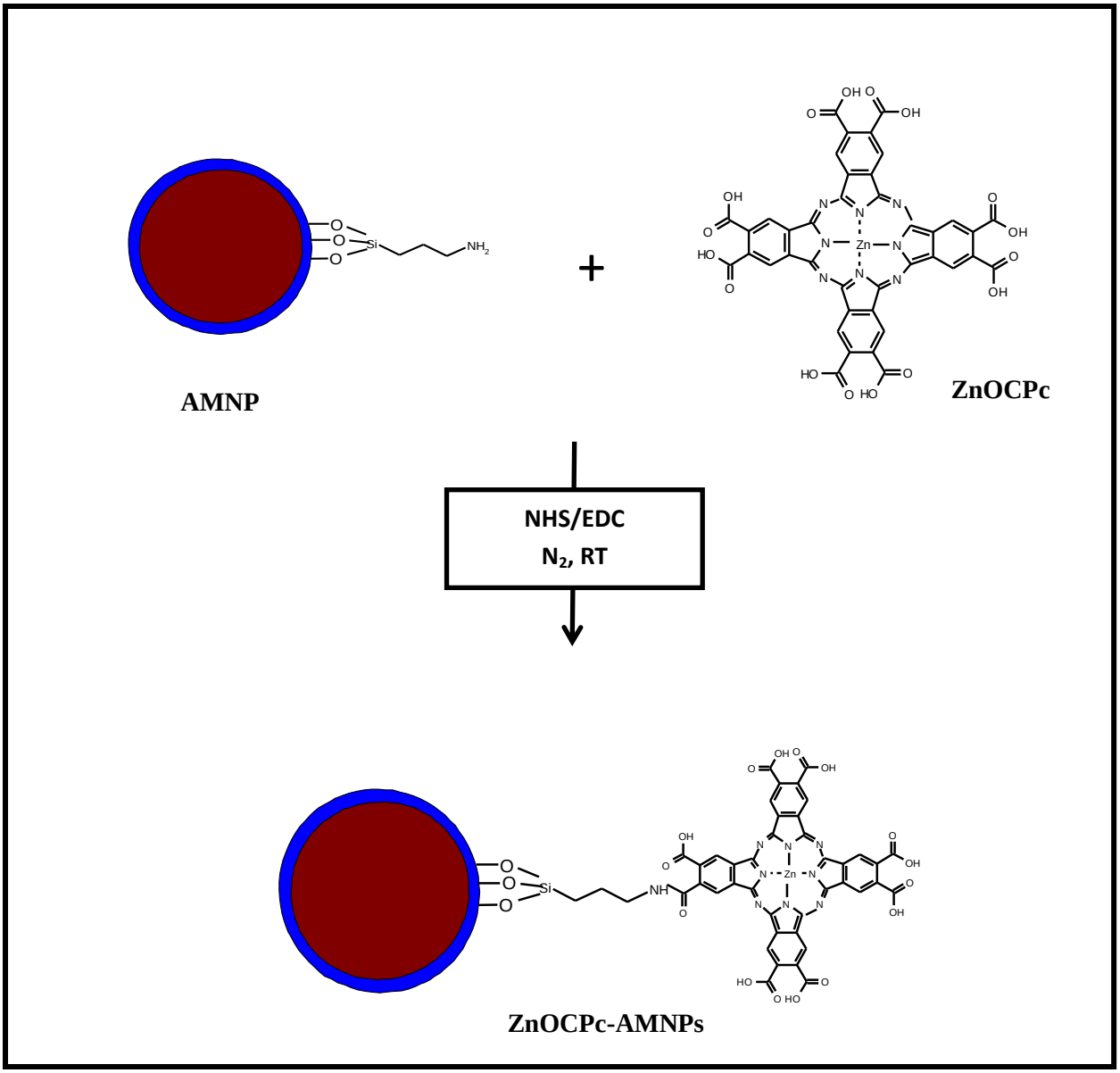

Scheme 3.2: Covalent linking of AMNPs to ZnOCPc. NHS = N-hydroxy succinimide; EDC= 1-Ethyl-3-(3-methylaminopropyl) carbodiimide

Scheme 3.3 shows the use of EDC and NHS in the formation of the amide bond. The NHS is used to prepare amine-reactive esters of carboxylate groups for crosslinking. The carboxylates (-COOH) of the Pcs are reacted with NHS in the presence of a carbodiimide (EDC), resulting in a semi-stable NHS ester, which may then be reacted with primary amines ($-NH_2$) to form amide crosslinks (Scheme 3.3). The activation reaction with EDC and NHS is most efficient at pH 4.5-7.4; hence these reactions were performed in buffer solution of pH 7.4.

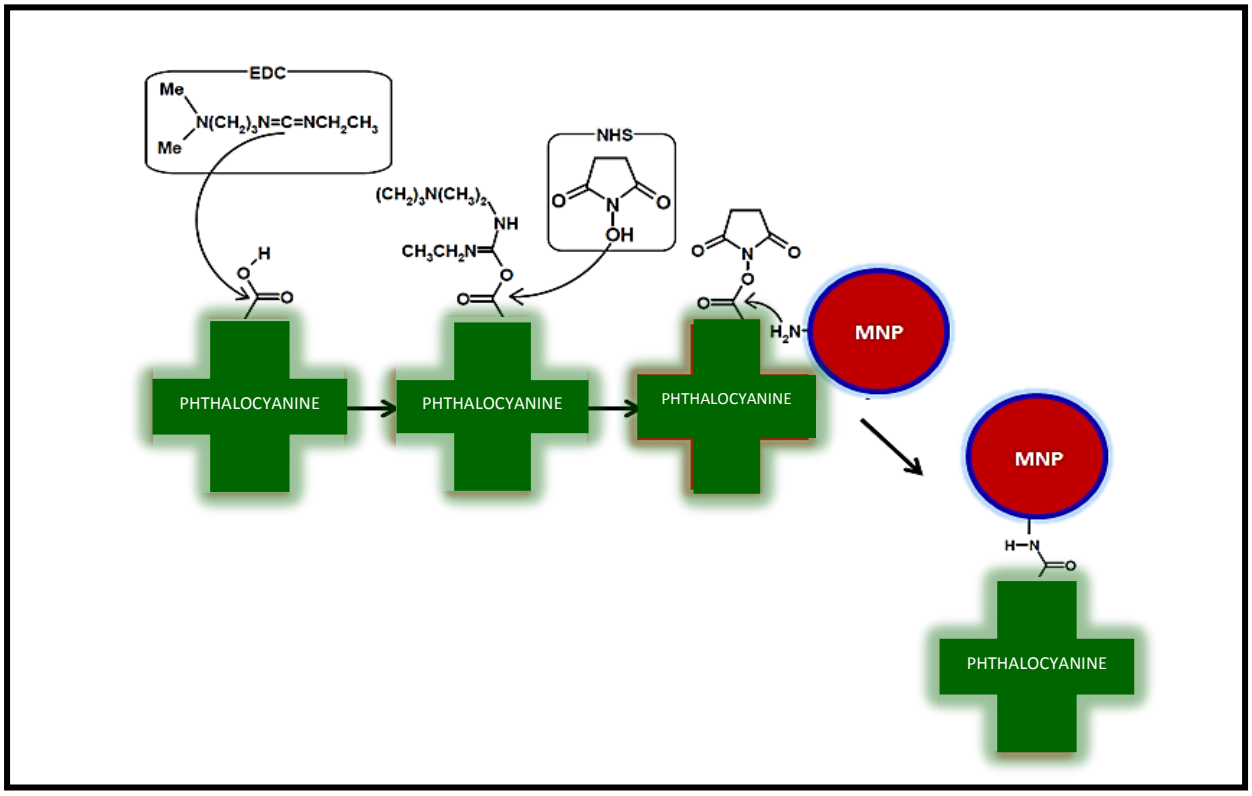

Scheme 3.3: Schematic representation showing the activation of carboxylic acid group of the phthalocyanine and the immobilization of AMNPs on activated carboxy-phthalocyanine forming an amide bond.

3.2 Characterization of ZnOCPc-AMNPs and ZnTCPc-AMNPs conjugates

3.2.1 FTIR spectra (p 50)

The covalent link between ZnOCPc or ZnTCPc and AMNPs was confirmed by FTIR spectroscopy as shown in Figure 3.1. The characteristic peaks of the primary amino ($-NH_2$) group of the AMNPs are observed at 1568 cm^{-1} and 1484 cm^{-1}, Figure 3.1 (i) (A) and B. The intense peak at 1034 cm^{-1} is assigned to Si-O-Si and Fe-O-Si bonding stretch, as reported in literature [**142**]. The ZnOCPc shows the C=O vibration at 1709 cm^{-1} and broadened peak in the range 3100 cm^{-1} to 3600 cm^{-1} corresponding to the O-H of the carboxyl group, Figure 3.1 (ii) (A). The ZnOCPc-AMNPs (mixed) spectrum in Figure 3.1 (iii) (A), showed the C=O peak (at 1710 cm^{-1}) and the O-H of the carboxyl group of the ZnOCPc, showing no covalent bonding between the MNPs and ZnOCPc. With the ZnOCPc-AMNPs (linked) conjugate, the peaks attributed to the -COOH functional group disappeared. While the peaks assigned to the amide (-NHCO-) group appeared i.e. C=O stretch (1631 cm^{-1}), -NH- bend (1535 cm^{-1}) and the -NH- stretch at 3283 cm^{-1}, Figure 3.1(iv) (A). Similar IR spectral changes were observed for ZnTCPc, ZnTCPc-AMNPs (mixed) and ZnTCPc-AMNPs (linked), Figure 3.1 (B).

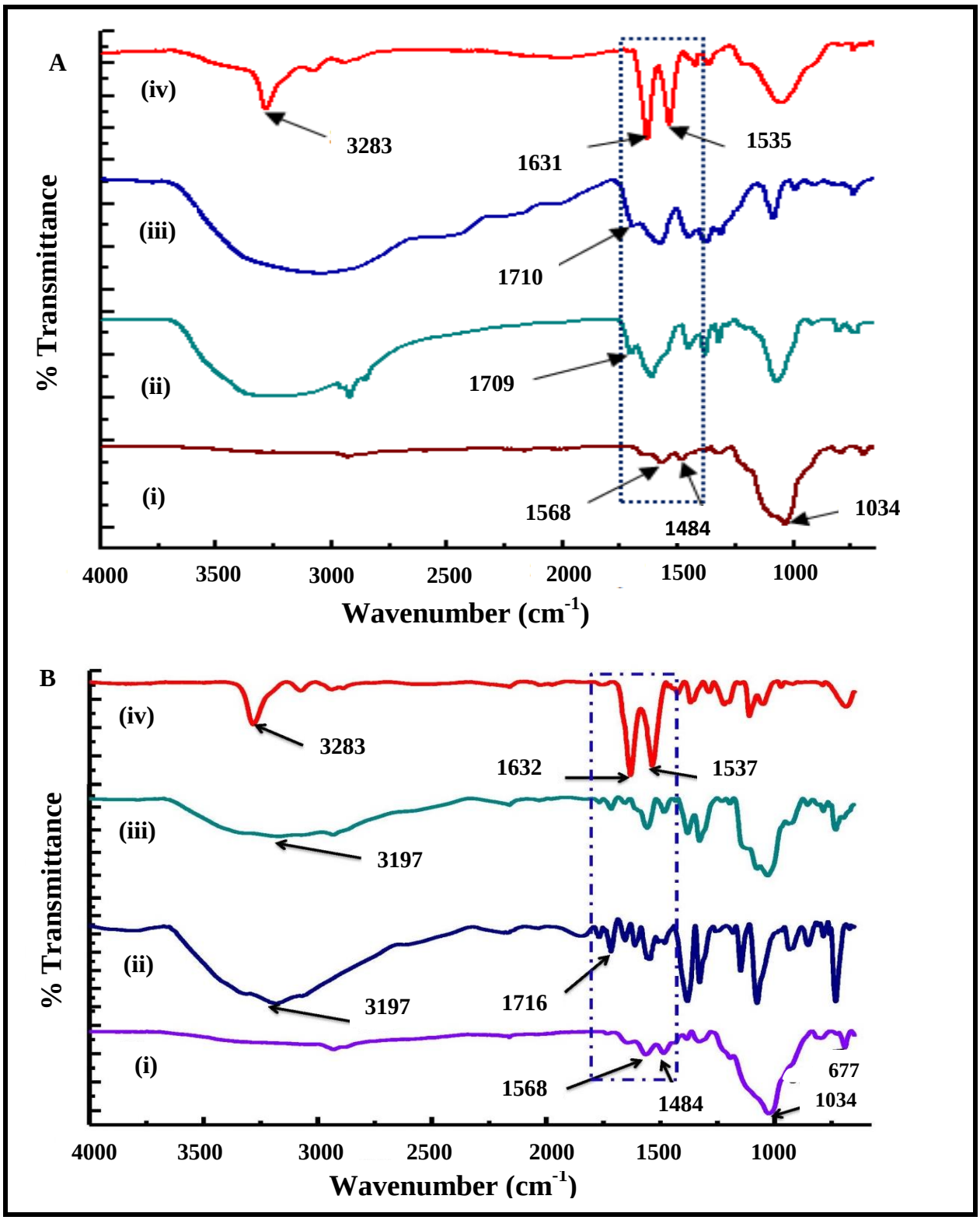

Figure 3.1: FT-IR spectra of (i) AMNPs (ii) ZnOCPc (iii) ZnOCPc-AMNPs (mixed) and (iv) ZnOCPc-AMNPs (linked) (A). (i) AMNPs, (ii) ZnTCPc, (iii) ZnTCPc-AMNPs (mixed) and (iv) ZnTCPc-AMNPs (linked) (B). Highlighted = amide bond region.

3.2.2 UV/ Vis absorption and fluorescence spectra

Selected data from the absorption and fluorescence spectra of the MPcs and their conjugates are presented in Table 3.1. A mixture of solvents, EtOH: NaOH (1:1) was used for ZnTCPc in order to suppress its aggregation. ZnOCPc is partially soluble in water and highly soluble in alkaline pH, hence pH 9 solution was used.

Table 3. 1: Wavelength of strongest absorption (abs), emission (emm) and excitation (exc) of MPcs and their conjugates in the solvent media, EtOH: NaOH (1:1) and also in pH 9 buffer.

Complex	Solvent	λ_{abs} (nm)	λ_{emm} (nm)	λ_{exc} (nm)
ZnOCPc	pH 9 buffer	691	705	691
ZnOCPc-AMNPs (mixed)	pH 9 buffer	691	706	698
ZnOCPc-AMNPs (linked)	pH 9 buffer	688	701	694
ZnTCPc	EtOH: NaOH (1:1)	673	708	706
ZnTCPc-AMNPs (mixed)	EtOH: NaOH (1:1)	673	708	704
ZnTCPc-AMNPs (linked)	EtOH: NaOH (1:1)	673	694	692

3.2.2.1 ZnOCPc-AMNPs conjugate

The amino functionalized MNPs showed a broad absorption peak at 385 nm, Figure 3.2. The ground state electronic absorption spectra of ZnOCPc showed a monomeric behavior as evidenced by a single narrow Q-band, which is reported before [**143**]. The Q band of the ZnOCPc in pH 9 buffer solution is observed at 691 nm, Figure 3.2 (Table 3.1). The absorption spectrum of ZnOCPc-AMNPs is broad and shows the presence of both the ZnOCPc and

AMNPs. There was no change in the Q band maxima following mixing of ZnOCPc with AMNPs (without a chemical bond) as reported in literature for other MPc complexes mixed with MNPs [**144**]. The ZnOCPc-AMNPs (linked) showed a slight blue shift of the Q band compared to ZnOCPc alone due to covalent linking.

For ZnOCPc the excitation was similar to absorption spectra and both were mirror images of the emission spectra, Figure 3.3A. For the ZnOCPc-AMNPs (mixed), the excitation and absorption spectra were observed at 698 nm and 691 nm, respectively, Table 3.1 (Figure 3.3B), suggesting red shifting by 7 nm upon excitation. For ZnOCPc-AMNPs (linked) the excitation was red shifted from absorption by 6 nm, Table 3.1 (Figure 3.3C). However, the mirror image rule still holds for both mixed and linked. The red shifting for linked and mixed ZnOCPc-AMNPs could be due to the antiparallel orientation of dipolar moments of both ZnOCPc and MNPs upon excitation; such kind of behavior is reported in literature **[145]**.

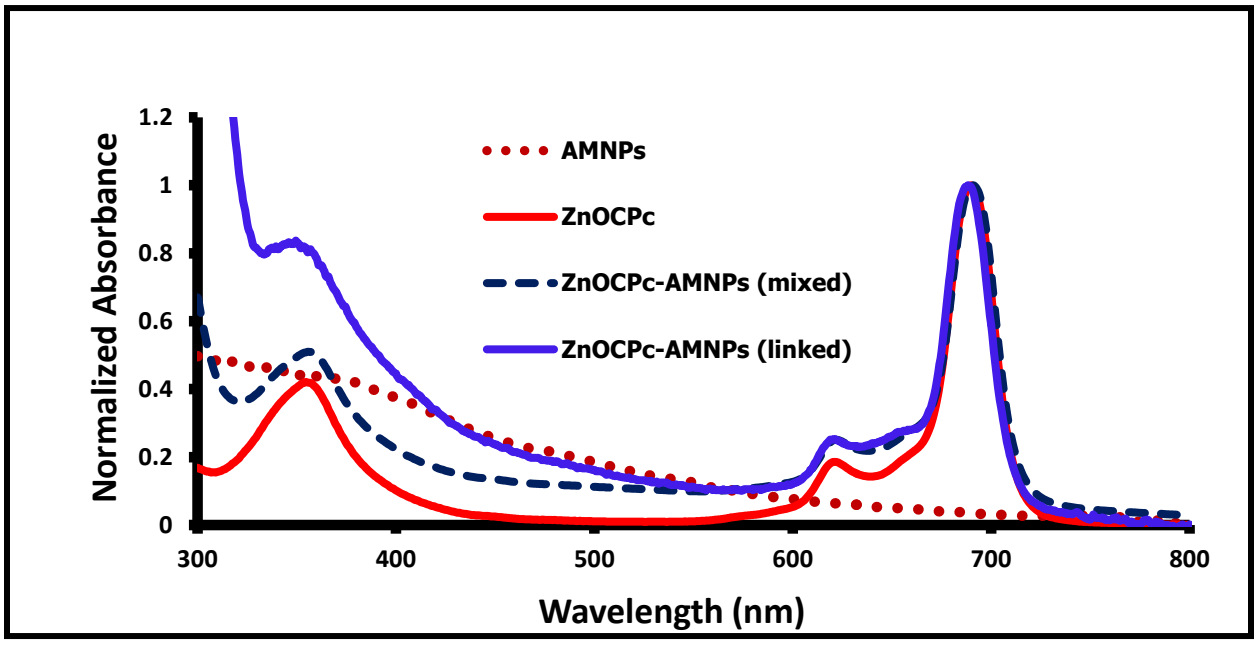

Figure 3.2: Ground state absorption spectra of AMNPs, ZnOCPc, ZnOCPc-AMNPs (mixed) and ZnOCPc-AMNPs (linked) using pH 9 buffer. Concentration ~ 2.5×10^{-6} M.

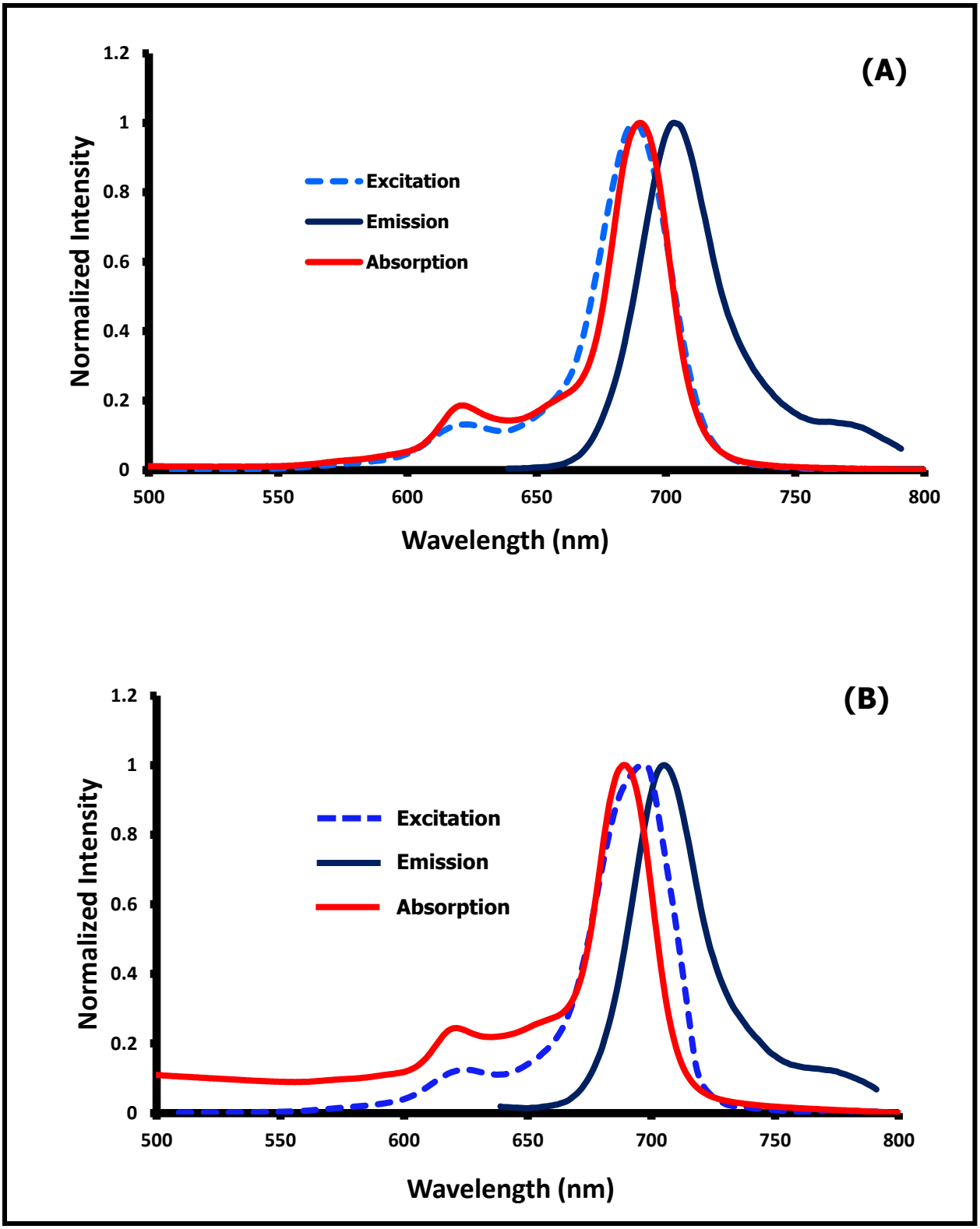
(A)
Normalized Intensity
1.2
1
0.8
0.6
0.4
0.2
0
Excitation
Emission
Absorption
500
550
600
650
700
750
800
Wavelength (nm)
(B)
Normalized Intensity
1.2
1
0.8
0.6
0.4
0.2
0
Excitation
Emission
Absorption
500
550
600
650
700
750
800
Wavelength (nm)

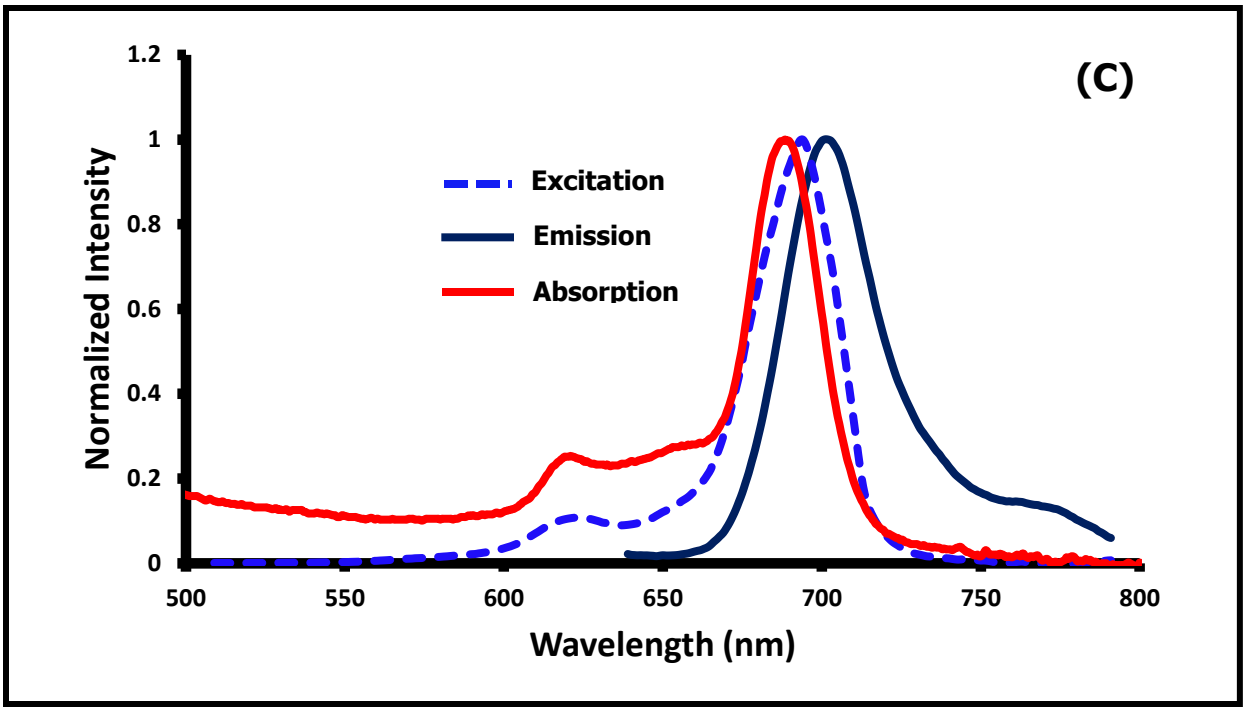

Figure 3.3: Ground state absorption, fluorescence emission and excitation spectra of (A) ZnOCPc, (B) ZnOCPc-AMNPs (mixed) and (C) ZnOCPc-AMNPs (linked) in pH 9 buffer solution, λ exc = 620 nm.

3.2.2.2 ZnTCPc-AMNPs conjugate

The ZnTCPc is known to be aggregated in aqueous media [**146**], hence it shows splitting of the Q-band, Figure 3.4 (i). The low energy peak is due to the monomer, while the high energy band is due to the aggregate. Aggregation persisted when ZnTCPc and AMNPs are mixed, Figure 3.4 (ii), but upon linking, aggregation is reduced, Figure 3.4 (iii). The aggregation of ZnTCPc was also reduced by using a solvent mixture of EtOH and NaOH (1:1), Figure 3.5A. It is well known that organic solvents break up aggregation in phthalocyanines **[68]**. For ZnTCPc, ZnTCPc-AMNPs (mixed) and ZnTCPc-AMNPs (linked), the Q-band of the excitation spectra were red shifted by 33 nm, 31 nm and 19 nm (the latter in Figure 3.5 B), respectively as compared to the

absorption spectra, Table 3.1. This could be related to the fact that ZnTCPc consists of a mixture of isomers, with some being more fluorescent.

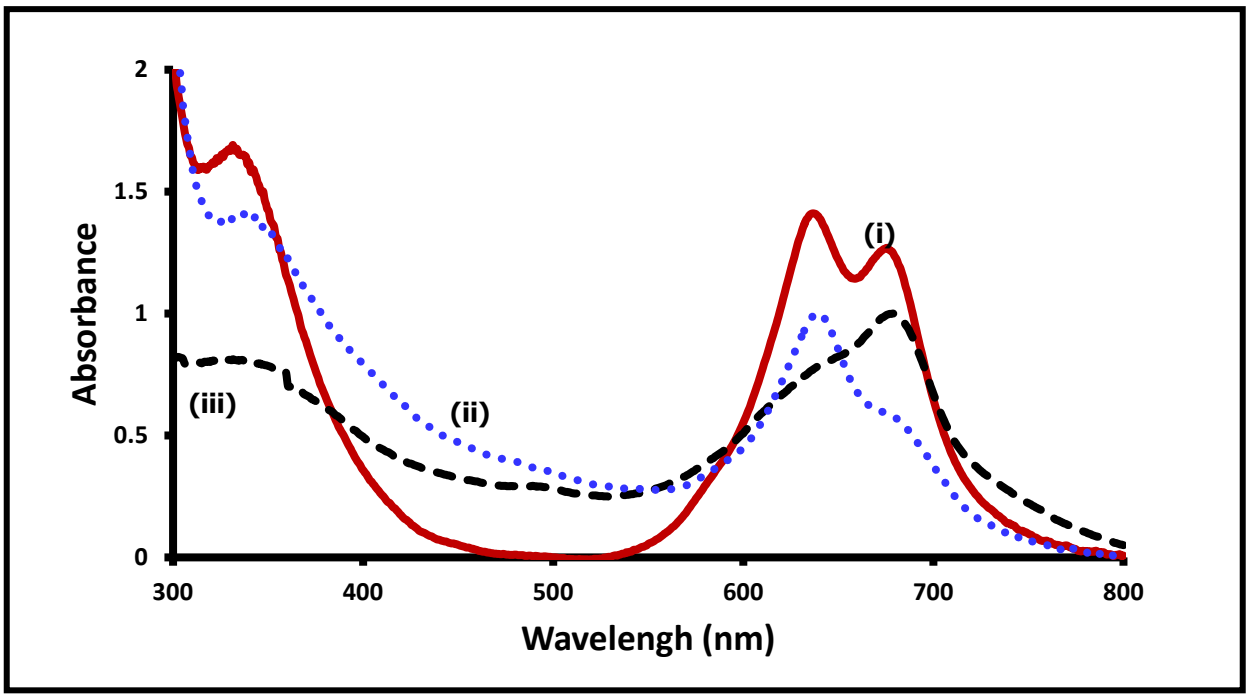

Figure 3.4: Ground state absorption spectra of ZnTCPc (i), ZnTCPc-AMNPs (mixed) (ii) and ZnTCPc-AMNPs (linked) (iii) in pH 9. Concentration ~10^{-6} M.

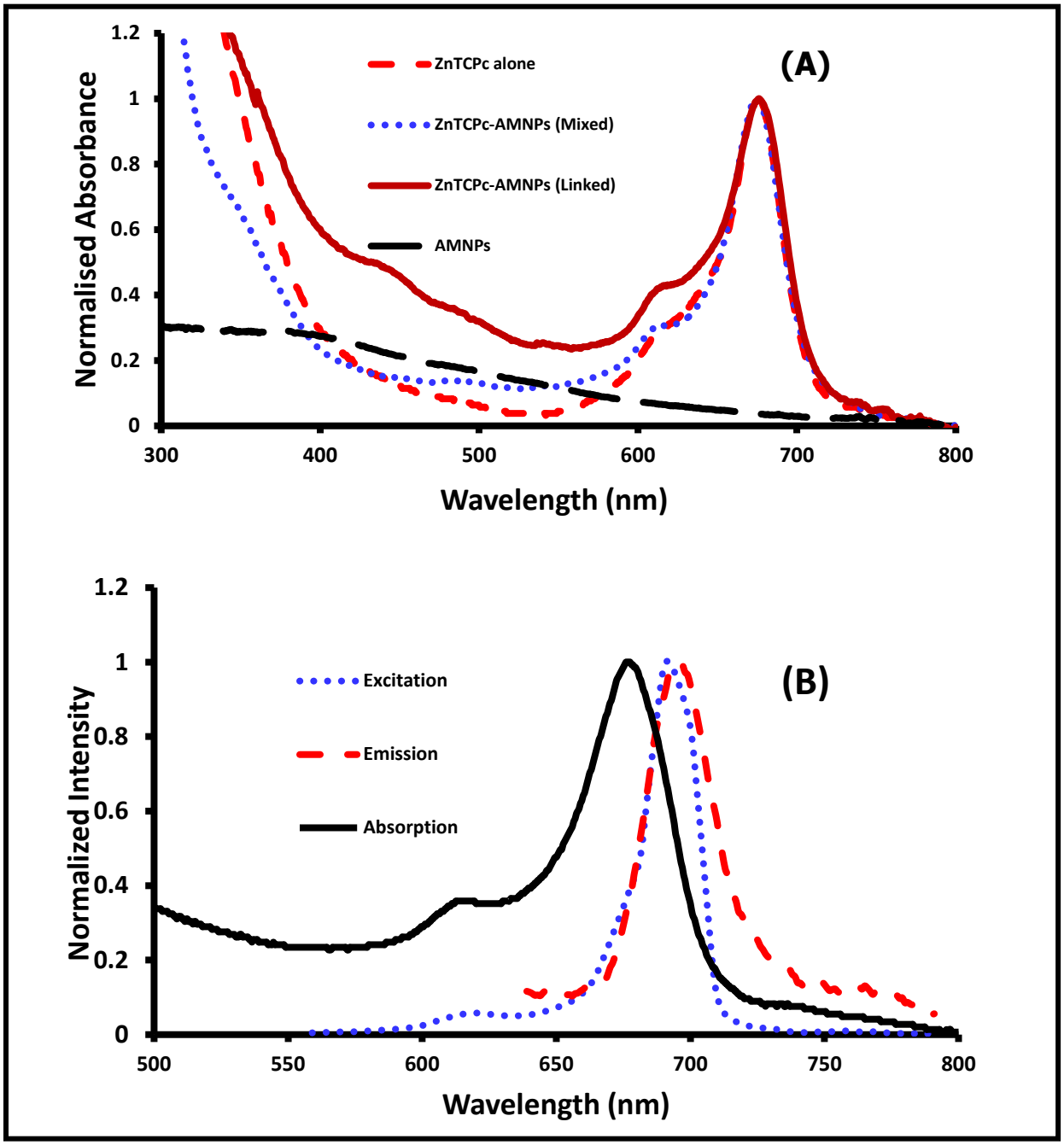

Figure 3.5: Ground state absorption spectra of (A) AMNPs, ZnTCPc, ZnTCPc-AMNPs (mixed) and ZnTCPc-AMNPs (linked); (B) Ground state absorption, fluorescence emission and excitation spectra of ZnTCPc-AMNPs (linked). Solvent EtOH: 0.5 M NaOH (1:1), λ exc = 620 nm.

3.2.3 PXRD patterns (p 58)

The AMNPs PXRD pattern, Figure 3.6 (i) shows peaks characteristics of a face centered cubic structure of 2θ values, 30 ^{o}, 36 ^{o}, 43 ^{o}, 54 ^{o}, 57 ^{o} and 63 ^{o}, with the hkl Miller indices of (220), (311), (400), (422), (511) and (440), respectively. These characteristics correspond to what have been reported in literature before **[147]**. Moreover, the peak at 2θ~18^{o} is due to the amorphous silica [**33**]. ZnOCPc has sharp peaks which upon conjugation they overlap with those of AMNPs, Figure 3.6 (ii) and (iii). ZnTCPc-AMNPs (linked) show peaks matching those of the magnetite pattern, Figure 3.7. ZnTCPc shows one weak peak at 2θ = 26^{o}, Figure 3.7 (inset), which is characteristic of Pcs [**148**]. These peaks overlap with the AMNPs pattern. The minimum crystalline sizes of the AMNPs and their conjugates were estimated using Debye-Scherrer equation and focusing on the 2θ = 36^{o} (311) peak. The calculated size of the amino functionalised MNPs is 11 nm. The size was found to be 12.5 nm for ZnTCPc-MNPs and 12.0 nm for ZnOCPc-MNPs. The increase in size and the appearance of new peaks confirms the combination of AMNPs with ZnTCPc or ZnOCPc.

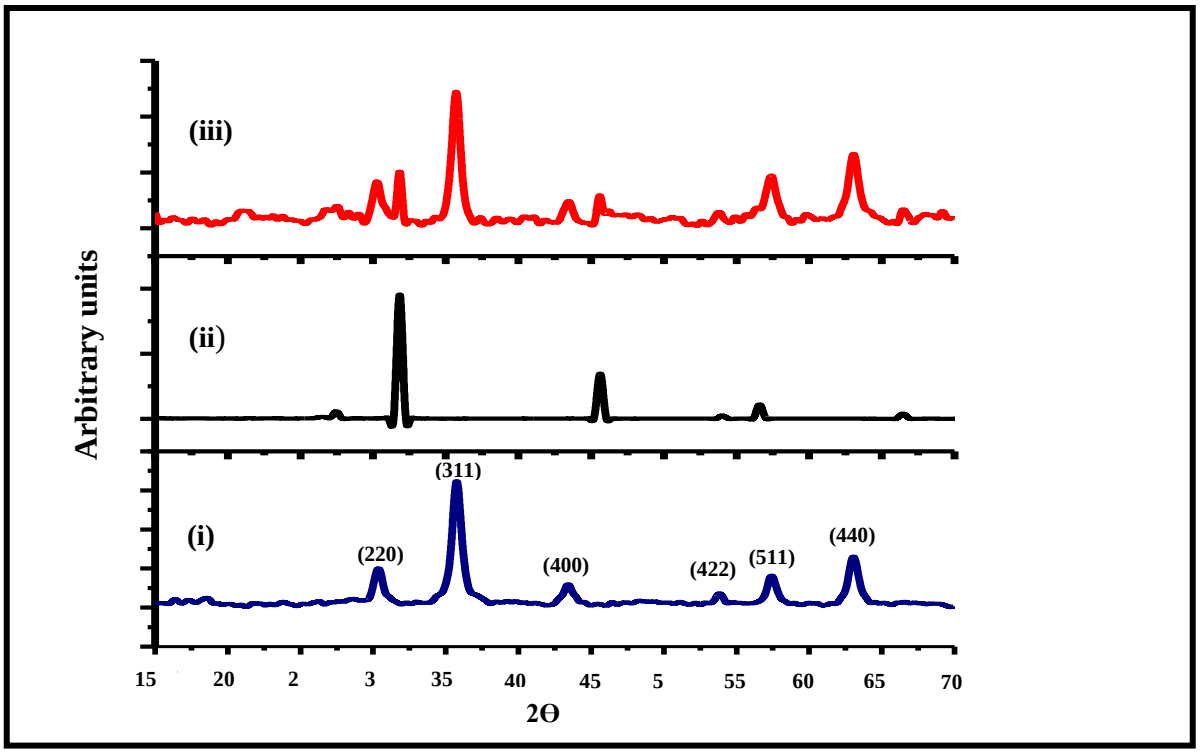

Figure 3.6: Powder X-ray diffraction patterns of (i) AMNPs, (ii) ZnOCPc, (iii) ZnOCPc-AMNPs (linked).

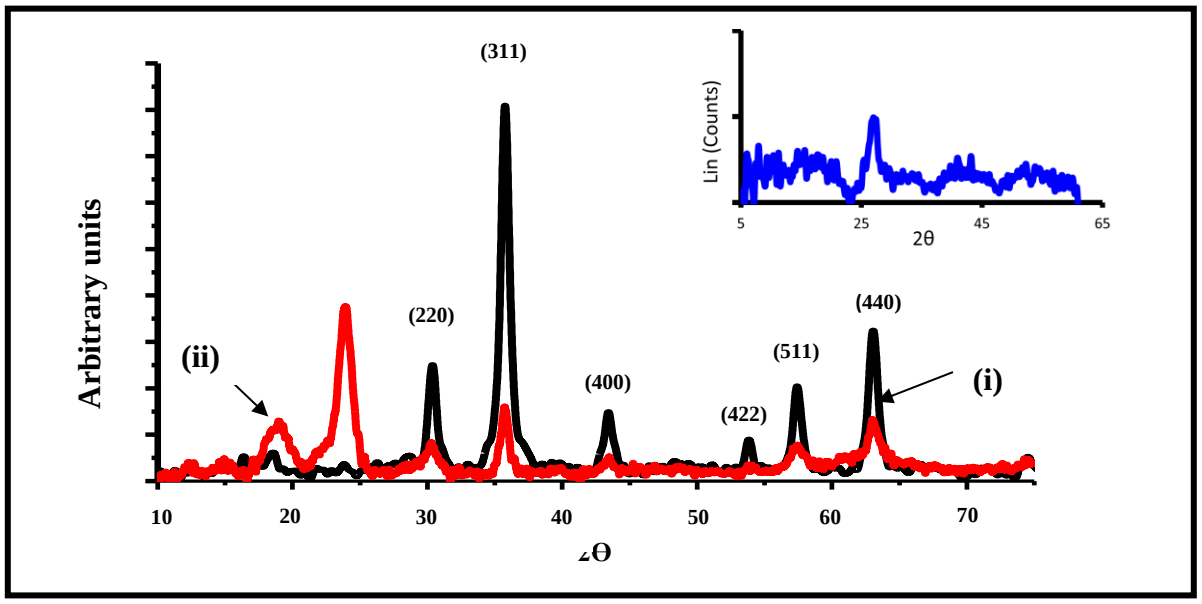

Figure 3.7: Powder X-ray diffraction patterns of (i) AMNPs and (ii) ZnTCPc-AMNPs (linked). Inset = PXRD pattern of ZnTCPc.

3.2.4 TEM (p 60, 61)

The TEM images of the CMNPs, AMNPs, ZnTCPc-AMNPs (linked) and ZnOCPc-AMNPs (linked) are as shown in Figure 3.8. The CMNPs shown in Figure 3.8 (A) are spherical and not aggregated. Functionalizing them with APTES, Figure 3.8 (B) resulted in aggregation and the aggregation continues upon linking to the ZnTCPc and ZnOCPc, Figure 3.8 (C) and (D), respectively. This aggregation could be due to the drying of the nanoparticles on the TEM grid. The average size of the CMNPs, AMNPs, and ZnTCPc-AMNPs and ZnOCPc-AMNPs are 9 nm, 11 nm, 12.5 nm and 12.98 nm, respectively. The sizes obtained from TEM, were determined by means of plotting the particle size distribution histograms and they are in close proximity with the minimum sizes obtained by PXRD above.

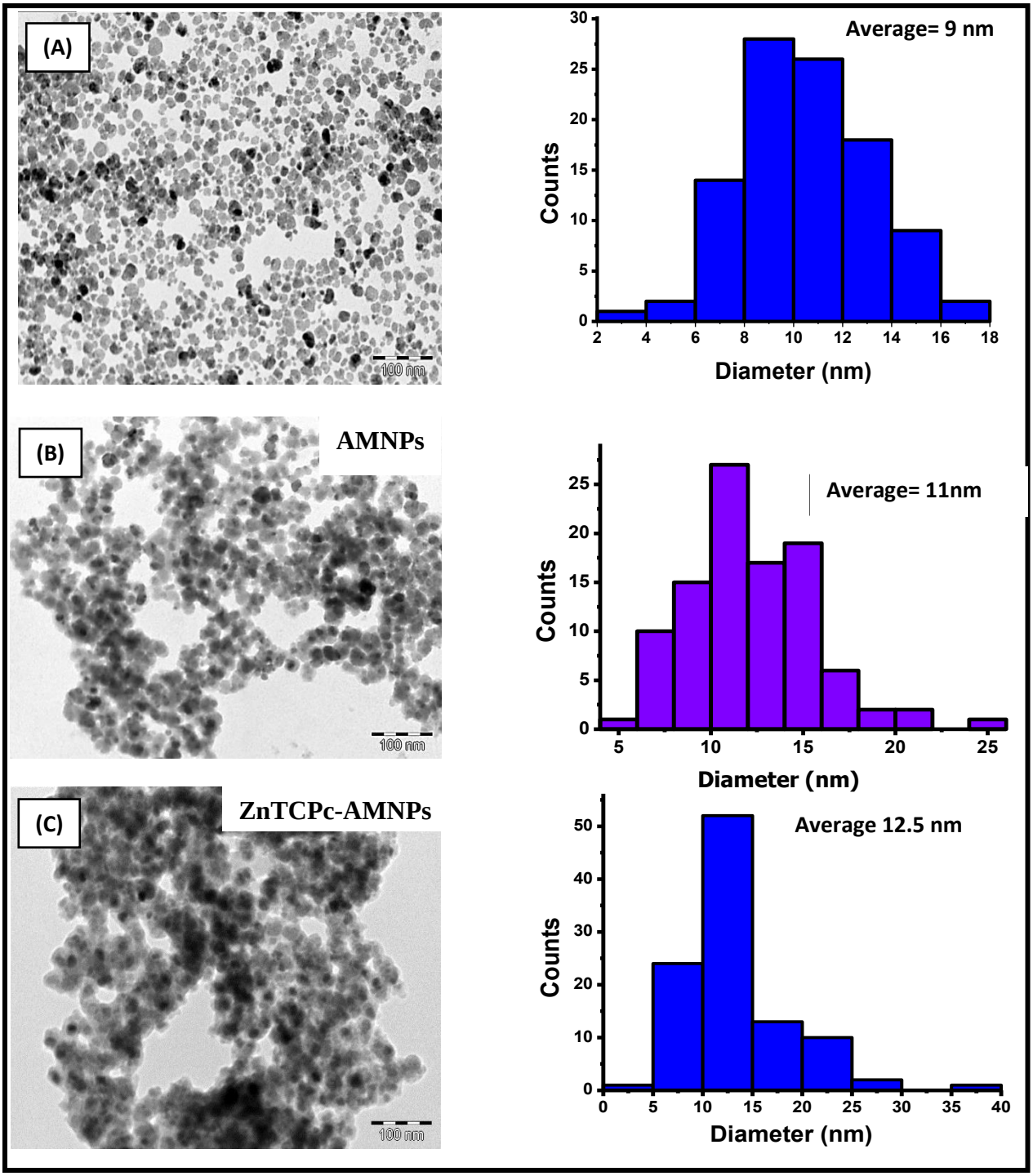
(A)
100 nm
Average= 9 nm
Counts
Diameter (nm)
(B)
AMNPs
100 nm
Average= 11nm
Counts
Diameter (nm)
(C)
ZnTCPc-AMNPs
100 nm
Average 12.5 nm
Counts
Diameter (nm)

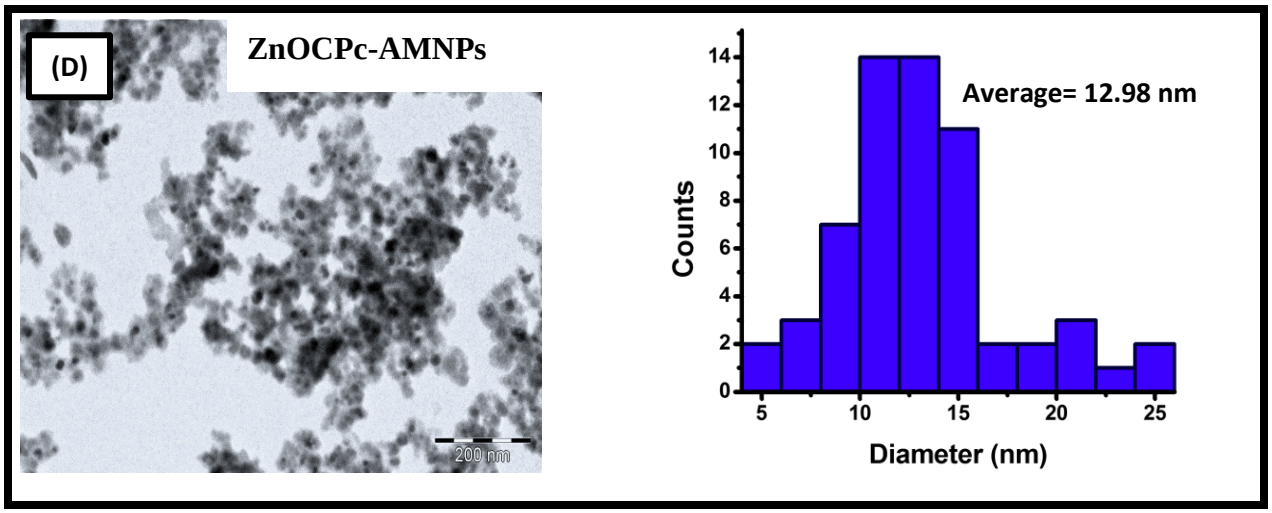

Figure 3.8: TEM images showing in (A) CMNPs, (B) AMNPs, (C) ZnTCPc-AMNPs (linked), (D) ZnOCPc-AMNPs (linked), and their corresponding size distribution histograms.

3.2.5 Energy dispersive x-ray spectroscopy (EDS)

Energy dispersive x-ray spectroscopy (EDS) was used to assess the elemental composition of AMNPs, Figure 3.9. The presence of Fe and O confirms the formation of the iron oxide nanoparticles, while the silicon (Si) and carbon (C) signals are due to the ethoxy silane groups on the surface of the AMNPs, Figure 3.9.

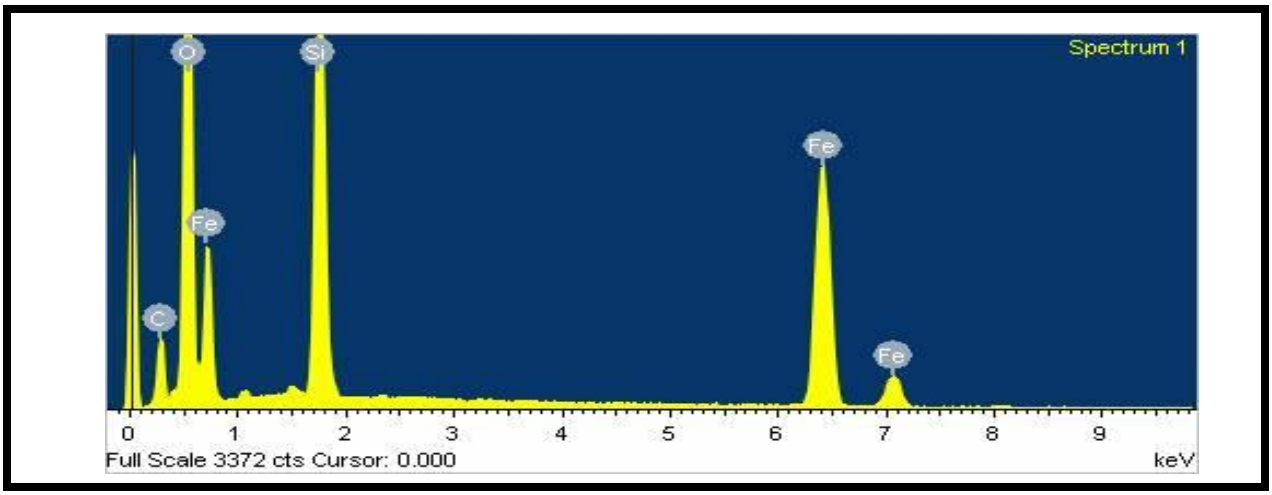

Figure 3.9: EDS profile of AMNPs

3.2.6 Thermogravimetric analysis (TGA)

Thermogravimetric analysis (TGA) was used to examine the organic content of the surface of AMNPs. The TGA curve for AMNPs, Figure 3.10 (i), shows two weight loss steps i.e. an initial loss of 13.4 % (which is attributed to moisture) at ~100 ^{o}C and a slow decomposition step (17.6 %) over ~400 ^{o}C which could be due to the loss of 3-aminopropyl-triethoxysilane (APTES) groups. The curve for ZnOCPc-MNPs, Figure 3.10 (ii) shows a weight loss of 42.3 % over 450 ^{o}C, with a sharp decomposition step at ~280 ^{o}C. The weight loss may be due to the decomposition of the ZnOCPc and the amino-propyl silane groups on the MNPs surface. This would mean that the amount of ZnOCPc MNPs is 11.3 %. Figure 3.10 (iii) shows the decomposition profile for the ZnOCPc which develops as a slow decomposition step followed by a sharp decrease at ~500 ^{o}C.

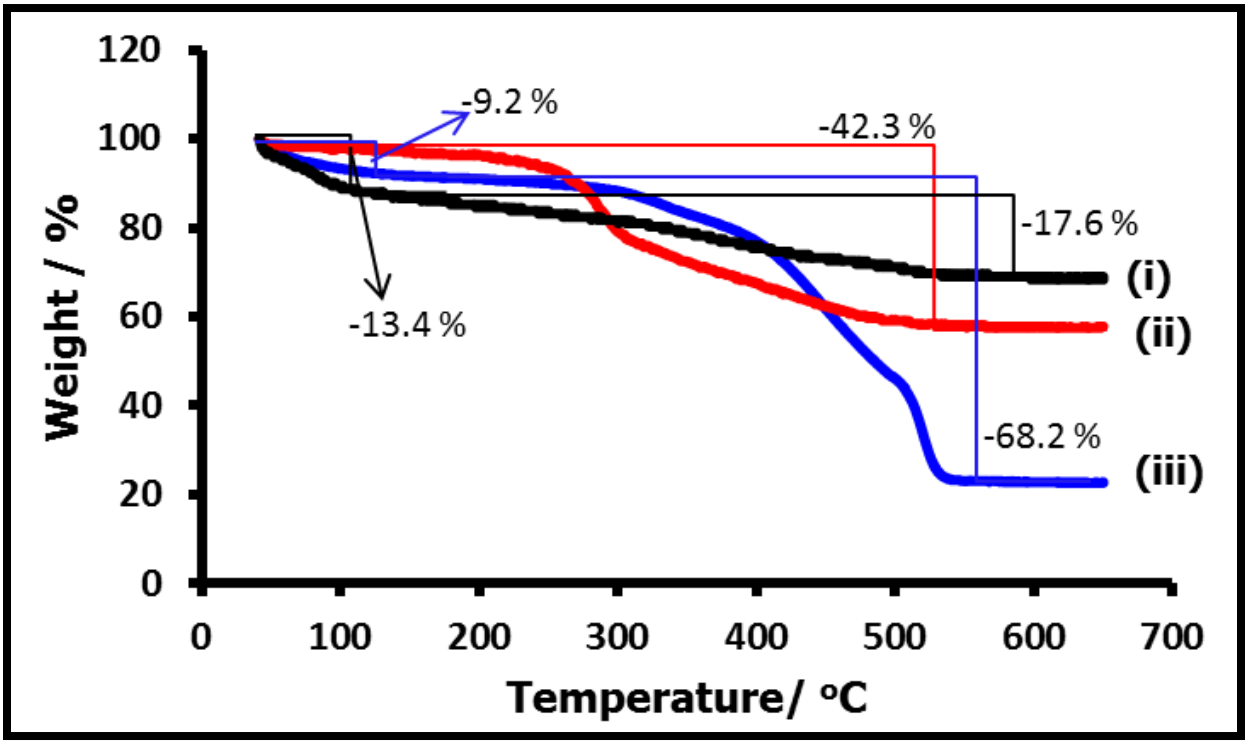

Figure 3.10: TGA curves of (i) AMNPs, (ii) ZnOCPc-MNPs and (iii) ZnOCPc

3.3 Photophysical and photochemical parameters

The effect of AMNPs on the photophysicochemical parameters of ZnOCPc and ZnTCPc were studied, the data is shown in Table 3.2.

Table 3. 2: The photophysical and photochemical parameters of ZnTCPc and ZnOCPc as well as their mixtures and conjugates with AMNPs.

Complex	Solvent	Φ_F	τ_F (ns)	Φ_T	τ_T (μs)	Φ_Δ	τ_Δ (μs)
ZnTCPc	EtOH: NaOH (1:1)	0.01	2.86 (92.4 %) 0.79 (7.64 %)	0.32	118	0.12	0.8 (±0.01)
ZnTCPc-AMNPs (mixed)	EtOH: NaOH (1:1)	<0.01	0.01 (73.3 %) 2.81 (26.3 %)	0.30	151	0.17	0.9 (±0.01)
ZnTCPc-AMNPs (linked)	EtOH: NaOH (1:1)	<0.01	3.16 (100 %)	0.37	192	0.26	2.3 (±0.2)
ZnOCPc	pH 9 buffer	0.15	2.90 (100%)	0.34 [71, 152]	62	0.21	1.7 (±0.4)
ZnOCPc-AMNPs (mixed)	pH 9 buffer	0.12	2.91 (79%) 0.01 (21%)	0.32	67	0.24	2.2 (±0.1)
ZnOCPc-AMNPs (linked)	pH 9 buffer	0.09	3.0 (100%)	0.41	147	0.31	8.5 (±0.3)

3.3.1 Fluorescence quantum yields and lifetimes

The Φ_F value for ZnOCPc-AMNPs (linked) or ZnTCPc-AMNPs (linked) were found to be much lower than that for Pc alone due to increased intersystem crossing in the presence of the heavy, paramagnetic AMNPs, Table 3.2. Time resolved fluorescence decay curves are shown in Figures 3.11 and 3.12, the fluorescence lifetimes (τ_F) are listed in Table 3.2. One lifetime was observed for ZnOCPc alone, ZnOCPc-AMNPs (linked) or ZnTCPc-AMNPs (linked) while two lifetimes were found for ZnTCPc, ZnOCPc-AMNPs (mixed) or ZnTCPc-AMNPs (mixed). The presence of two lifetimes in the mixed compounds may suggest the presence of differently oriented, closely packed Pc molecules on the AMNP surface [**149**]. For ZnTCPc alone, two lifetimes may be due to quenched and unquenched fluorescence caused by aggregation **[150]**.

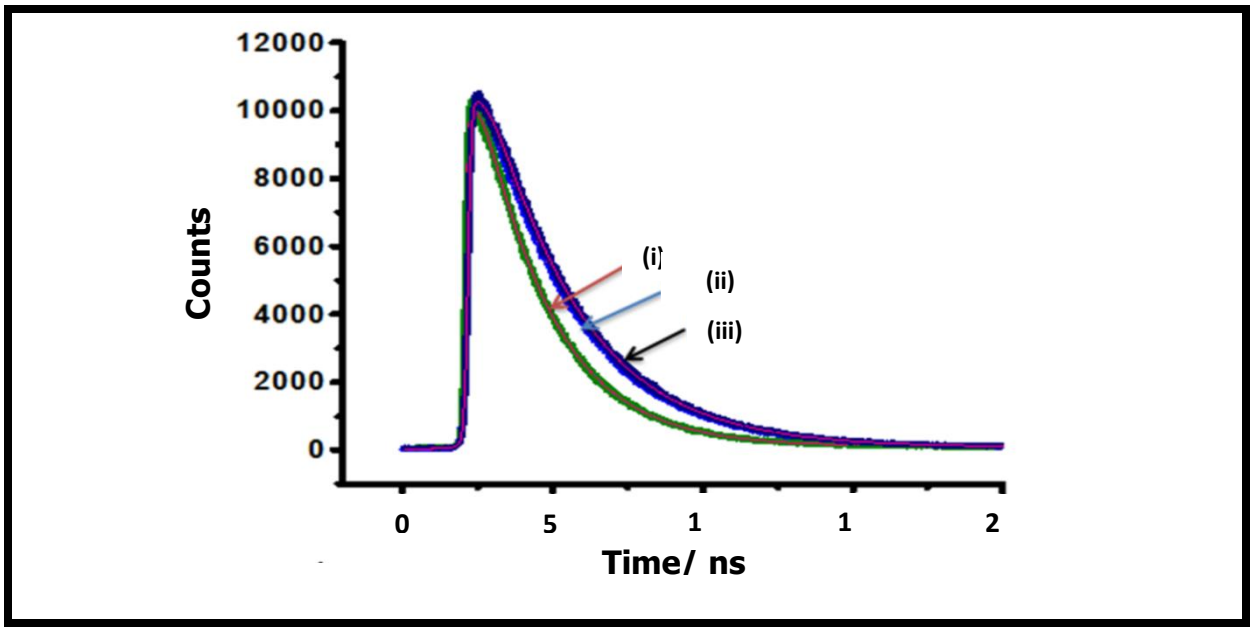

Figure 3.11: Fluorescence decay curves of (i) ZnOCPc (ii) ZnOCPc-AMNPs (mixed) and (iii) ZnOCPc-AMNPs (linked) in pH 9 buffer.

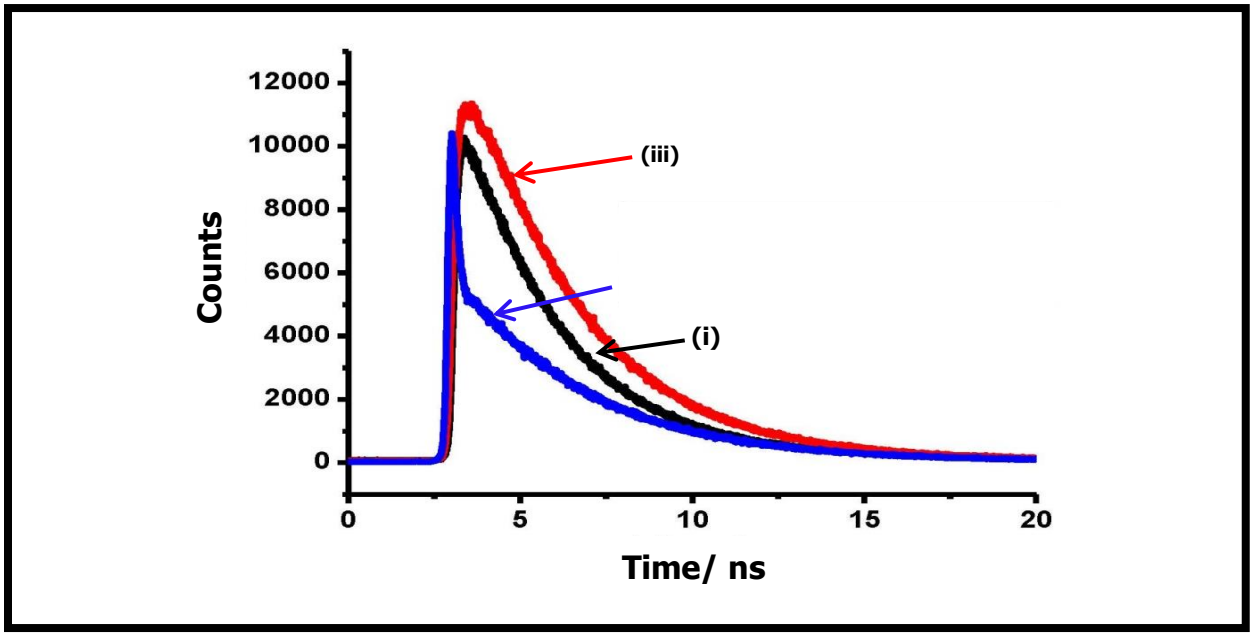

Figure 3.12: Fluorescence decay curves of (i) ZnTCPc, (ii) ZnTCPc-AMNPs (mixed) and (iii) ZnTCPc-AMNPs (linked) in EtOH:NaOH (1:1).

3.3.2 Triplet quantum yields and lifetimes

The triplet quantum yields and lifetimes are listed in Table 3.2. Figure 3.13 shows a representative triplet decay trend for ZnOCPc and ZnOCPc-AMNPs (both mixed and linked). The curves obeyed the first order kinetics for ZnTCPc or ZnOCPc together with their conjugates. The Φ_T value was found to increase for the ZnTCPc-AMNPs (linked) or ZnOCPc-AMNPs (linked) when compared to either ZnTCPc or ZnOCPc alone, due to the heavy atom effect of AMNPs. Surprisingly, there is no increase in this value for the ZnTCPc-AMNPs (mixed) or ZnOCPc-AMNPs (mixed) samples when compared to ZnTCPc or ZnOCPc alone, even though the external heavy atom effect of the AMNPs could also play a role. This could be due to the distance between the Pc and AMNPs because there is no linkage. The higher Φ_T value corresponds to the lower Φ_F value for the ZnTCPc-AMNP (linked) or ZnOCPc-AMNPs (linked). Triplet state lifetimes of the ZnTCPc or ZnOCPc covalently linked with AMNPs are higher than those of the mixed samples and Pcs alone. It is expected that when triplet quantum yields increase, the triplet lifetimes should be shorter **[151]**. It was previously reported that MNPs increase the triplet lifetime of ZnPc [**144**]. In the presence of nanoparticles such as quantum dots, the increase in triplet lifetimes of the Pcs with increase in triplet quantum yield has been repeatedly observed [**152, 153**]. The long lifetimes for the ZnTCPc-AMNPs (linked) or ZnOCPc-AMNPs (linked) could be as a result of the protection afforded by the AMNPs to the phthalocyanine from the environment.

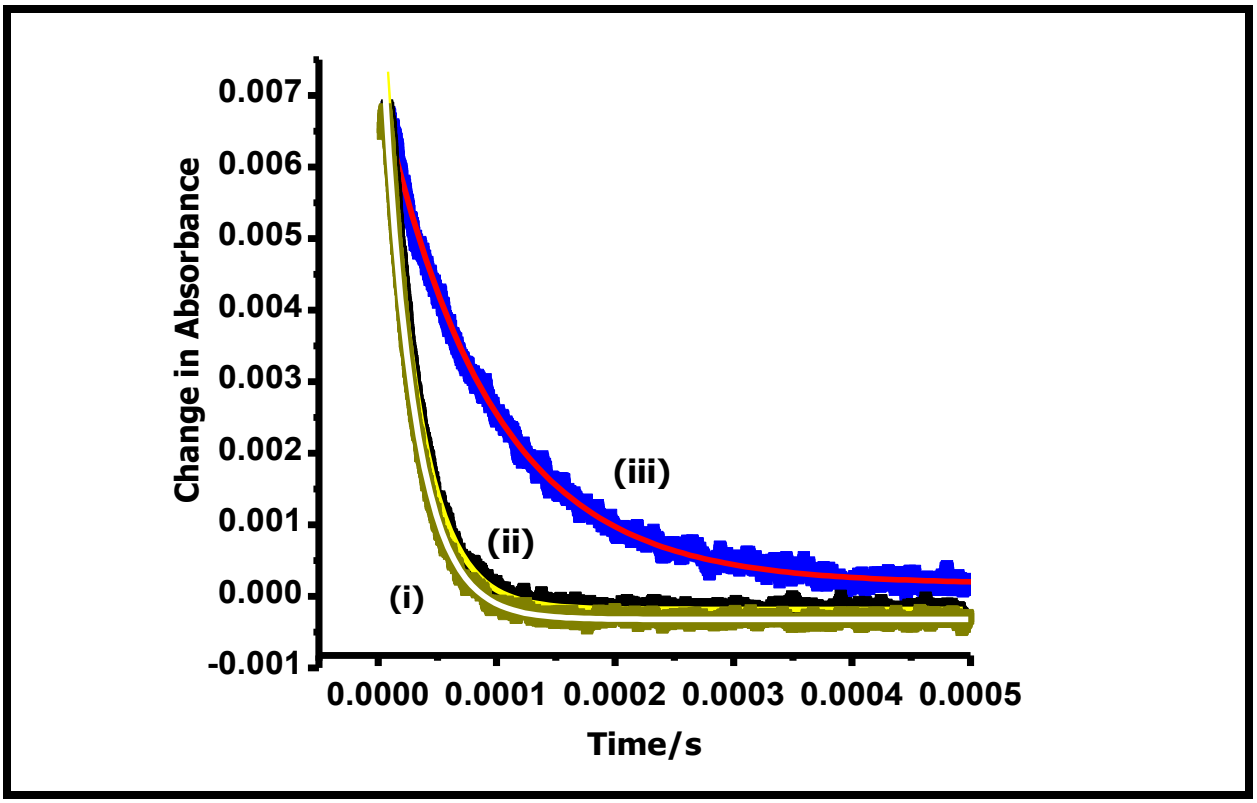

Figure 3.13: Triplet decay profile of (i) ZnOCPc (ii) ZnOCPc-AMNPs (mixed) and (iii) ZnOCPc-AMNPs (linked) in pH 9 buffer, λexc = 687 nm.

3.3.3 Singlet oxygen quantum yield (Φ_Δ) and lifetime (τ_Δ)

A representative $^1O_2$ phosphorescence decay curve is shown in Figure 3.14 and the Φ_Δ values are listed in Table 3.2. By chemically linking the AMNP with ZnOCPc or ZnTCPc, the Φ_Δ increased as compared to ZnOCPc-AMNPs (mixed), ZnOCPc and ZnTCPc alone, Table 3.2. This corresponds to the increased triplet quantum yields observed previously. An increase in Φ_Δ was observed for ZnOCPc-AMNPs (mixed) and ZnTCPc-AMNPs (mixed) even though there was no increase in their Φ_T. A longer singlet oxygen lifetime was observed for the ZnOCPc-AMNPs (linked) and ZnTCPc-AMNPs (linked) when compared to the ZnOCPc-AMNPs (mixed), ZnTCPc-AMNPs (mixed), ZnOCPc and ZnTCPc alone, Table 3.2.

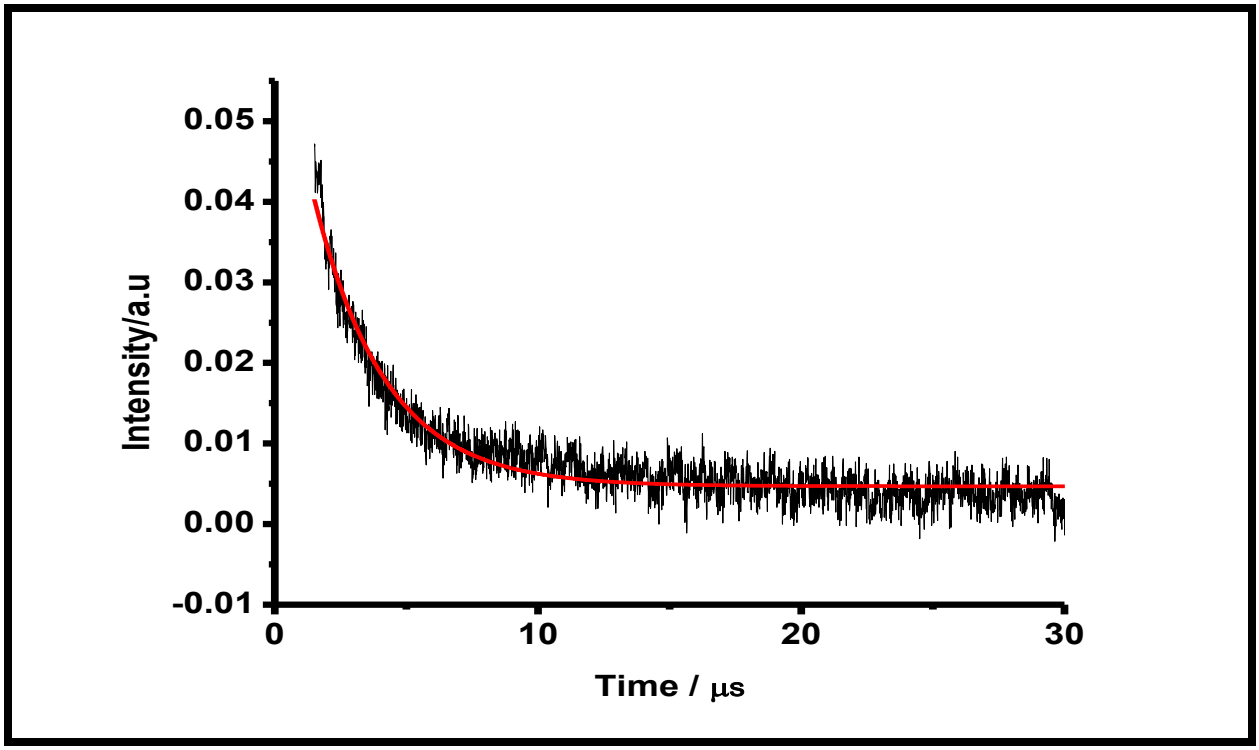

Figure 3.14: Singlet oxygen phosphorescence decay profile of ZnOCPc in pH 9 buffer solution.

In the subsequent chapter, the effects of elecrospinning parameters on the electropsun nanofibers are investigated. The thermal stability and the singlet oxygen generation ability of the fibers incorporated with Pc and Pc-AMNPs are also studied.

CHAPTER FOUR

Characterization of the fibers

4. Characterization of the electrospun fibers

This work reports on the investigation of the effect of solution parameters on the fiber morphology and size. The best electrospun solution is chosen for the incorporation of the phthalocyanine and phthalocyanine-magnetite conjugate. Moreover, the modified and unmodified fibers were characterized and the singlet oxygen quantum yields are also determined.

4.1 Electrospun PA-6 fibres

4.1.1. Polymer viscosity/concentration/molecular weight

The solution viscosity depends highly on the polymer concentration and has been found to have an effect on the fiber size and morphology **[154, 155]**. Fixing the polymer concentration and increasing the polymer molecular weight (B24 to B32) increases the solution viscosity, as shown in Table 4.1. Increasing the polymer concentration for the same polymer grade increases the viscosity and conductivity. The SEM images in Figure 4.1 also show that as we increase the polymer viscosity by increasing the concentration, the fiber diameter also increases, Table 4.2. However a similar trend was not observed for all polymer grades at different viscosities and concentrations. In order to obtain a small fiber diameter, the solution concentration should be as low as possible, which is useful in applications of fibers for filtering. However, at low polymer concentrations (i.e., lower viscosity); defects in the form of beading and droplets were observed (Figure 4.2 A). This is a characteristic of electrospraying instead of spinning. Additionally, the presence of junctions and bundles were observed, indicating that the fibers were still wet when reaching the collector. Increasing the solution viscosity by increasing the polymer concentration, uniform fibers with few beads and junctions were obtained, Figure 4.2 B. Figure 4.3 shows that as the polymer molecular weight increases the fiber diameter increases.

Table 4.1: The viscosity and conductivity of various polymer solutions used during the experiment. FA=Formic Acid, AA=Acetic Acid

Polymer grade	Polymer concentration (Wt. %)	Viscosity (cP)		Conductivity (mS/cm)	
		FA/AA		FA/AA	
		50/50 vol.%	75/25 vol.%	50/50 vol.%	75/25 vol.%
B24	10	100	114	0.643	1.930
	12	183	206	0.678	2.036
	14	384	349	0.716	2.055
	16	690	778	0.739	2.096
B27	10	141	177	0.646	1.972
	12	208	344	0.691	2.029
	14	576	576	0.722	2.069
	16	885	952	0.739	2.022
B32	10	188	284	0.633	1.894
	12	389	547	0.686	1.963
	14	796	1233	0.699	1.986
	16	1802	1666	0.700	1.995

4.1.2 Solvent ratio

Polyamide-6 dissolves in formic acid (FA) and not in acetic acid (AA) however, acetic acid acts as a stabilizer as stated by De Schoenmaker *et al* **[156]**. According to Pham *et al*. **[157]**, the conductivity of a PA-6 can be increased by adding a highly polar solvent or $MgCl_2$ without affecting the solution viscosity but having an impact on the fiber diameter. With an increase in the amount of formic acid, the conductivity and viscosity increases (Table 4.1) and thus the fiber diameter increases, Figure 4.4 and Table 4.2. The main reason for this is the higher dielectric constant of formic acid (57.29 at 25 ^{0}C). The high dielectric constant of formic acid is due its high polarity and it determines the charge distribution in a jet. Acetic acid has a lower dielectric constant (6.6 at 25 ^{o} C) than formic acid thus the higher the formic acid content, the higher the dielectric constant and the more the electric field pulls the polymer solution since the solution is more conductive. Most of the solutions with 75:25 volume ratios (FA/AA) were more electrospinnable than those of 50:50 volume ratios (FA/AA). Table 4.2 shows larger fiber diameter for high molecular weight and high polymer concentration.

81 nm **96 nm**

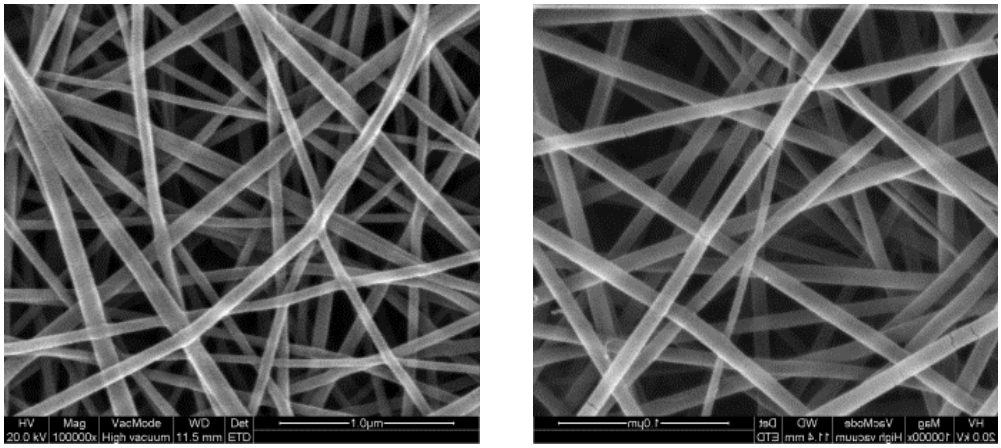

10 wt. % **12 wt. %**

112 nm **127 nm**

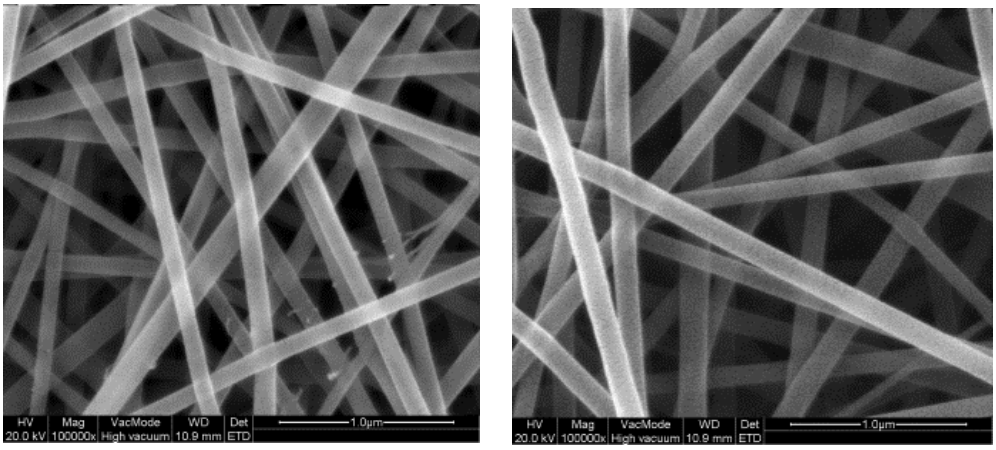

14 wt. % **16 wt. %**

Figure 4.1: SEM images showing the effect of PA-6 concentration (bottom) on the fiber diameter (top). B27 (Mw=80000), 75:25 (FA/AA). Relative humidity= ±48 % at 25 ^{o}C

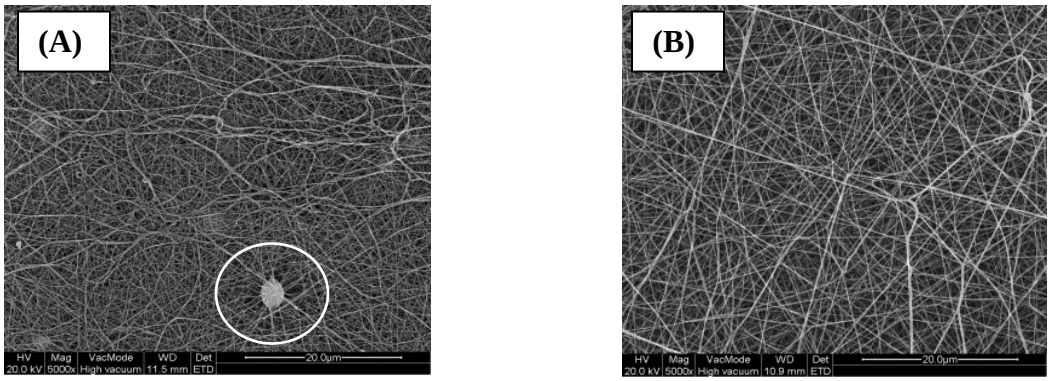

Figure 4.2: SEM images showing (A) beads and droplets at low viscosity 10 wt. % (B) no beads and droplets at higher viscosity. 16 wt. %, B27 (Mw=70000), 50:50 (FA/AA). Circled = bead. Relative humidity =49% at 22 ^{o}C

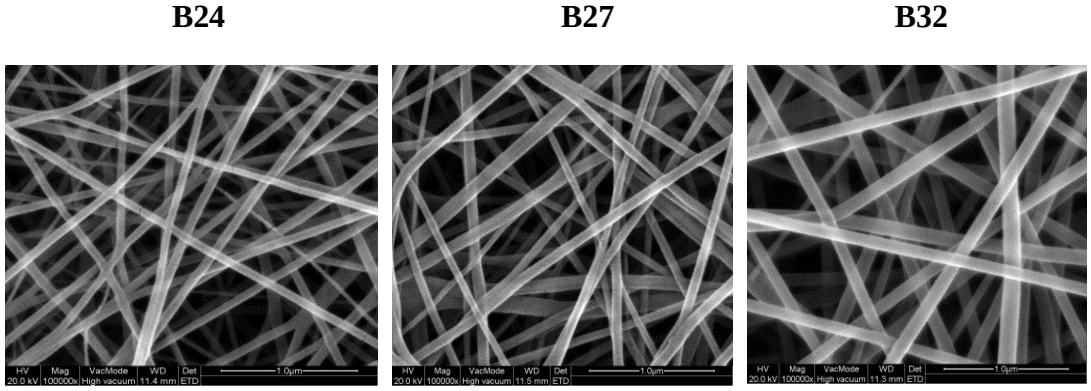

Figure 4.3: SEM images showing the effect of PA-6 grades on fiber diameter and morphology. B24 (Mw= 70000), B27 (Mw=80000), B32 (Mw 90000); 75:25 (FA/AA). Relative humidity= ± 49 % at 22 ^{o}C

B 32 (50:50 FA/AA) **B 32 (75:25 FA/AA)**

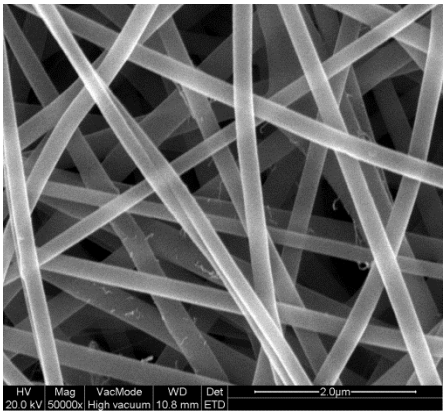

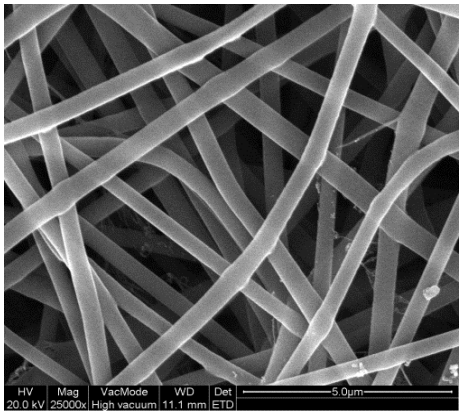

90 nm **108 nm**

Figure 4.4: SEM images showing the effect of solvent ratio FA/AA) on the fiber diameter and morphology. PA-6 grade B32 (Mw= 90000), Relative humidity = ± 48 % at 26 ^{o}C

Table 4.2: The effect of solvent ratio, polymer concentration and molecular weight on the fiber diameter (µm). FA/AA=50/50 and FA/AA=75/25

Polymer concentration (wt. %)	50:50 vol.% (FA/AA)			75/25 vol.% (FA/AA)		
	B24	**B27**	**B32**	**B24**	**B27**	**B32**
10	58	69	90	66	81	108
12	65	107	131	86	96	141
14	95	79	260	103	112	154
16	101	160	229	113	127	230

4.2 Electrospun fibers containing ZnOCPc and ZnOCPc-AMNPs

ZnOCPc has been used as an example representing ZnTCPc. It is reported before that anchoring a ZnPc into PA-6 solution could increase the conductivity and viscosity of the polymer solution **[158]**. The conductivity of the Pc central metal adds on the conductivity of the polymer solution. This is similar to the results we obtained when adding a ZnOCPc into polyamide solution. We first chose the best electrospun PA-6 grade and concentration (i.e., B 32 14 wt. %, 75:25 FA/AA) and thereafter different concentrations of ZnOCPc or ZnOCPc-AMNPs were added. B 32 14 wt. % was the best because there was no clogging and dripping of the polymer solution and furthermore the Taylor cone was stable. It is detailed in Table 4.3 that by fixing the polymer concentration and increasing the ZnOCPc concentration increases the solution viscosity, conductivity and thus the fiber diameter. A similar trend is expected when ZnOCPc-AMNPs is added. However, SEM images in Figure 4.1 did not show any change upon addition of ZnOCPc and ZnOCPc-AMNPs. Figure 4.5 shows the EDS spectrum of PA-6/ZnOCPc-AMNPs nanofiber. The appearance of the elements associated with the ZnOCPc-AMNPs conjugate on the EDS spectrum, confirms that the ZnOCPc-AMNPs was successfully embedded in the PA-6 nanofibers.

Table 4.3: The effect of ZnOCPc concentration on solution viscosity, conductivity and fiber diameter (nm). The FA/AA (75/25) solvent also contained 14 wt. % PA-6 polymer (B 32).

ZnOCPc concentration (mmol)	Viscosity (Cp)	Conductivity (mS/cm	Fiber diameter (nm)
0.1	1419	1.919	111
0.5	1890	1.975	156
1	2828	1.995	240

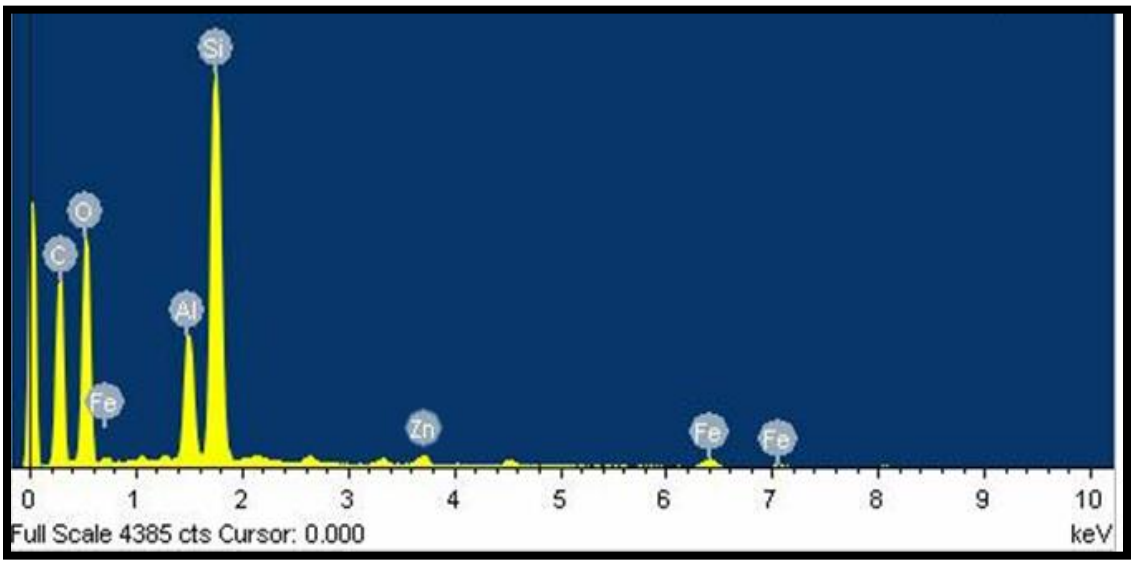

Figure 4.5: EDS spectrum of PA-6/ ZnOCPc-AMNPs nanofibers, spun from B32 14 wt. % (FA/AA) 75/25

4.2.1 Thermogravimetric analysis (TGA) (p 79)

The TGA thermograms in Figure 4.6 show a comparison between functionalized and unfunctionalized PA-6 nanofibers. In this study the thermal stability is regarded as a function of the relative amount of total mass loss . PA-6 nanofibers, Figure 4.6 (i), decomposed completely meaning no residuals were left. The first degradation stage for PA-6/ZnOCPc at 420 ^{o} C is due to the PA-6 nanofibers and the second degradation at 550 ^{o} C is due to the ZnOCPc in the nanofibers, Figure 4.6 (ii). In addition ZnOCPc alone not embedded in the fiber is thermally stable when compared to PA-6 alone, Figure 4.6 (iii). This would mean that the stability of PA-6 (Figure 4.6 (i)) is increased in the presence of ZnOCPc. The PA-6/ZnOCPc-AMNPs nanofibers, shows the first onset decomposition temperature below 300 ^{o} C, the second above 400 ^{o} C and the third decomposition above 500 ^{o} C, Figure 4.6 (iv). The first and third decompositions could be due the loss of fragments of the ZnOCPc-AMNPs conjugate and the second degradation could be due to the PA-6 because the second degradation onset temperature is close to that of PA-6 alone. The increased thermal stability of PA-6/ZnOCPc-AMNPs nanofibers is due to the thermally stable magnetite nanoparticles (MNPs). This confirms that the thermal stability of PA-6 nanofibers can be enhanced by functionalization with thermally stable nanoparticles.

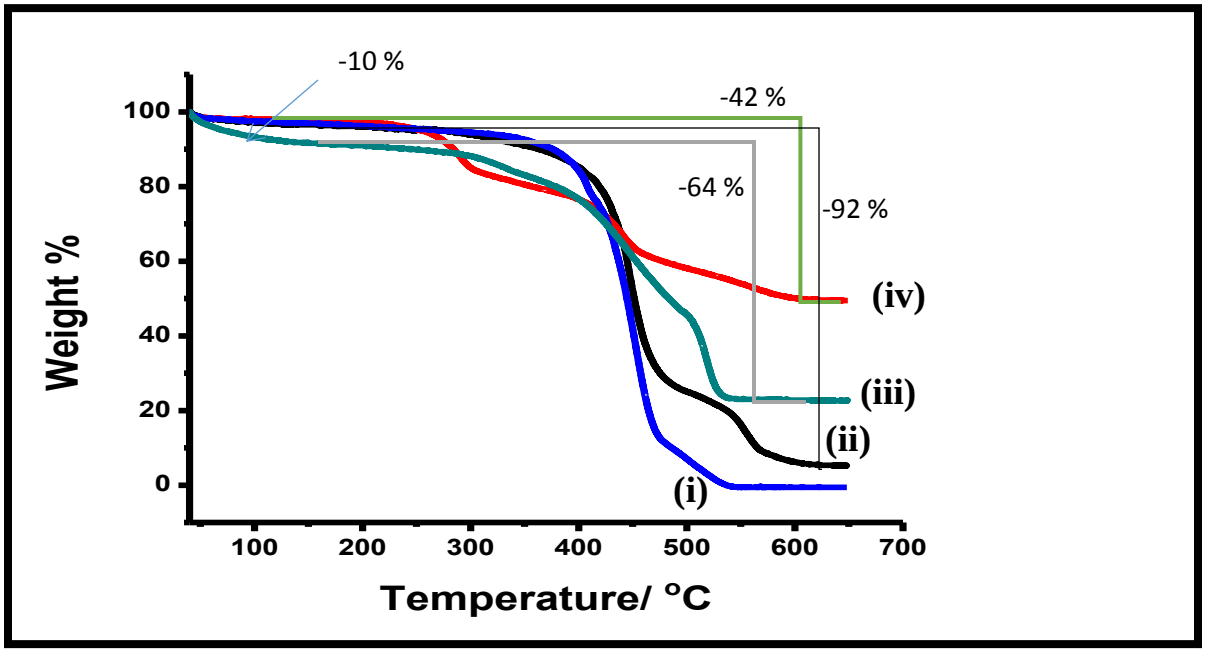

Figure 4.6: TGA thermograms of electrospun nanofibers of PA-6 (i), PA-6/ZnOCPc (ii), ZnOCPc alone (iii) and PA-6/ZnOCPc-AMNPs (iv).

4.2.2 Singlet oxygen generating ability of the functionalized fiber (p 80)

As stated already, singlet oxygen is involved in photocatalytic reactions. Hence it is important to determine the singlet oxygen generating ability of the modified fiber in the aqueous medium which is to be used for photocatalysis. The singlet oxygen quantum yield (Φ_Δ) determinations for the ZnOCPc and ZnOCPc-AMNPs in fibers were carried out in unbuffered aqueous media using ADMA as a quencher and its degradation was monitored at 380 nm, Figure 4.7. In each case 15 mg of the modified fiber was suspended in an aqueous solution of ADMA and irradiated using the photolysis set-up described in chapter 2. The singlet oxygen quantum yield (Φ_Δ) of the PA-6 fibers containing different amounts of ZnOCPc (hence different sizes) were 0.16 for the 111 nm, 0.21 for 156 nm, 0.24 for 240 nm, Table 4.4. For PA-6/ZnOCPc-AMNPs fibers the Φ_Δ

value is 0.37. The higher the Φ_{Δ} value, the more effective is the fiber for degradation of Orange-G, as discussed in the next chapter.

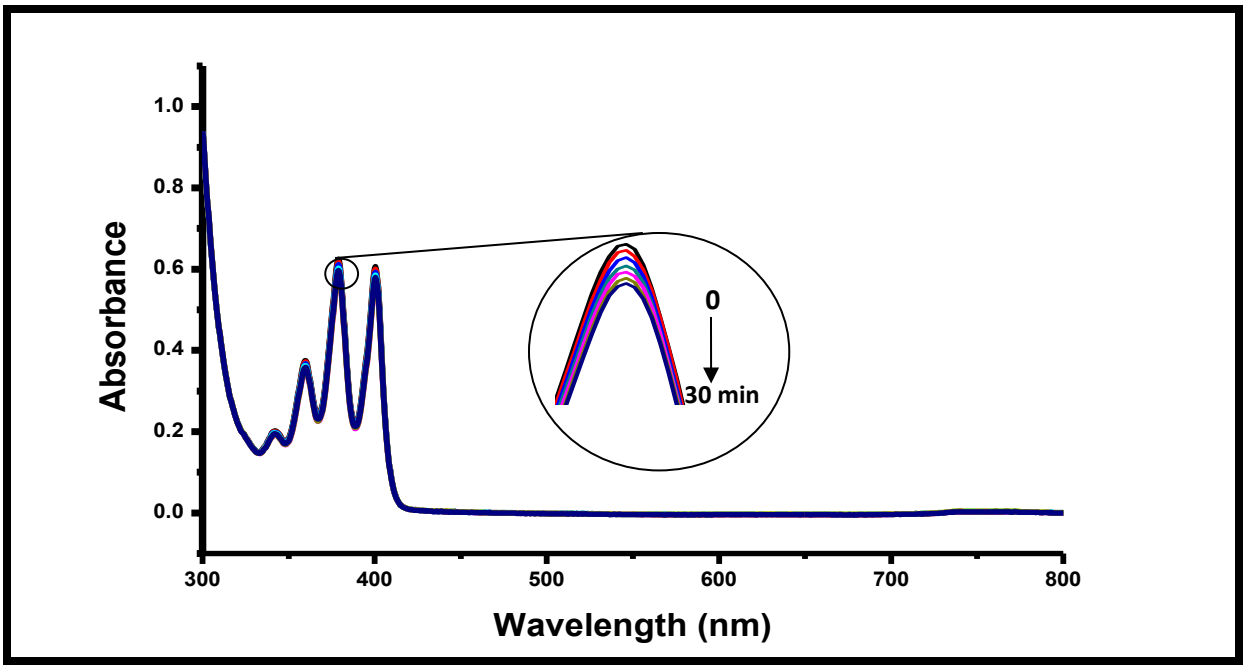

Figure 4.7: UV/Vis spectral changes observed upon photolysis of 15 mg of PA-6/ZnOCPc-AMNPs nanofibers in the presence of ADMA in unbuffered water for 30 min of photolysis. Starting ADMA concentration = 4.9×10^{-5} mol dm^{-3}, irradiation interval = 5 min.

Table 4.4: The effect of ZnOCPc concentration and ZnOCPc-AMNPs in fibers on the diameter and singlet oxygen quantum yields. Polymer formed from PA-6 (B 32, 14 wt. %) 75/25 (FA/AA).

ZnOCPc concentration (mmol)	Fiber diameter (nm)	Φ_{Δ} (in water)
0.1	111	0.16
0.5	156	0.21
1	240	0.24

ZnOCPc-MNP in mg	Fiber diameter (nm)	Φ_{Δ} (in water)
30	432	0.37

CHAPTER FIVE

Photodegradation of Orange-G

5. Photodegradation of Orange-G (OG)

Photodegradation of Orange-G was done using ZnOCPc or ZnOCPc-AMNPs in solution and when embeded in a fiber as examples. The kinetics for the photodegradation of OG (Figure 5.1 inset) using catalysts in different forms were studied.

5.1. UV/ Vis studies

Figure 5.1 shows the absorption spectral changes observed during the photolysis of Orange-G (OG) at 5 minutes intervals using ZnOCPc (A) and ZnOCPc-AMNPs (B) in solution. However, in solution, ZnOCPc is difficult to recovery without AMNPs. The OG absorption peak at 476 nm decreased upon light irradiation in the presence of the catalysts. When the photocatalysts were employed without irradiation and as well as in the absence of oxygen (*viz.* nitrogen purged solutions), no UV-Vis spectral changes were observed due to degradation of Orange-G (OG). The catalyst (ZnOCPc-AMNPs) could be reused following recovery with a magnet and rinsing with deionized water and methanol. PA-6/ZnOCPc-AMNPs nanofibers show a complete decomposition of OG (Figure 5.2) when compared to ZnOCPc-AMNPs in suspension. The absence of the Q-band of the phthalocyanine when using PA-6/ZnOCPc and PA-6/ZnOCPc-AMNPs nanofibers, indicates that there was no leaching of the Pc into the water, Figure 5.2. Unmodified fiber on its own showed no activity towards degradation of OG.

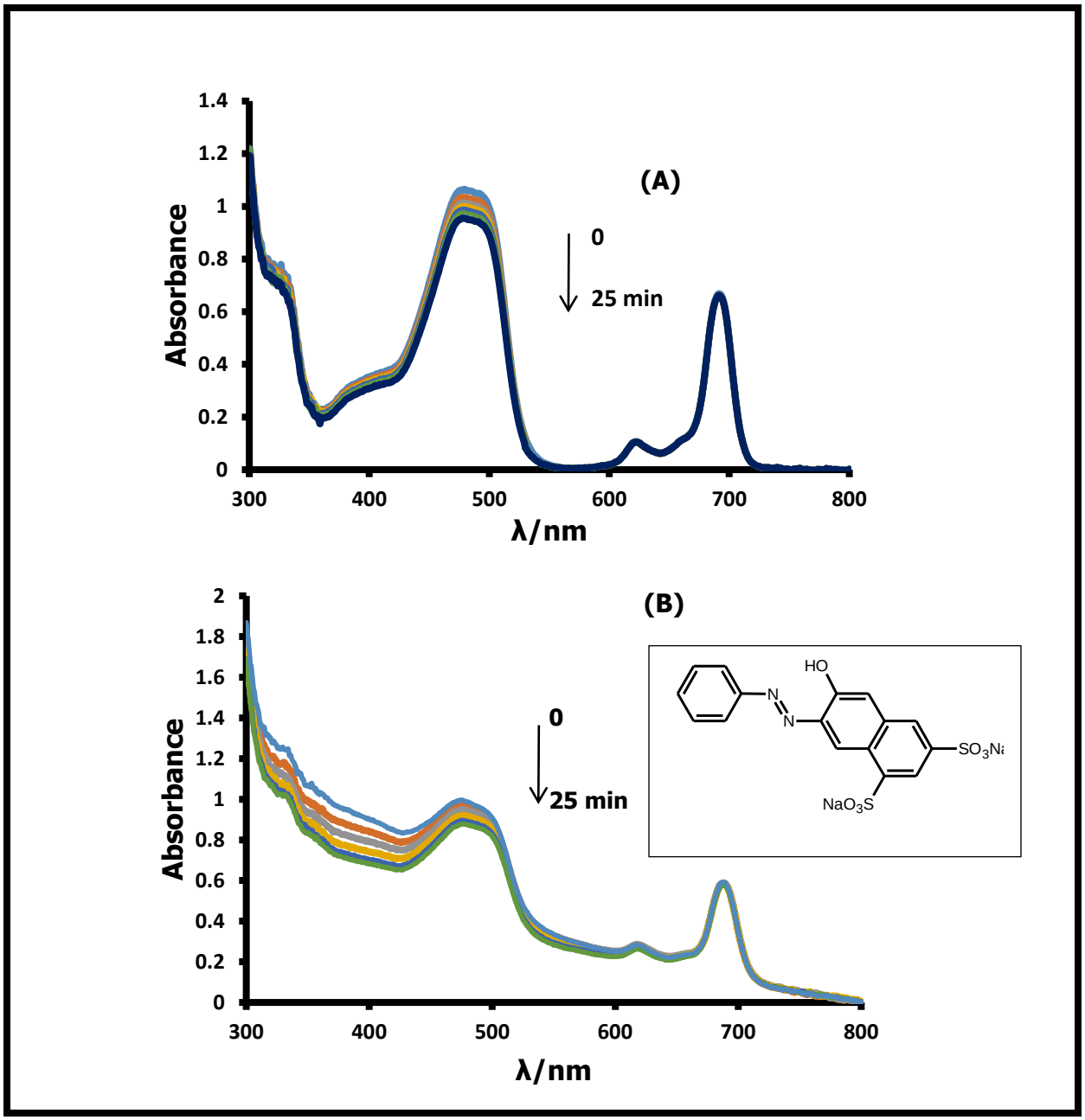

Figure 5.1: Electronic absorption spectra changes of 0.88 x 10^{-4} mol L^{-1} Orange G during visible light photocatalysis in the presence of ZnOCPc (A) and ZnOCPc-AMNPs (B), at 5 min intervals in unbuffered water. Inset= Orange-G structure.

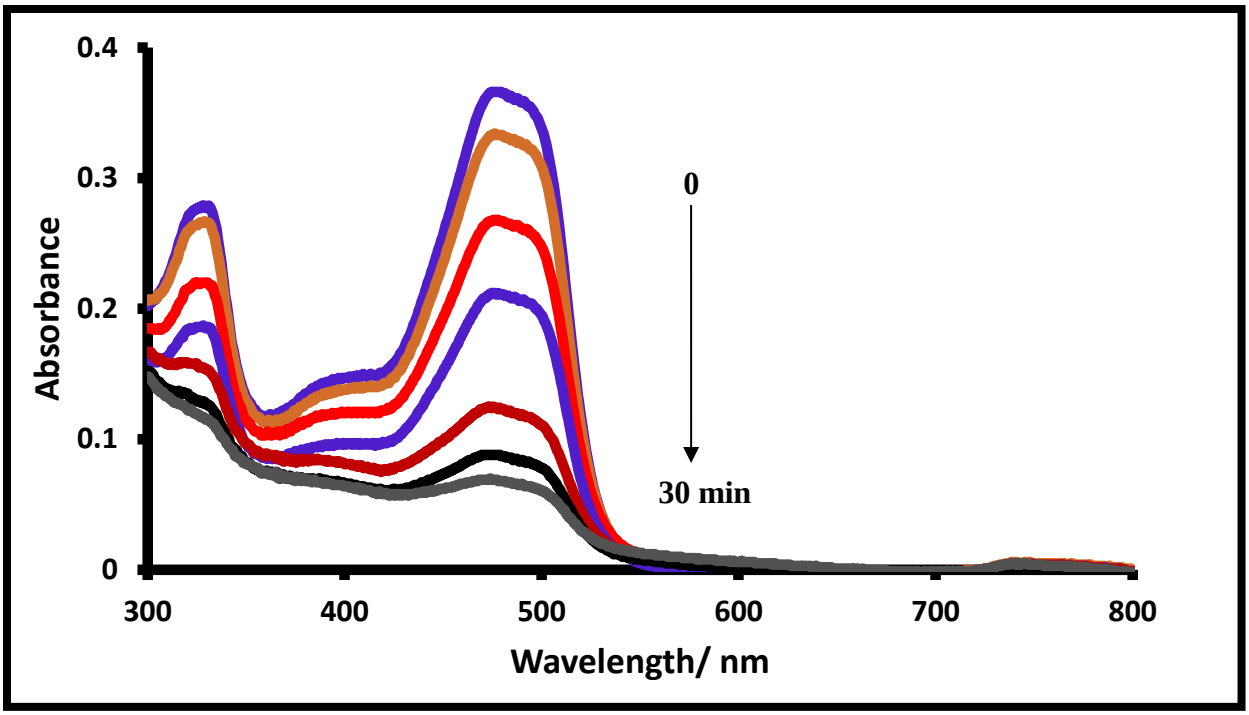

Figure 5.2: Electronic absorption spectra changes of 0.44 x 10^{-4} mol L^{-1} Orange G during visible light photocatalysis using 15 mg of PA-6/ZnOCPc-AMNPs nanofiber, at 5 min intervals in unbuffered water.

5.2 First order kinetics for the photodegradation of Orange-G (OG)

5.2.1 Catalyst in solution

Plots for the variation of OG concentration versus irradiation time are shown in Figure 5.3 using the data obtained from Figures, 5.1 and 5.2. The plots obtained for $In\left(\frac{C_o}{C}\right)$ versus time were linear indicating that the reaction follows first order reaction kinetics Figure 5.3. The observed rate constant (k_{obs}) decreased with an increase in dye concentration as expected. The k_{obs} values listed in Table 5.1 are larger for ZnOCPc-AMNPs when compared with ZnOCPc alone. This could be due to the improved singlet oxygen quantum yield for ZnOCPc-AMNPs. Thus ZnOCPc-AMNPs showed better catalytic behavior towards the photodegradation of OG than

ZnOCPc. Table 5.1 illustrates that the catalyst performance decreased slightly following reuse. This is shown by a decrease in the rate k_{obs} values when compared to the fresh catalyst. This could mean that the singlet oxygen generating capacity decreases as the catalyst is reused. The half-lives are also lower for ZnOCPc-AMNPs (used or fresh) compared to ZnOCPc alone.

Table 5.1: Shows the rate, rate constant (k_{obs}) and half-life ($t_{1/2}$) of various initial concentrations of OG using ZnOCPc-AMNPs. All studies in unbuffered water.

[OG]/ $\times 10^{-4}$ mol L^{-1}	k_{obs} /min^{-1}			Initial rate/ $\times 10^{-7}$ mol L^{-1} min^{-1}			Half-life/min		
	ZnOCPc	ZnOCPc-AMNPs	Reused ZnOCPc-AMNPs	ZnOCPc	ZnOCPc-AMNPs	Reused ZnOCPc-AMNPs	ZnOCPc	ZnOCPc-AMNPs	Reused ZnOCPc-AMNPs
0.44	0.0044	0.0053	0.0049	1.93	2.33	2.16	157	131	141
0.88	0.0026	0.0031	0.0027	2.28	2.72	2.38	267	224	257
1.33	0.0018	0.0021	0.0019	2.39	2.79	2.53	385	330	365
2.21	0.0011	0.0013	0.0012	2.43	2.87	2.65	630	553	577
2.65	0.0001	0.0011	0.0010	2.54	2.91	2.70	693	630	577

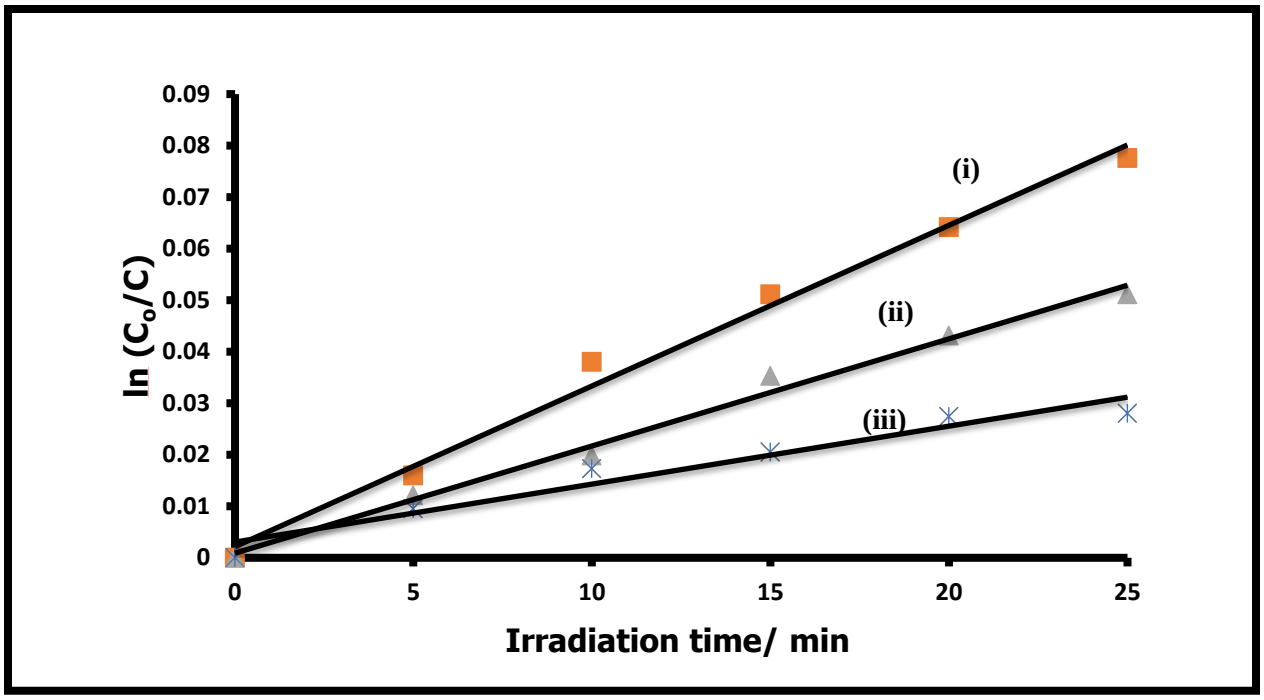

Figure 5.3: First order kinetics plots for degradation of OG; (i) 1.33 × 10^{-4}, (ii) 2.21 × 10^{-4} and (iii) 2.65 × 10^{-4} mol L^{-1} using ZnOCPc-AMNPs as a catalyst.

5.2.2 Catalysts on electrospun nanofibers

The plots of the variation of OG concentration versus irradiation time for PA-6/ ZnOCPc-AMNPs. are shown in Figure 5.4 and the kinetic data is listed in Table 5.2. First order reaction kinetics are also observed in this case. The k_{obs} rate follows the order PA-6/ZnOCPc-AMNPs> PA-6/ZnOCPc> ZnOCPc-AMNPs nanofibers, Table 5.2. This could be due to the improved singlet oxygen quantum yield for PA-6/ZnOCPc-AMNPs nanofibers. Thus better catalytic performace was observed for PA-6/ZnOCPc-AMNPs towards photodegradation of OG. However, the PA-6/ZnOCPc nanofibers improved with an increase in fiber size. The reduced half-lives for PA-6/ZnOCPc-AMNPs nanofiber also confirms that the catalyst was efficient.

Table 5.2: The rate constant (k_{obs}), initial rate and half-life ($t_{1/2}$) of various initial concentrations of OG using PA-6/ ZnOCPc-AMNPs nanofibers. Values in round brackets are for PA-6/ZnOCPc nanofiber. Values in square brackets are for ZnOCPc-AMNPs in solution (not embedded in fiber). All studies in unbuffered water. FD= Fiber diameter

[OG]/ $\times 10^{-4}$ mol L^{-1}	k_{obs} /min^{-1}				Initial rate/ $\times 10^{-6}$ mol L^{-1} min^{-1}				Half life/min			
		FD 111 nm	FD 156 nm	FD 240 nm		FD 111 nm	FD 156 nm	FD 240 nm		FD 111 nm	FD 156 nm	FD 240 nm
0.44	0.0490 [0.0053]	(0.031)	(0.035)	(0.041)	2.16 [0.23]	(1.36)	(1.54)	(1.80)	14 [131]	(22)	(20)	(17)
0.88	0.0444 [0.0031]	(0.026)	(0.029)	(0.032)	3.91 [0.272]	(2.29)	(2.55)	(2.82)	15 [224]	(27)	(24)	(22)
1.33	0.0324 [0.0021]	(0.020)	(0.022)	(0.023)	4.31 [0.279]	(2.66)	(2.93)	(3.10)	21 [330]	(35)	(32)	(30)
2.21	0.0201 [0.0013]	(0.013)	(0.015)	(0.016)	4.44 [0.287]	(2.87)	(3.32)	(3.54)	35 [553]	(53)	(46)	(43)
2.65	0.0175 [0.0011]	(0.011)	(0.013)	(0.014)	4.64 [0.291]	(2.99)	(3.45)	(3.71)	39 [630]	(61)	(53)	(50)

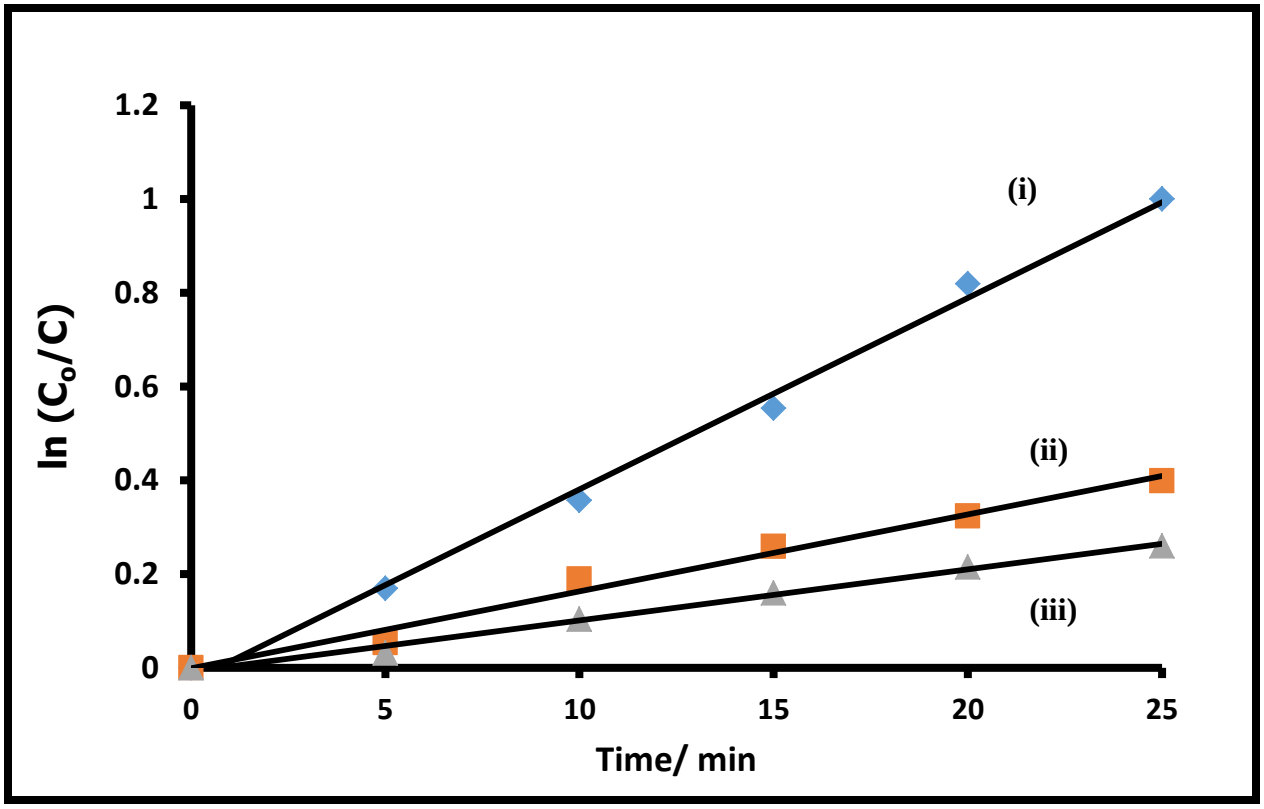

Figure 5.4: First order kinetics plots for degradation of OG; (i) 1.33 × 10^{-4}, (ii) 2.21 × 10^{-4} and (iii) 2.65 × 10^{-4} mol L^{-1} using PA-6/ZnOCPc-AMNPs nanofiber as a catalyst.

5.3 Langmuir-Hinshelwood kinetics

The Langmuir-Hinshelwood rate expression (Eq. 5.1) **[159]** may be used to describe the relationship between the initial rate of degradation of Orange G and the corresponding initial concentration. This model has successfully been applied to describe the kinetics of solid-liquid reactions, particularly heterogeneous photocatalytic degradation reactions. Since the ZnOCPc-AMNPs conjugate exists as a colloidal suspension, the Langmuir-Hinshelwood kinetic model may be employed. This model was also used for ZnOCPc or ZnOCPc-AMNPs fibers.

$$\frac{1}{r_0} = \frac{1}{kK_A}\frac{1}{C_o} + \frac{1}{k} \qquad (5.1)$$

where r_0 is the initial photocatalytic degradation rate (mol L^{-1} min^{-1}), C_o is the initial concentration of OG, k is the apparent reaction rate constant (mol L^{-1} min^{-1}) and K_A is the adsorption coefficient. $1/r_0$ was plotted against $1/C_o$, a linear fit with a non-zero intercept was obtained showing that the photodegradation of OG obeys the Langmuir-Hinshelwood kinetics model, Figure 5.5. The value of k can be obtained from the y-intercept, while K_A is obtained from the slope of the line, and they were estimated at 3.1×10^{-7} mol L^{-1} min^{-1} and 7.3×10^{4} mol^{-1} L, respectively, for ZnOCPc-AMNPs. k and K_A for reused catalyst (ZnOCPc-AMNPs) were estimated to be 2.8×10^{-7} mol L^{-1} min^{-1} and 7.9×10^{4} mol^{-1} L, showing only small changes in the catalyst activity, Table 5.3. K_A, the adsorption coefficient was slightly higher for the reused catalyst, suggesting that adsorption was more favored following reuse.

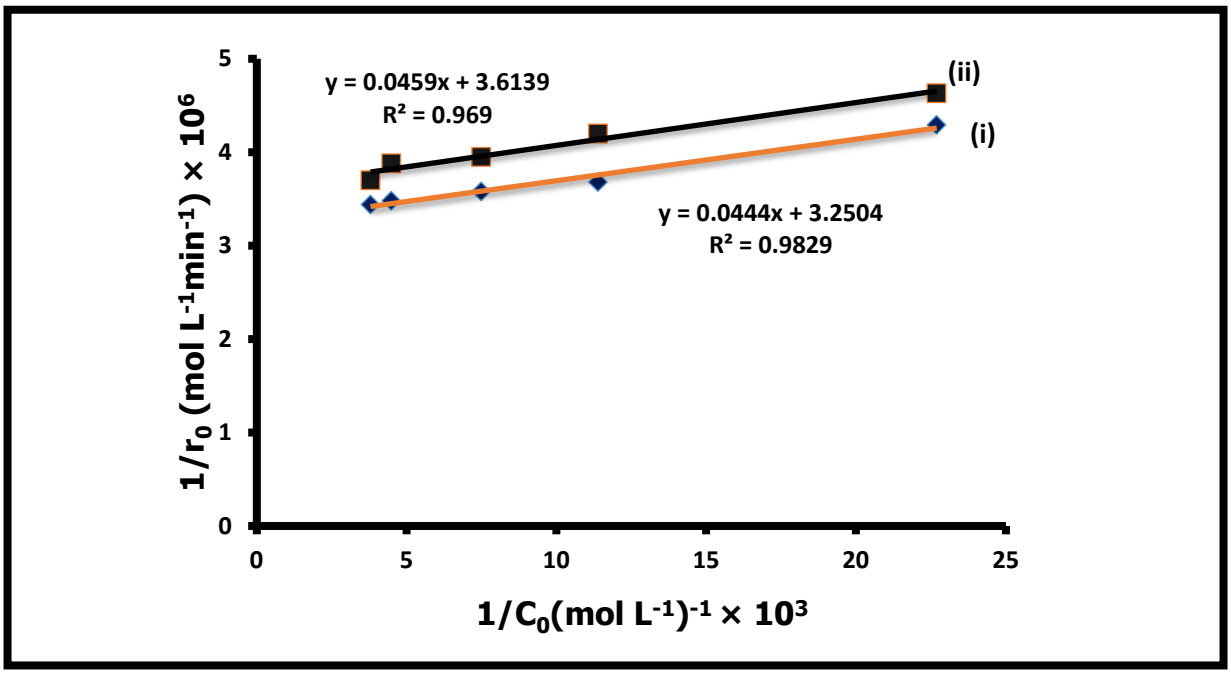

Figure 5.5: Plot of the reciprocal of initial reaction rate (1\r$_0$) vs. the reciprocal of the initial concentration of OG for photo-oxidation, (i) for the fresh catalyst (ZnOCPc-AMNPs) and (ii) for reused catalyst.

The results in Figure 5.6 also show that Langmuir-Hinshelwood kinetic model is a relevant model in describing the kinetics for the photodegradation following heterogeneous catalytic system based on the fiber supported phthalocyanine complexes. For the photocatalysts embedded in fibers, the Langmuir-Hinshelwood kinetics data is listed in Table 5.3. The value of k and K_A were estimated at 4.3×10^{-6} mol. L^{-1} min^{-1} and 1.1×10^{4} mol^{-1} L, respectively, for PA-6/ZnOCPc nanofiber (111 nm). k and K_A for PA-6/ZnOCPc-AMNPs nanofiber (were estimated to be 6.8×10^{-6} mol L^{-1} min^{-1} and 1.1×10^{5} mol^{-1} L respectively. K_A was estimated at 3.1×10^{-7} mol L^{-1} min^{-1} and k at 7.3×10^{4} mol^{-1} L for ZnOCPc-AMNPs in solution, showing better activity on the fiber than in solution. K_A, the adsorption coefficient is higher for PA-6/ZnOCPc-AMNPs nanofiber, suggesting that adsorption was more favored on the fiber.

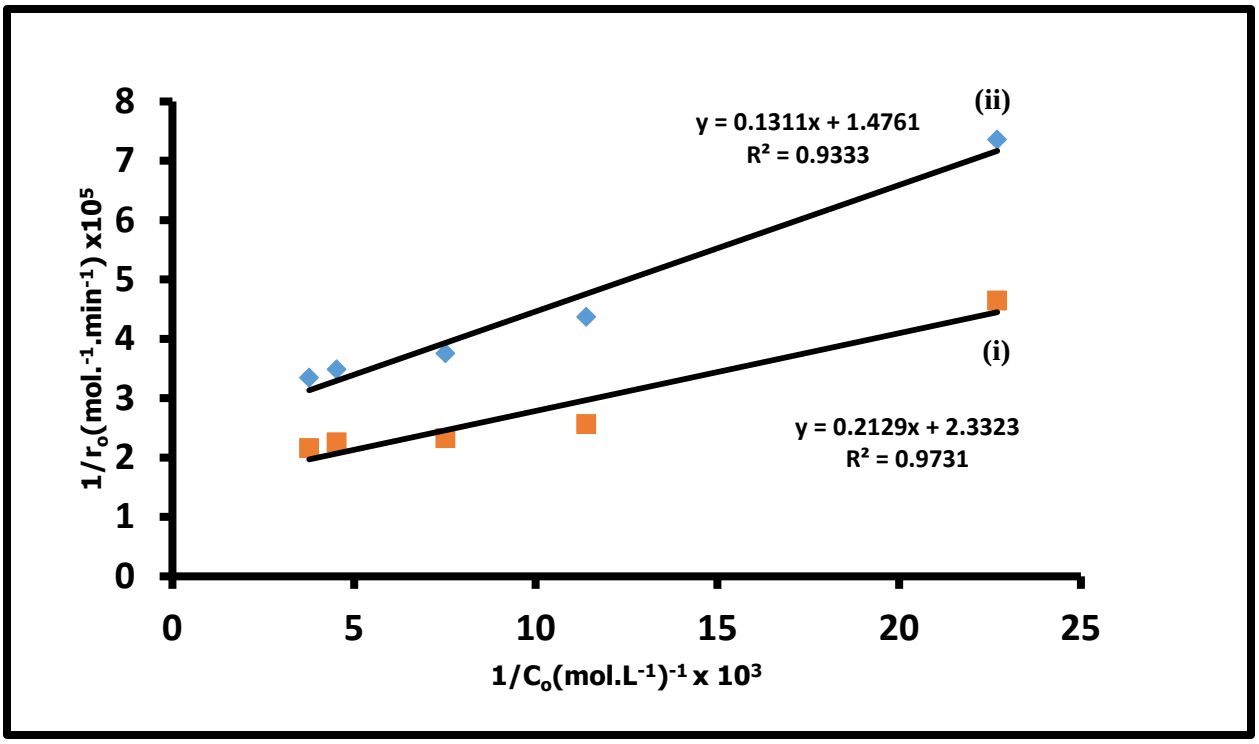

Figure 5.6: Plot of the reciprocal of initial reaction rate ($1/r_0$) vs. the reciprocal of the initial concentration ($1/C_0$) for photodegradation of OG, using (i) PA-6/ ZnOCPc-AMNPs and (ii) PA-6/ ZnOCPc-AMNPs nanofibers as catalysts in water.

Table 5.3: Langmuir-Hinshelwood parameters for photocatalysis of Orange-G using unbuffered water.

Catalyst	k mol L^{-1} min^{-1}	K_A mol^{-1} L	R^2
ZnOCPc-AMNPs (fresh)	3.1×10^{-7}	7.3×10^{4}	0.9829
ZnOCPc-AMNPs (reused)	2.8×10^{-7}	7.9×10^{4}	0.9690
PA-6/ZnOCPc-AMNPs fiber	6.8×10^{-6}	1.1×10^{5}	0.9731
PA-6/ZnOCPc (111 nm) fiber	4.3×10^{-6}	1.1×10^{4}	0.9333
PA-6/ZnOCPc (156 nm) fiber	4.9×10^{-6}	1.1×10^{4}	0.9851
PA-6/ZnOCPc (240 nm) fiber	4.8×10^{-6}	1.4×10^{4}	0.9874

CHAPTER SIX

CONCLUSIONS

Conlusions

ZnTCPc and ZnOCPc were chemically linked to AMNPs to form ZnTCPc-AMNPs and ZnOCPc-AMNPs conjugates. The FTIR spectra confirmed the linkage of the two systems by the presence of peaks attributed to an amide bond. TEM revealed that the nanoparticles synthesized are spherical but aggregated. The size of the MNPs (by TEM) increased upon functionalization and linkage to the Pcs, and that the sizes obtained agree with PXRD data. The increase in the background of the UV/Vis absorption spectra also shows the interaction of Pcs (ZnTCPc or ZnOCPc) with the AMNPs. The ground state absorption, fluorescence excitation and emission of ZnOCPc after mixing and linking with AMNPs did not alter significantly. The UV/Vis absorption spectra of ZnTCPc have shown a monomeric Q-band in EtOH:NaOH (1:1) and upon linking with MNPs. The fluorescence quantum yields decreased in the presence of AMNPs. Φ_T, Φ_Δ,τ_Δ and τ_T of ZnTCPc or ZnOCPc increased upon linking with AMNPs. Zinc octacarboxy phthalocyanine (ZnOCPc), as well as conjugates of ZnOCPc with AMNPs, were electrospun into fibers using polyamide 6 (PA-6). The functionality of the ZnOCPc and ZnOCPc-AMNPs was maintained within a solid fiber core. Good singlet oxygen quantum yields were obtained within the fibers. Orange-G was easily degraded by ZnOCPc-AMNPs as well as these fibre photocatalysts with the highest rate of degradation found for PA-6/ZnOCPc-AMNPs fiber due to its improved singlet oxygen quantum yield. The rate also increased with the size of the ZnOCPc-AMNPs fibers. The photodegradation of Orange-G is in agreement with both first order kinetics and Langmuir-Hinshelwood kinetics. We have found that MNPs induces the adsorption of Orange-G onto the catalyst surface, as shown by an increased adsorption coefficient (K_A) when PA-6/ZnOCPc-AMNPs fiber is used.

Future work

Hydrophobic magnetite nanoparticles synthesized via sol-gel method could also be conjugated to hydrophobic mono carboxyl phthalocyanines in which one linkage is used. The magnetic properties of iron platinum (FePt), iron palladium (FePd), and iron oxides (Fe_2O_3 and Fe_3O_4) need to be studied alone and also when conjugated with phthalocyanines. It would be of great interest to also compare different shapes of magnetic nanoparticles. Photodegradation comparing mono, di and tri-azo dyes as test pollutants need to be studied further. The effects of pH, temperature and catalyst loading on photodegradation can also be investigated. Products obtained upon degradation should be qualitatively characterized.

References

[1] K. S. Wilson, L. A. Harris, J. D. Goff, J. S. Riffle, J. P. Dailey, *Eur. Cell Mater*., 3 (2002) 206.

[2] M. Song, Y. Zhang, S. Hu, L. Song, J. Dong, Z. Chen, N. Gu, *Colloids Surf. A: Physicochem. Eng. Aspects,* 408 (2012) 114.

[3] K. S. Shin, Y. K. Cho, J. Choi, K. Kim, *Appl. Catal. A: Gen*., 413 (2012) 170.

[4] S. Sun, C. B. Murray, D. Weller, L. Folks, A. Moser, *Science*, 287 (2000) 1989.

[5] M. M. Miller, G. A. Prinz, S. F. Cheng, S. Bounnak, *Appl. Phys. Lett.*, 81 (2002) 2211.

[6] J. W. Bulté, *Methods Mol. Med.,* 124 (2006) 419.

[7] S. Laurenta, S. Dutz, U. O. Häfeli, M. Mahmoudi, *Adv. Colloid Interface Sci*., 166 (2011) 8.

[8] M. Hofmann-Amtenbrink, B. von Rechenberg and H. Hofmann, *Nanostructured Materials for Biomedical Applications*: Editor: M. C. Tan, Transworld Research Network 37/661 (2), Fort P.O., Trivandrum-695 023, Kerala, India (2009), Chp. 5, pp.122.

[9] Y. W. Jun, J. W. Seo, A, Cheon, *Acc. Chem. Res*., 42 (2008)179.

[10] P. Moodley, F. J. E. Scheijen, J. W. Niemantsverdriet, P. C. Thüne, *Catal. Today*, 154 (2010) 142.

[11] F. Horst, E.H. Rueda, M.L. Ferreira, *Enzyme Microb. Technol*., 38 (2006) 1005.

[12] M. S. Saeedi, S. Tangestaninejad, M. Moghadam, V. Mirkhani, I. Mohammadpoor-Baltork, A. R. Khosropour, *Polyhedron*, 49 (2013) 158.

[13] P. Yuan, D. Liu, M. Fan, D. Yang, R. Zhu, Fei Ge, J. Zhu, H. He, *J. Hazard. Mater*.,173 (2010) 614.

[14] V. Swarnalatha, R. A. Esther, R. Dhamodharan , *J. Mol. Catal. B: Enzym.*,96 (2013) 6.

[15] E. Ranjbakhsh , A. K. Bordbar, M. Abbasi, A. R. Khosropour, E. Shams, *J. Chem. Eng.* 179 (2012) 272.

[16] X. Jin, K. Zhang, J. Sun, J. Wang, Z. Dong , R. Li, *Catal. Commun*., 26 (2012) 199.

[17] M. Faraji, Y. Yamini, M. Rezaee, *J. Iran. Chem. Soc*., 7 (2010) 1.

[18] J. Cheon, J. H. Lee, *Acc. Chem. Res*., 41 (2008) 1630.

[19] M. Ahmed, M. Douek, *BioMed Res. Int*. 2013 (2013), 11 pages.

[20] C. Hopper, *Lancet Oncol*., 1 (2000) 212.

[21] A. Ito, M. Shinkai, H. Honda, T. Kobayashi, *J. Biosc. Bioeng.*, 100 (2005) 1.

[22] S. Mornet, S. Vasseur, F. Grasset, E. Duguet, *J. Mater. Chem*., 14 (2004) 2161.

[23] P. Reimer, C. Bremer, T. Allkemper, M. Engelhardt, M. Mahler, W. Ebert, B. Tombach, *Radiology*, 231 (2004) 474.
[24] A. B. Chin, I. I. Yaacob, *J. Mater. Process. Technol.*, 191 (2007) 14.

[25] C. Albornoz, S. E. Jacobo, *J. Magn. Magn. Mater.*, 305 (2006) 12.

[26] J. Wan, X. Chen, Z. Wang, X. Yang, Y. Qian, *J. Cryst. Growth*, 276 (2005) 571.

[27] G. S. Alvarez, M. Muhammed, A. A. Zagorodni, *Chem. Eng. Sci.*, 61 (2006) 4625.

[28] S. Basak, D. R. Chen, P. Biswas, *Chem. Eng. Sci.*, 62 (2007) 1263.

[29] S. A. Jadhav, R. Bongiovanni, *Adv. Mat. Lett.* 3 (5) (2012) 356

[30] A. K. Gupta, M. Gupta, *Biomaterials*, 26 (2005) 3995.

[31] J. C. Love, L. A. Estroff, J. K. Kriebel, R. G. Nuzzo, G. M. Whitesides, *Chem Rev*., 105 (2005) 1103.

[32] C. Nazli, T. I. Ergenc, Y. Yar, H. Y. Acar, S, Kizilel. *Int. J. Nanomedicine*,7 (2012) 1903.

[33] Y. Xu, S. Palchoudhury, Y. Bao, *Langmuir*, 27 (2011) 8990.

[34] A. M. Morawski, P. M. Winter, K. C. Crowder, S. D. Caruthers, R. W. Fuhrlop, M. J. Scott, J. D. Robertson, D. R. Abendschein, G. M. Lanza, S. A. Wickline, *Magn. Res. Med*., 51 (2004) 480.

[35] J. Sun, S. Zhou, P. Hou,Y. Yang, J. Weng, X. Li, M. Li, *J. Biomed. Mater. Res. A*, 80 (2007) 333.

[36] S. Calvin, E. E. Carpenter, V. G. Harris, *Phys. Rev. B: Condens. Matter Mater. Phys*., 68 (2003) 033411/1.

[37] Y. Zhua, F.Y. Jiang, K. Chena, F. Kanga, Z.K. Tang, *J. Alloys Compd*., 509 (2011) 8549.

[38] P. Granitzer, K. Rumpf, A.G. Roca, M. P.Morales, P. Poelt, M. Albu, *J. Magn. and Magn. Mater*.,322 (2010) 1343.

[39] J. B. Mamania, A. J. Costa-Filhob, D.R. Cornejoc, E.D. Vieirad, L.F. Gamarraa, *Materials characterization*, 81 (2013) 28.

[40] P. Gregory, *J. Porphyrins Phthalocyanines*, 3 (1999) 468.

[41] A. von Braun, J. Tscherniac, *Ber. Deut. Chem. Ges.*, 40 (1907) 2709.

[42] R. P. Linstead, *J. Chem. Soc.*, (1934) 1016.

[43] J. M. Robertson, *J. Chem. Soc*., (1935) 615.

[44] J. M. Robertson, *J. Chem. Soc*., (1936) 1195.

[45] M. G. Walter, A. B. Rudine , C. C. Wamser, *J. Porphyrins Phthalocyanines*, 14 (2010) 759.

[46] T. Reinot, W. H. Kim, J. M. Hayes, G. J. Small, *J. Opt. Soc. Am*., 602 (1997) B14.

[47] A. B. Djuri, C.Y. Kwong, T. W. Lau, W. L. Guo, E. H. Li, Z.T. Liu, H. S. Kwok, L. S. M. Lam, W. K. Chan, *Opt. Commun*., 205 (2002) 155

[48] F. Zhao, F. Harnisch, U. Schroder, F. Scholz, P. Bogdanoff, I. Herrmann, *Electrochem. Communi.*, 7 (2005) 1405.

[49] S. Vilakazi, T. Nyokong, *Polyhedron*, 19 (2000) 229.

[50] P. Kluson, M. Drobek, T. Strasak, J. Krysa, M. Karaskova, J. Rakusan, *J. Mol. Catal., A Chem.*, 272 (2007) 213.

[51] S. V. Rao, P. T. Anusha, T. S. Prashant, D. Swain, S. P. Tewari, *Mater. Sci. Appl.*, 2 (2011) 299.

[52] C. M. Allen, W. M. Sharman, J. E. Van Lier, *J. Porphyrins Phthalocyanines*, 5 (2001) 161

[53] J. Chen, Z. Chen, Y. Zheng, S. Zhou, J. Wang, N. Chen, J. Huang, F. Yan M. Huang, *J. Porphyrins Phthalocyanines*, 15 (2011) 293.

[54] X. Song, Y. She, H. Ji and Y. Zhang, *Org. Process. Res. Dev*., 9 (2005) 297.

[55] N. A. Wiederkehr, J. Braz., *Chem. Soc*., 7 (1996) 7.

[56] M. Keyanpour-Rad, *Iran. Polym. J*., 10 (2001) 224.

[57] M. A. A. El-Ghaffar, N. R. El-Halawany and H. A. Essawy, *J. Appl. Polym. Sci.,* 108 (2008) 3226.

[58] A. R. A Shoukat, J. Keshavayya, M. N. K. Harish, A. H. Shridhar, T. Rajesha and A. G. Prashantha, *Int.J. Chem. Tech. Res.,* 3 (2011) 1145.

[59] C. C. Leznoff, In Phthalocyanines: Properties and Applications, eds. C. C. Leznoff, A. B. P. Lever, VCH publishers, New York, Vol. 1 (1989)1, Chp. 1

[60] K. Sakamoto and E. Ohno, *Prog. Org. Coat.*,31 (1997) 139.

[61] T. Nyokong, Z. Gasyna, M.J. Stillman, *Inorg. Chem.,* 26 (1987) 548.

[62] F. R. Fan, L. R. Faulkner, *J. Am. Chem. Soc.* 101 (1979) 4779.

[63] J. Mack, M.J. Stillman, *J. Am. Chem. Soc*., 116 (1994) 1292.

[64] J. Mack, M. Stillman, *Coord. Chem. Rev*., 219 (2001) 993.

[65] M. Gouterman, in The Porphyrins, (Ed. D. Dolphin), *Part A. Physical Chemistry,* Academic Press, New York, (1978).

[66] A. J. McHugh, M. Gouterman, C. Weiss, *Theoret. Chim. Acta*, 24 (1987) 246.

[67] A. M. Schaffer, M. Gouterman, E. R. Davidson, *Theoret. Chim. Acta,* 30 (1973) 9.

[68] M. J. Stilman, T. Nyokong, In Phthalocyanines*: Properties and Applications,* Eds. C. C. Leznoff, A. B. P. Lever, VCH, New York, (1989).

[69] R. D. George, A.W. Snow, J. S. Shirk and W. R. Barger, *J. Porphyrin Phthalocyanines*, 2 (1998) 1.

[70] K. Kameyama, A. Satake and Y. Kobuke, *Tetrahedron Lett.,* 45 (2004) 7617.

[71] T. Nyokong, E. Antunes in The Handbook of Porphyrin Science. Eds. Kadish, K. M.; Smith, K. M.; Guilard, R., Academic Press: New York World Scientific, Singapore, Vol. 7, (2010).

[72] M. Kasha, *Radiat. Res.*, 20 (1960) 55.

[73] Z. Gasyna, N. Kobayashi, M.J. Stillman, *J. Chem. Soc., Dalton Trans.*, 12 (1989) 2397.

[74] A.W. Snow, in:, K.M. Kadish, K.M. Smith, R. Guilard (Eds.), The Porphyrin Handbook, Academic Press, 2003, pp. 129-176.

[75] J. R. Lakowicz, Principles of Fluorescence Spectroscopy, 3rd ed., Springer Science Business Media, LCC, New York, 2006.

[76] A. Gilbert, J.E. Baggott in: Essentials of Molecular Photochemistry, Blackwell Scientific, Oxford, 1991.

[77] D.F. Shriver, P.W. Atkins in: Inorganic Chemistry, 3rd ed., Oxford University Press, New York, 1999.

[78] J. G. Calvert, J. N. Pitts, *Photochem*., 285 (1967) 258.

[79] U. Resch-Genger, M. Grabolle, S. Cavaliere-Jaricot, R. Nitschke and T. Nann, *Nat. Methods*, 5 (2008) 763.

[80] S. Fery-Forgues, D. Lavabre, *J. Chem. Educ*., 76 (1999) 76.

[81] P. Kubat, J. Mosinger, *J. Photochem. Photobiol. A: Chem.*, 96 (1993) 93.

[82] J. Davila, A. Harriman, *Photochem. Photobiol*., 50 (1989) 29.

[83] J. D Spikes, J. E. van Lier, J. C. Bommer, *J. Photochem. Photobiol.* A: Biol., 91 (1995) 193.

[84] J. R. Darwent, P. Douglas, A. Harriman, G. Porter, M. C. Richoux, *Coord, Chem. Rev*., 44 (1982) 83.

[85] I. Seotsanyana-Mokhosi, T. Nyokong, *J. Porphyrins Phthalocyanines*, 8 (2004) 1214.

[86] A. O. Ogunsipe, T. Nyokong, *J. Porphrins Phthalocyanines*, 9 (2005) 121.

[87] M. Niedre, M. S. Patterson, B. C. Wilson, *Photochem. Photobiol*., 75 (2003) 382.

[88] M. S. Patterson, S. J. Madsen, R. Wilson, *J. Photochem. Photobiol. B*: 5 (1990) 69.

[89] C. S. Foote, In singlet oxygen (eds H. H. Wasserman and R. W. Murray) Academic Press, New York, San Francisco, London, 1979, 139.

[90] B. U. Jang, J. H. Choi, S. J. Lee , S. G. Lee, *J. Porphyrins Phthalocyanines*, 13 (2009) 779.

[91] Z. Guo , B. Chen, J. Mu , M. Zhang, P. Zhang, Z. Zhang, J. Wang , X. Zhang, Y. Sun, C. Shao, Y. Liu , *J. Hazard. Mater*, 219 (2012) 156.

[92] S. Rismayani, M. Fukushima, H. Ichikawa, K. Tatsumi, *J. Hazard. Mater*., B 114 (2004) 175.

[93] R. Zugle, T. Nyokong, *J. Mol. Catal. A: Chem. A: Chem.*, 366 (2013) 247.

[94] S. Tombe, E. Antunes, T. Nyokong, *J. Mol. Catal. A: Chem. A: Chem.*, 371 (2013) 125.

[95] D. M. Oliveira, P. P. Macaroff, K. F. Ribeiro, Z. G. M. Lacava, R. B. Azevedo, E. C. D. Limac, P. C. Morais, A. C. Tedesco, *J. Magn. Magn. Mater*. 289 (2005) 476.

[96] K. Ozawa, K. Ishii, *Phys. Chem. Chem. Phys*.,11 (2009) 1019.

[97] M. Idowu, T. Nyokong, *J. Photochem. Photobiol., A: Chem*. 188 (2007) 200.

[98] A. Rezaeifard, M. Jafarpour, A. Naeimi, R. Haddad , *Green Chem*., 14 (2012) 3386.

[99] F. Wang, X. Chen, Z. Zhao, S. Tang, X. Huang, C. Lin, C. Cai, N. Zheng, *J. Mater. Chem.*, 21 (2011) 11244.

[100] X. Chen, J. Zou , L. Liu, Y. Zhang, J. Huang, *Appl. Spectrosc.*, 64 (2010) 552.

[101] L. M. G. Jansen, I. P. Wilkes, F. Wilkinson, D. R. Worrall, *J. Photochem. Photobiol. A: Chem.*, 125 (1999) 99.

[102] K. T. Chung, S. E. Stevens, *Environ. Toxicol. Chem*. 12 (1993) 2121.

[103] X. C. Jin, G. Q. Liu. Z. H. Xu, W. Y. Tao, *Appl. Microbiol. Biotechnol.*,74 (2007) 239.

[104] J. T. Spadaro, M. H. Gold, V. Renganathan, *Appl. Environ. Microbiol.*, 58 (1992) 2397.

[105] S. Saranaik, P. Kanekar,. *J. Appl. Bacteriol.*79 (1995) 459.

[106] M. Pera-Titus, V. Garcia-Molina, M.A. Banos, *Appl. Catal. B: Environ.*, 47 (2004) 219.

[107] A. Özcan, M.A. Oturan, N. Oturan, Y. Sahin, *J. Hazard. Mater.*,163 (2009) 1213.

[108] H. T. Gomes, S. M. Miranda, M. J. Sampaio, A. M. T. Silva, J. L. Faria, *Catal. Today*, 15 (2010) 153.

[109] M. Koch, A. Yediler, D. Lienert, G. Insel, A. Kettrup, *Chemosphere,* 46 (2002) 109.

[110] N. Daneshvar, A. Oladegaragoze, N. Djafarzadeh, J. Hazard. *Mater.*, 129 (2006) 116.

[111] M. Mrowetz, C. Pirola, E. Selli, *Ultrason. Sonochem.*, 10 (2003) 247.

[112] S.J. Zhang, H.Q. Yu, Q.R. Li, *Chemosphere*, 61 (2005) 1003.

[113] N. Shimizu, C. Ogino, M.F. Dadjour, T. Murata, *Ultrason. Sonochem.*, 14 (2007) 184.

[114] J. Zeleny, *Physical reviews,* 3 (1914) 69.

[115] D. H. Reneker, I. Chun, *Nanotechnology,* 7 (1996) 216.

[116] P. Supaphol, C. Uppatham, M. Anakul, *J. Polym. Sci. B: Polym. Phys.,* 43 (2005) 3699.

[117] L.S. Carnell, E.J. Siochi, N.M. Holloway, R.M. Stephens, C. Rhim, L.E. Niklason and R.L. Clark, *Macromolecules,* 41 (2008) 5345.

[118] H. Wang, Q. Liu, Q. Yang, Y. Li, W. Wang, L. Sun, C. Zhang and X. Li, *J. Mater. Sci.*,45 (2010) 1032.

[119] S. De Vrieze, B. De Schoenmaker, O. Ceylan, J. Depuydt, L. Van Landuyt, H. Rahier, G. Van Assche, K. De Clerck, *J. Appl. Polym. Sci.,* 119 (2011) 2984.

[120] S. De Vrieze, P. Westbroek, T. Van Camp, K. De Clerck, *J. Appl. Polym. Sci.,* 115 (2010) 837.

[121] R. Nirmala, K. Nam, S. Park, Y. Shinc, R. Navamathavan, H. Kim, *Appl. Surf. Sci.,* 256 (2010) 6318.

[122] P. Heikkilä, A. Harlin. *Eur. Polym J.,* 44 (2008) 3067.

[123] R. Zugle, C. Litwisky, N. Torto, T. Nyokong. *New J. Chem.,* 35 (2011) 1588.

[124] B. De Schoenmaker, L. Van der Schueren, O. Ceylan, K. De Clerck, *J. Nanomat.,*1 (2012) 1.

[125] B. Carlberg, M. Z. Axell, U. Nannmark, J. Liu, H. G. Kuhn, *Biomed. Mater.,* 4 (2009) 045004.

[126] R. Zugle, E. Antunes, S. Khene, T. Nyokong, *Polyhedron,* 33 (2012) 74.

[127] R. Zugle, T Nyokong, *J. Mol. Cat. A: Cem.*, 358 (2012) 49.

[128] R. Zugle, T Nyokong, *J. Macromol. Sci., A: Pure Appl. Chem.,*49 (2012) 279.

[129] S. Tang, C. Shao, Y. Li, R. Mu, *J. Phys. Chem. Solids,* 68 (2007) 2337.

[130] J. Mosinger, K. Lang, P. Kubát, J. Sýkora, M. Hof, L. Píštil, B. Mosinger Jr., *J. Fluorec.,* 19 (2009) 709.

[131] S-L. Cheng, X-J. Huang, Z-K. Xu, *Cellulose*, 18 (2011) 1295.

[132] M. Karaskova, J. Rakusan, O. Jirsak, P. Jilek, NANCON, 2010, Olomouc, Czech Republic, EU.

[133] M. Ambroz, A. Beeby, A.J. McRobert, M.S.C. Simpson, R. K. Svensen, D. Phillips, *J. Photochem. Photobiol. B: Biol.,* 9 (1991) 87.

[134] K. Sakamoto, E. Ohno, *Prog. Org. Coat.,* 31 (1997) 139.

[135] A.R.A. Shoukat, J. Keshavayya, M.N.K. Harish, A.H. Shridhar, T. Rajesha, A.G. Prashantha, *Int. J. Chem. Tech. Res*., 3 (2011)1145.

[136] S. Beyaz, H. Kockar, T. Tanrisever, *J. Optoelectron. Adv. Mat.*,1 (2009) 447.

[137] J. Ho Chang, K. Ho Kang, J. Choi, Y. K. Jeong, *Superlattices Microstruct*., 44 (2008) 442.

[138] M. Idowu, T. Nyokong, *Int. J. Nanoscience*, 11 (2012) 1250018 (9 pages).

[139] A. Ogunsipe, J.Y. Chen, T. Nyokong, *New J. Chem.* 7 (2004) 822.

[140] A. Ogunsipe, T. Nyokong, *J. Photochem. Photobiol. A : Chem.* 173 (2005) 211.

[141] L. Jiang, A. Glidle, A. Griffith, C. J. McNeil and J. M. Cooper, *Bioelectrochem. Bioenerg*., 42 (1997) 15.

[142] J. Ho Chang, K. Ho Kang, J. Choi, Y. K. Jeong, *Superlattices Microstruct*., 44 (2008) 442.

[143] M. Idowu and T. Nyokong, *J. Photochem. Photobiol. A: Chem*., 200 (2008) 396.

[144] D.M. Oliveira, P.P. Macaroff, K.F. Ribeiro, R.B. Lacava, R.B. Azevedo, E.C.D. Lima, P.C. Morais and A.C.Tedesco, *J. Magn. Magn. Mater*., 289 (2005) 476.

[145] A. Pinchuk and G. Schatz, *Nanotechnology*, 16 (2005) 2209.

[146] S. Moeno, T. Nyokong, *Polyhedron*, 27 (2008) 1953.

[147] M.E. Park, J. Ho Chang, *Mater. Sci. Eng.* C., 27 (2007) 1232.

[148] B.N. Achar, K.S. Lokesh, *J. Organomet. Chem.*, 689 (2004) 2601.

[149] A. Kotiaho, R. Lahtinen, A. Efimov, H-K. Metsberg, E. Sariola, H. Lehtivuori, N.V. Tkachenko, H. Lemmetyinen, *J. Phys. Chem. C.*, 114 (2010) 162.

[150] J. A. Lacey, D. Philips, *Photochem. Photobiol. Sci.*, 1 (2002) 378.

[151] J. R. Darwent, P. Douglas, A. Harriman, G. Porter, M. C. Richoux, *Coord. Chem. Rev.*, 44 (1982) 83.

[152] M. Idowu, T. Nyokong, *J. Lumin.* 129 (2009) 356.

[153] S. D'Souza, E. Antunes, C. Litwinski, T. Nyokong, *J. Photochem. Photobiol. A: Chem*. 220 (2011) 11.

[154] J. C. Cha, D.I. Kim, H.Y. Lee, K.H. Jung, *J. appl. Polym. Sci.*, 96 (2005) 460.

[155] C. Mit-Uppatham, M. Nithitanakul, and P. Supaphol, *Macromol. Chem. Physic.*,205 (2004) 2327.

[156] B. De Schoenmaker, L. Van Der Schueren, S. De Vrieze, P. Westbroek, K. De Clerck, *J. Appl. Polym. Sci.*, 120 (2011) 305.

[157] Q. Pham, U. Sharma, A. Mikos. *Tissue engineering*, 12 (2006) 1197.

[158] C. Alkan, L. Aras, G. Gunduz, *J. Polym. Sci*. *A: Polym. Chem.*, 44 (2006) 5692.

[159] J. Sun, X. Wang, J. Sun, R. Sun, S. Sun, L. Qiao, *J. Mol. Catal. A: Chem*., 260 (2006) 241.